Institute of Protein Biochemistry

Head: Prof. Dr. Marcus Fändrich

Structural Analysis of Ex Vivo Amyloid Fibrils from AL Amyloidosis

Cumulative Dissertation

to obtain the degree Dr. rer. nat. of the

Faculty of Natural Sciences of Ulm University

submitted by

Lynn Radamaker, M.Sc.

Born in Haarlem, The Netherlands

Ulm, 2021

Current dean of the Faculty of Natural Sciences: Prof. Dr. Thorsten Bernhardt

First reviewer: Prof. Dr. Marcus Fändrich

Second reviewer: Prof. Dr. Johannes Buchner

Third reviewer: Prof. Dr. Luis del Pozo-Yauner

Day of doctorate awarded: 23rd June 2022

Table of Contents

1. Statutory declaration 4
2. List of Abbreviations 5
3. Summary 6
4. Introduction 8
    - 4.1 AL amyloidosis 8
    - 4.2 Amyloid fibrils 10
    - 4.3 Immunoglobulin light chains 14
    - 4.4 Structural analysis of AL amyloid fibrils 20
5. Aims 25
6. References to the Introduction 26
7. Publications 44
    - 7.1 List of Publications 44
    - 7.2 Publication I 45

      Cryo-EM structure of a light chain-derived amyloid fibril from a patient with systemic AL amyloidosis.
    - 7.3 Publication II 65

      Cryo-EM reveals structural breaks in a patient-derived amyloid fibril from systemic AL amyloidosis.
    - 7.4 Publication III 90

      Role of mutations and post-translational modifications in systemic AL amyloidosis studied by cryo-EM
8. Acknowledgements 146
9. Curriculum Vitae 148

1. Statutory Declaration

I hereby declare that I have done the work independently and have not used any other sources and resources than those indicated, have identified the passages taken over in words or content as references and have complied with the statutes of the University of Ulm for the Protection of Good Scientific Practice as currently published.

I agree that the dissertation may also be used for the purpose of verifying compliance with generally accepted scientific standards, in particular by using electronic data processing programs.

Ulm, 23rd June 2022

(Lynn Radamaker)

2. List of abbreviations

2D	Two-dimensional
3D	Three-dimensional
AL	Amyloid light chain
C	Constant gene segment
$C_{L/H}$	Constant light/heavy
CDR	Complementarity determining region
cryo-EM	Cryo-electron microscopy
EM	Electron microscope
GL	Germ line
HC	Heavy chain
J	Joining gene segment
LC	Light chain
PTM	Post-translational modification
ssNMR	Solid-state nuclear magnetic resonance
V	Variable gene segment
$V_{L/H}$	Variable light/heavy

3. Summary

The disease AL amyloidosis is caused by the misfolding of immunoglobulin light chains (LC). Due to an underlying plasma cell dyscrasia, amyloidogenic LCs are overproduced and their high serum concentrations lead to aggregation and amyloid fibril formation. The ensuing organ damage can be fatal, in particular in case of cardiac involvement. Current treatment options target the plasma cell clone, thereby reducing LC production and amyloid formation. However, no amyloid-targeting therapies are available and high-risk patients with advanced cardiac damage often die within months of diagnosis as the available treatments are unable to rapidly restore organ function. Being a patient-specific disease, the molecular mechanisms determining pathogenesis in AL amyloidosis are poorly understood. In particular, it is unclear how different factors influence amyloid fibril formation by the pathogenic LCs.

AL amyloidosis is a member of the group of clinical disorders termed the amyloidoses, which are based on the misfolding of different proteins into amyloid fibrils. Amyloid fibrils formed in vivo or in vitro from different proteins show similar characteristics: a long and straight appearance under an electron microscope, binding to amyloid-specific dyes, as well as a cross-β X-ray diffraction pattern. Although in vitro formed fibrils are generally easier to study than fibrils that are directly extracted from amyloidotic tissue, it remains to be established whether in vitro fibril structures are relevant to disease. Therefore, in order to shed light on disease processes, it is important to study ex vivo fibrils.

LCs are highly variable proteins due their natural function as antibody constituents. The LC sequence variability is a result of genetic recombination, junctional diversity and somatic hypermutation. These processes take place during the production and maturation of B cells. Previous studies have shown that AL fibril proteins contain several post-translational modifications (PTMs). AL fibril proteins have generally been proteolyzed and contain a disulfide bond. Also, AL

LCs are more often glycosylated than non-amyloidogenic LCs and sometimes pyroglutamylated. The contributions of sequence variability and PTMs to the structure and stability of AL amyloid fibrils are unclear. Structural information on AL amyloid fibrils is required to elucidate the influence of these factors. Previous studies have investigated the three-dimensional (3D) structure of AL amyloid fibrils using X-ray crystallography, solid-state nuclear magnetic resonance (ssNMR), negative-stain electron microscopy and cryo-electron microscopy (cryo-EM). However, these models were based on (short) fragments of LCs that were fibrillated in vitro and it is unclear whether they correspond to pathogenic, in vivo formed amyloid fibril structures.

In this thesis, 3D structures of pathogenic AL fibrils from three patient cases were obtained using cryo-EM. By imaging the AL fibrils directly in vitreous ice, their structures could be obtained by 3D reconstruction and molecular modeling. The models revealed that a rotational switch around the LC disulfide bond takes place during misfolding. Two similar amyloid folds, differing only in a short segment of the polypeptide chain, were found to occur within a single amyloid fibril, forming structural breaks at their interface. These structural breaks could play a role in, e.g., fibril fragmentation or interactions with other molecules. Furthermore, the structure of a glycosylated AL fibril showed that the glycosylation is present on the surface of the fibril where it protects the fibril from proteolytic degradation. By comparing the available ex vivo AL fibril structures, it was shown that mutations enable the LC fragments to adopt a proteolytically stable morphology that is able to withstand the degradation mechanisms in the body. The same LC fragments may adopt different amyloid folds in vitro, as demonstrated by an ssNMR study. In conclusion, this thesis has expanded the understanding of the molecular basis of AL amyloidosis by elucidating the influence of mutations and PTMs on the structure and stability of AL fibrils, as well as on the misfolding process. These insights could aid in the development of novel diagnostic tools and therapeutic approaches.

4. Introduction

4.1 AL Amyloidosis

AL amyloidosis is a devastating, rare disease with an estimated incidence of 4-15 per million inhabitants per year (Quock et al., 2018; Shimazaki, 2019; Wisniowski et al., 2019). An underlying plasma cell dyscrasia leads to the overproduction of monoclonal immunoglobulin light chains (LC), which are constituents of antibodies (Wolf et al., 1986; Gertz et al., 1991). The LCs misfold and aggregate, forming amyloid deposits in the body, which can cause tissue damage and organ dysfunction. Due to the systemic nature of the disease, the amyloid often deposits in multiple organs and tissues. The most frequently involved organs are the heart (~82 %), kidneys (~68 %), liver (~14 %), soft tissue (~17%), peripheral nervous system (~12%) and autonomic nervous system (~10%) (Merlini, 2017). The presence of amyloid can be detected by staining a biopsy sample with the amyloid-binding dye Congo red (Symmers, 1956; Westermark and Stenkvist, 1973; Schroeder et al., 1975; Arbustini et al., 1995). Typing of the protein that underlies the deposits is necessary to distinguish different forms of amyloidosis (Vrana et al., 2009; Schönland et al., 2012, Brambilla et al., 2012; Fernández de Larrea et al., 2015). Diagnosis and disease monitoring are supported by imaging techniques that can determine the extent of organ damage (Bhatti et al., 2016), as well as the measurement of biomarkers specific for AL amyloidosis. Patient survival mostly depends on the extent of cardiac damage, which can be measured by cardiac biomarkers (Dispenzieri et al., 2004; Lilleness et al., 2019). Furthermore, tumor burden is an important prognostic factor, which is measured by free LC concentration in serum (Kumar et al., 2012).

Current treatment schemes aim to suppress LC production by destroying the plasma cell clone. This is mainly achieved through chemotherapy, which can be combined with other therapies and/or medications (Kastritis et al., 2020; Cai et al., 2020). In case of extensive organ

damage, transplantation of the kidneys or heart can be performed in selected patients (Varr et al., 2012; Davis et al., 2015; Kristen et al., 2018; Angel-Korman et al., 2019). These treatment options have improved the survival of AL patients over the past decades (Staron et al., 2021), however high-risk patients with advanced cardiac damage still have a median survival of only ~6 months (Wechalekar et al., 2013; Manwani et al., 2018). One reason for these poor outcomes is delays in diagnosis, which means the disease has often progressed to the point of being fatal (McCausland et al., 2018). Another reason is that no amyloid-targeting therapies are available, so that the amyloid present in a patient can only be cleared by slow, body-own mechanisms (Fotiou et al., 2020). Therefore, patients with a high amyloid load often succumb to the organ damage before the body has time to clear the amyloid (Manwani et al., 2018). Thus, there is a need to develop therapies that enhance the clearance of amyloid deposits and aid in reversing organ damage (Fotiou et al., 2020). Insights into the molecular mechanisms of amyloid formation in AL amyloidosis can aid in the development of novel therapeutic approaches (Merlini, 2017).

One obstacle to obtaining insights into the molecular mechanisms underlying the pathogenesis in AL amyloidosis is the patient-specific nature of the disease. Due to their natural function as constituents of antibodies, LCs display a great variability in amino acid sequence, which means that each AL patient possesses a virtually unique LC underlying the amyloid deposits. This translates into heterogeneous clinical manifestations which complicate diagnosis and treatment (Bellotti et al., 2000; Merlini, 2017). Due to a lack of structural information, it is unclear how these different LCs misfold into amyloid fibrils. In order to identify common principles of misfolding in AL amyloidosis, this thesis presents the molecular structure of the amyloid fibrils from three different patient cases. These patients all had severe cardiac involvement requiring heart transplantation, which enabled the extraction of the fibrils directly from the explanted heart tissue. By comparing the different structures, common steps in the misfolding pathway and a fibril selection mechanism in vivo were identified.

4.2 Amyloid fibrils

Under normal, physiological conditions, most proteins fold into a specific three-dimensional (3D) structure termed the native conformation that is uniquely determined by the intramolecular interactions in the protein, and thus by its primary structure, i.e., the amino acid sequence (Anfinsen, 1973). As a properly folded structure is essential for protein function in most cases, cells have evolved mechanisms that ensure the correct folding of proteins and prevent misfolding. Nevertheless, sometimes proteins escape the quality control mechanisms and aggregate as amyloid fibrils inside the cell or in the extracellular space (Dobson, 2003). The amyloid fibril is a particularly stable misfolded state of protein (Knowles et al., 2014). Amyloid fibrils formed from different proteins naturally present in the human body are associated with a range of clinical disorders, generally termed the amyloidoses. 18 proteins that manifest as systemic amyloidoses and 22 that are associated with localized forms have been discovered (Benson et al., 2020). Examples are given in Table 1. In the neurodegenerative diseases, such as Alzheimer’s (Goedert and Spillantini, 2006) and Parkinson's disease (Braak and Braak, 2000), and the localized amyloidoses, such as lactoferrin amyloidosis (Ando et al., 2002), the amyloid deposits occur at the site of the protein precursor production. In systemic amyloidoses on the other hand, the proteins deposit far away from the site of production and typically affect multiple organs (Wechalekar et al., 2016). The nomenclature for systemic amyloidoses contains a letter “A” for amyloid, followed by an abbreviation of the precursor protein (Benson et al., 2020). The most common form of systemic amyloidosis in developed nations is AL amyloidosis. Other common forms are AA and ATTR amyloidosis, which are caused by the misfolding of the proteins serum amyloid A, and transthyretin, respectively (Wechalekar et al., 2016). It should be noted that AL amyloidosis can manifest both in systemic and localized forms. The systemic form can be lethal whereas the localized form is generally benign (Mahmood et al., 2015). In this thesis, systemic AL amyloidosis

Fibril protein	Precursor protein	Associated disorder	Affected organs	Systemic (S) and/or localized (L)
Aβ	Aβ precursor protein	Alzheimer's disease	Nervous system	L
ATau	Tau	Alzheimer's disease Pick's disease Chronic traumatic encephalopathy	Nervous system	L
AαSyn	α-synuclein	Parkinson's disease	Nervous system	L
ALact	Lactoferrin	Lactoferrin Amyloidosis	Cornea	L
AL	Immunoglobulin light chain	AL amyloidosis	All organs usually except CNS	S, L
AH	Immunoglobulin heavy chain(Apo) serum amyloid A	AH amyloidosis	All organs except CNS	S, L
AA	(Apo) serum amyloid A	AA amyloidosis	All organs except CNS	S
ATTR	Transthyretin	ATTR amyloidosis	Heart mainly in males, lung, ligaments, tenosynovium	S
Aβ2M	β2-microglobulin	Dialysis-related amyloidosis	Musculoskeletal system	S

Table 1. Prominent examples of diseases associated with amyloid deposits (Benson et al., 2020).

was investigated.

Although the proteins underlying the amyloidoses are diverse in their biological functions, amino acid sequences and native structures, the amyloid fibrils formed from these proteins display common characteristics (Sunde et al., 1997). These characteristics include the binding to specific dyes, in particular to Congo red, which is used for demonstrating the presence of amyloid in a sample (Bennhold, 1922). When Congo red binds to amyloid, it produces a birefringence when viewed under a polarization light microscope, which testifies to the regular,

ordered structure of amyloid fibrils (Romhányi, 1971). Under an electron microscope (EM), the amyloid fibrils appear as long, straight and unbranched structures with a typical width of 5-14 nm and a varying length of up to several micrometers (Cohen and Calkins, 1959). They consist of one or several protofilaments, the fibril subunits (Serpell et al., 2000). They often display a helical symmetry, which can be seen in the EM images as periodic constrictions (termed crossovers) of the fibril width (Fändrich, 2007). The helical twist stems from the chirality of amino acids and can be left- or right-handed depending on sequence and environmental conditions (Kurouski, 2016). A remarkable feature which contrasts starkly to the unique 3D structure of the native state of proteins is that amyloid fibrils display structural polymorphism. Multiple fibril morphologies can be assumed by a single protein, even within one sample. Different fibril morphologies can often be visually distinguished in EM images, typically by their width and degree of twist (Fändrich et al., 2018). Further common characteristics of the amyloid fibril structure are revealed by X-ray diffraction studies. The X-ray diffraction patterns of amyloid fibrils show that the fibril proteins form pleated β-sheets parallel to the fibril axis, with a spacing of 4.7 – 4.8 Å between the individual β-strands and a spacing of 8 -12 Å between β-sheets (Eanes and Glenner, 1968; Sunde et al., 1997). This structure is called the cross-β conformation and is considered to be the biophysical hallmark of amyloid fibrils (Benson et al., 2020).

Amyloid fibrils produced in vitro were initially referred to as “amyloid-like” in order to distinguish them from amyloid fibrils associated with diseased tissue (Glenner et al., 1971). Recently however, the definition of amyloid fibrils has come to include all fibrils with a cross-β diffraction pattern, according to the recommendations of the International Society of Amyloidosis nomenclature committee (Benson et al., 2020). Although it is possible to isolate or recombinantly produce proteins with the same sequence as found in a patient and to form amyloid fibrils from these proteins in vitro, the structures of these in vitro fibrils may not correspond to the in vivo structures (Annamalai et al., 2017). It remains an open question whether in vitro fibril structures are

relevant to disease. Many factors have been suggested to influence the fibril structures in vivo, such as components of the extracellular matrix, enzymes, proteases and chaperones (Zhang et al., 2017), which are lacking in vitro. Therefore, it is important to study amyloid fibrils directly extracted from diseased tissue. In this thesis, AL amyloid fibrils were extracted directly from patient heart tissue.

4.3 Immunoglobulin Light Chains

Natural function and sequence variability of immunoglobulin light chains

In a normal biological context, LCs are constituents of antibodies, which are a central part of the adaptive immune system. Antibodies consist of two identical LCs combined with two identical heavy chains (HC) roughly arranged in a y-shape (Cohen and Porter, 1964; Valentine and Green, 1967) (Fig. 1a,b). The LCs have a mass of ~25 kDA and consist of one variable light (V_L) and one constant light (C_L) domain whereas the HCs have a molecular mass of around ~50 kDa and consist of one variable heavy (V_H) and three constant heavy (C_H) domains (Edelman and Benacerraf, 1962; Fleischman et al., 1963; Hilschmann and Craig, 1965). The LC is connected to its partnering HC through a disulfide bond (Fleischman et al., 1963). An immunoglobulin domain consists of ~110 amino acids and is folded in the shape of a β-barrel in which two β-sheets consisting of 3 and 4 (C domains) or 4 and 5 (V domains) β-strands face each other and are connected by a conserved disulfide bond (Edmundson et al., 1975) (Fig. 1c). The V_L and V_H have a high sequence variability that results in a great number of different antibodies that can bind a vast array of different molecular structures on pathogens: typically proteins and polysaccharides (Porter, 1967). Three loops in the V_L and V_H each, termed the complementarity determining regions (CDR), combine to form an antigen-binding site on each arm of the antibody (Fig. 1a,b). The CDRs display the highest sequence variability in the V_L and V_H, which enables specific and sensitive antigen binding (Wu and Kabat, 1970).

The sequence variability of the LCs mainly results from three different processes taking place during the maturation of B cells and their differentiation into plasma cells: genetic recombination, junctional diversity and somatic hypermutation (Tonegawa, 1983). Genetic recombination involves the irreversible rearrangement of DNA in the B cell (Dreyer and Bennett,

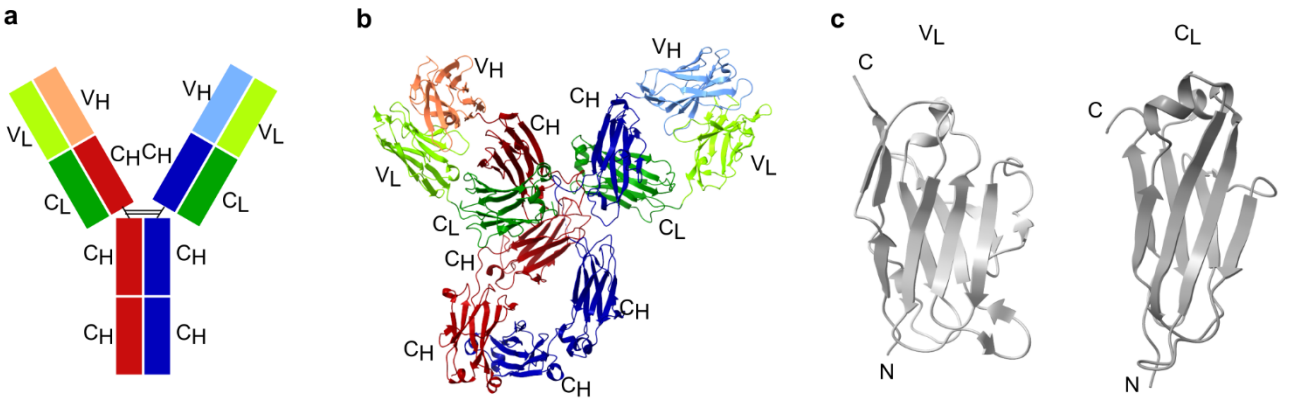

Figure 1: Antibody and immunoglobulin domain structure. (a) Schematic structure of an antibody composed of two heavy chains (red and blue) and two light chains (green). Dark shades represent the constant regions whereas light shades represent the variable regions. (b) Structure of an antibody (PDB: 5DK3). Coloring as in (a). (c) Structure of the immunoglobulin V_L and C_L domains (PDB: 5DK3). N- and C-termini are marked.

1965). The LC is encoded by three different germ line (GL) gene segments: a variable (*V*), joining (*J*) and constant (*C*) segment, where the *V* and *J* segments together encode the V_L. Two types of LCs exist: κ and λ type. There are 34-38 *Vκ*, 5 *Jκ* and 1 *Cκ* functional genes, whereas there are 29-33 *Vλ*, 4-5 *Jλ* and 4-5 *Cλ* functional genes (Lefranc, 2001). The genes encoding the *V* segments are located far away from the *J* segments on the chromosome (Hozumi and Tonegawa, 1976). The *J* genes are separated from the *C* genes only by an intron (Brack et al., 1978). During the maturation of the B cell, a *V* gene segment is ligated to a *J* gene segment by the removal of intervening DNA. The *C* segment is joined to the *VJ* segment after transcription by RNA splicing (Brack et al., 1978). Due to the random selection of the *V* and *J* gene segments, the genetically encoded variety in immunoglobulin sequences is combinatorially enhanced. Nucleotides can be randomly inserted or deleted between the *V* and *J* segment, leading to further variability in the translated LC sequence,

which is termed junctional diversity (Sakano et al., 1980; Tonegawa, 1983). The B cells initially circulate in an inactive form. When their B cell receptors (membrane-bound antibodies) are stimulated by antigen, the cells begin to proliferate and differentiate into plasma cells (Murphy and Weaver, 2016). During proliferation, point mutations are inserted into the *V, J* and *C* gene segments. This process is referred to as somatic hypermutation (Tonegawa, 1983). Plasma cells producing antibodies with mutations that increase the binding affinity to the antigen, mostly in the CDRs of the V_L, are stimulated to proliferate, while the other clones are removed by apoptosis. After several cycles of proliferation, the antigen-driven selection leads to a clonal population of plasma cells producing antibodies with high sensitivity and selectivity for the antigen (Murphy and Weaver, 2016).

Misfolding and aggregation of immunoglobulin light chains

In AL amyloidosis, plasma cells producing monoclonal immunoglobulin LCs are proliferating uncontrollably due to chromosomal aberrations and abnormal gene expression (Deshmukh et al., 2009; Granzow et al., 2017). This leads to an overproduction of monoclonal LCs, which are no longer paired to HCs in intact antibodies. The high serum concentration of unpaired LCs favors protein aggregation; however, this is not sufficient to explain the formation of amyloid deposits. Similar high serum concentrations of free LCs are seen in other plasma cell dyscrasias, such as in multiple myeloma or LC deposition disease, but without concurrent amyloid fibril formation (Sikkink and Ramirez-Alvarado, 2008). Although the factors contributing to LC amyloidogenicity are not fully understood, it is clear that the LC sequence plays an important role (Blancas-Mejia et al., 2018). Due to the natural variability in the LC sequence, each AL patient possesses a virtually unique LC. In AL patients, λ LCs are found in ~75 % of cases and κ in the remaining cases (Merlini, 2017). Furthermore, patient serum displays abnormal κ/λ ratios (Perfetti et al., 1995; Katzmann et al., 2002). This indicates that λ LCs are more likely to become amyloidogenic (Alim et

al., 1999). In particular, the GL segments *IGLV6-57; IGLV3-01; IGLV2-14* and *IGKV1-33* are found more frequently in AL amyloidosis than in the normal B cell repertoire and constitute around half of the cases in systemic AL amyloidosis (Perfetti et al., 2012; Kourelis et al., 2017). The GL segments are also associated with organ involvement: *IGLV1-44; IGLV2-14* and *IGLV3-1* are associated with cardiac, while *IGLV6-57* is associated with renal and *IGK1-33* with hepatic involvement (Perfetti et al., 2012; Kourelis et al., 2017). These observations indicate that the GL segment influences the amyloid formation propensity of the LC. However, none of the GL segments encode inherently amyloidogenic LCs. Instead, the LCs are rendered amyloidogenic by the insertion of point mutations (Hurle et al., 1994). Due to the variability in the LC sequence, it has not been possible to pinpoint specific mutations that universally cause AL amyloidosis, because the effect of the mutations seems to depend on the sequence context (Blancas-Mejia et al., 2018). However, sequence alignment has shown that certain positions in the LC sequence are more frequently mutated in AL amyloidosis than in patients with other disorders or in healthy individuals (Poshusta et al., 2009). These mutational hot spots map to specific β-sheets in the native structure and are associated with the serum free LC levels in the patient, indicating that the position rather than the number of mutations plays a role in LC amyloidogenesis. Furthermore, the effect of mutations on the amyloid formation rate of different LCs has been investigated by recombinant production of LC (fragment) proteins and in vitro fibril formation (Hurle et al., 1994; Baden et al., 2008b; Marin-Argany et al., 2015; Nokwe et al., 2016; Blancas-Mejia et al., 2014; Kazman et al., 2020; Rottenaicher et al., 2021). These studies have shown that the introduction of a single or small number of patient-associated mutations suffices to cause the V_L domain to spontaneously form fibrils under near-physiological conditions. These mutations affect side chain interactions or cause unfavorable backbone conformations leading to conformational stress. These changes decrease the thermodynamic stability and/or increase conformational dynamics of the V_L domain (Oberti et al., 2017), resulting in a larger population of unfolded or partially folded states. In these misfolding

intermediates, hydrophobic regions that are normally buried in the native state are exposed on the surface of the protein, thereby favoring protein-protein interactions and aggregation, which leads to a higher amyloid-forming propensity (Ferreira et al., 2006). Sometimes the mutations affect the V_L dimer interface, decreasing the dimerization rate (Baden et al., 2008a; Morgan et al., 2019). The V_L dimer mimics the interactions in a full antibody and therefore it is thought that the dimer state is protective against amyloid formation because it stabilizes the V_L domain. Although numerous studies have investigated the influence of the sequence on the native state of the LC, it has so far not been possible to assess the role of the sequence in stabilizing and shaping the amyloid state due to a lack of structural information. In this thesis, the role of the GL segment and the positions of the mutations are analyzed in ex vivo AL fibril structures.

Post-translational modifications in AL amyloidosis

Apart from the LC sequence, it is thought that certain post-translational modifications (PTM) can influence the fibril formation process and fibril structure. One important PTM in AL amyloidosis is proteolysis. In AL patients with λ LCs, the amyloid deposits mainly consist of N-terminal fragments encompassing the V_L domain, indicating that the majority of the C_L domain was proteolytically cleaved off (Glenner et al., 1970; Buxbaum, 1986; Enqvist et al., 2009). Isolated patient-derived λ V_L domains readily form fibrils in vitro whereas their full-length counterparts mostly do not, suggesting that the removal of the C_L domain is necessary for activating the amyloidogenic properties of the V_L domain (Morgan and Kelly, 2016; Kazman et al., 2020; Rottenaicher et al., 2021). On the other hand, it was suggested that full-length LCs initiate aggregation, forming a template for fibril formation by the V_L domain (Klimtchuk et al., 2010). It is so far not clear whether proteolysis takes place before or after fibril formation in vivo (Enqvist et al., 2009; Lavatelli et al., 2020). Another PTM which is present in AL fibril proteins is the disulfide bond, which corresponds to the canonical disulfide bond of the native structure. The retention of the

disulfide bond in the fibril structure indicates that misfolding occurred in an oxidative environment (Lim et al., 2001; Annamalai et al., 2017). Glycosylation is a PTM which is found more frequently in the LCs from AL patients than in other LCs, indicating that it enhances amyloid fibril formation (Kumar et al., 2019; Dispenzieri et al., 2020; Mellors et al., 2021). It has been suggested that glycosylated fibrils are protected from degradation (Bellotti et al., 2000). This mechanism is similar to the protection provided to amyloid deposits by glycosylated serum amyloid P component (Pepys et al., 1994). Other PTMs such as pyroglutamylation have been identified in some AL LCs, but it is unclear at present whether these contribute to amyloid formation (Klafki et al., 1992; Omtvedt et al., 1997; Yazaki et al., 2004; Lu et al., 2017). The influence of these different PTMs on the AL fibril structure is so far unknown. This thesis provides insight into the role of PTMs in AL fibril formation by elucidating the structure of several AL amyloid fibrils that have been proteolytically cleaved and contain a disulfide bond. Furthermore, one fibril structure additionally contains a glycosylation and a pyroglutamylation, revealing the contribution of these PTMs to the fibril structure.

4.4 Structural analysis of AL amyloid fibrils

Previous models of AL amyloid fibrils

X-ray diffraction studies have shown that AL amyloid fibrils, similarly to other amyloid fibrils, have an all β-sheet secondary structure and that the hydrogen-bonded β-strands are arranged perpendicular to the fibril axis with a helical twist (Eanes and Glenner, 1968; Sunde et al., 1997). In order to gain insight into the tertiary structure of AL amyloid fibrils, short amyloidogenic peptides were identified in patient LC sequences. In isolation from the rest of the sequence, these peptides form amyloid-like microcrystals, which were characterized by X-ray crystallography (Brumshtein et al, 2018). In X-ray crystallography, crystals are exposed to X-rays yielding a diffraction pattern. From the angles and intensities in the diffraction pattern, the positions of the atoms in the sample can be calculated (Woolfson and Woolfson, 1997). The crystal structures showed that the LC-derived peptides assemble into paired flat parallel or anti-parallel β-sheets with interdigitating side-chains. This structural motif is termed the steric zipper (Nelson et al., 2005; Sawaya et al., 2007) and it is stabilized by backbone hydrogen-bonds between the β-strands along the fibril axis, hydrophobic interfaces and van der Waals forces between the side chains (Eisenberg and Sawaya 2017). Short fragments of AL LCs not only form steric zippers in amyloid-like crystals, but also in amyloid fibrils as demonstrated by cryo-electron microscopy (cryo-EM) (Schmidt et al., 2016). The geometry of these steric zipper pairs, which form the protofilaments that construct the fibrils, was sufficient to explain the formation of different polymorphs in the in vitro sample through energy minimization (Close et al., 2018). However, it was unclear whether steric zippers play a role in the amyloid fibril structures formed by longer LC fragments. Based on the observation that a wide range of amyloidogenic peptides form steric zippers, it was suggested that steric zippers form the spines of amyloid fibrils from full-length proteins (Sawaya et al., 2007). Using the crystal structures of the LC fragments, speculative models were constructed that encompassed full-length V_L domains

arranged around the steric zipper spine (Brumshtein et al., 2018). It was shown that the V_L domains could be accommodated in the structure in a near-native conformation. Therefore, it was suggested that LC aggregation requires only minimal unfolding and that the formation of steric zippers might trigger additional unfolding in the V_L domains leading to further structural rearrangements (Brumshtein et al., 2018).

The structures of amyloid fibrils formed from patient-derived LC fragments have been studied using solid-state nuclear magnetic resonance (ssNMR) (Piehl et al., 2017a; Piehl et al., 2017b; Lecoq et al., 2019; Pradhan et al., 2020; Pradhan et al., 2021). SsNMR requires an isotopically labelled sample and therefore the amyloid fibrils are produced in vitro from recombinantly produced, labelled LC fragments. In an ssNMR experiment, the resonance signals of the isotopes in an oscillating magnetic field are measured. These resonances provide information on the relative positions and interactions between atoms in the sample (Hoult and Bhakar, 1997). The ssNMR studies of in vitro formed AL fibrils revealed that the secondary structural elements and intermolecular contacts are different from those of the native state (Piehl et al., 2017a; Piehl et al., 2017b; Lecoq et al., 2019; Pradhan et al., 2020; Pradhan et al., 2021). Contrary to the steric zipper spine models (Brumshtein et al., 2018), this observation implies that the proteins must undergo a profound structural rearrangement in order to form amyloid fibrils. One limitation of the ssNMR studies is that no 3D structure could be obtained. This requires a homogeneous sample which is difficult to achieve with AL amyloid fibrils. Further, ssNMR is limited to studying in vitro formed fibrils, whose structures may not faithfully reproduce the fibril structures present in vivo (Annamalai et al., 2017). Therefore, it is important to study the structure of ex vivo amyloid fibrils in order to obtain insights into the molecular mechanisms of disease.

To extract AL amyloid fibrils from patient tissue, protocols based on the water extraction method have been employed (Pras et al., 1968; Annamalai et al., 2016). As this extraction procedure does not involve harsh chemical conditions that could significantly alter the fibril

structure, it is generally assumed that the structure of ex vivo fibrils is highly similar, if not identical, to the fibril structures present in vivo (Pras et al., 1968). Negative-stain EM images of the ex vivo AL fibrils showed that they are polymorphic in vivo (Annamalai et al., 2016) and that the same morphologies are found in different tissues of the same patient (Annamalai et al., 2017). This fact suggests a systemic mechanism of misfolding, as opposed to an organ- or tissue-specific mechanism. Furthermore, the set of polymorphs in the ex vivo sample was compared to that of fibrils formed in vitro from the extracted, denatured and refolded fibril proteins from the same patient (Annamalai et al., 2017). It was shown that both the degree of polymorphism and the visual features of the individual polymorphs (width at and between crossovers, degree of twist) differed between the ex vivo and in vitro samples. This result indicates that the ex vivo fibril structures were not reproduced in vitro, highlighting the importance of studying ex vivo fibrils. The main morphologies present in two patient cases were reconstructed from negative-stain EM images (Annamalai et al., 2017). The reconstructed maps had a resolution of ~30 Å and they revealed the rough shape of the fibril cross-section. However, the precise fold of the polypeptide chain remained obscure. High resolution reconstructions revealing the molecular structure of proteins in amyloid fibrils can be obtained using cryo-EM. As cryo-EM is the main technique used in this thesis, a detailed description of this method is given in the next section.

Cryo-electron microscopy of amyloid fibrils

In cryo-EM, a small amount of sample is applied to a (carbon-coated) metal grid that is plunged into a cryogen, usually liquid ethane or propane, which is kept at liquid nitrogen temperature (Dubochet and McDowall, 1981; McDowall et al., 1983). The rapid freezing that occurs by this plunging process avoids the formation of crystalline ice. The resulting thin layer of vitreous ice hardly interacts with the electron beam and therefore provides a transparent support while also providing some protection from beam damage (McDowall et al., 1983). The native aqueous environment is

preserved, thereby avoiding structure distortion and the introduction of artifacts (McDowall et al., 1983). Images of small sections of these frozen grids are recorded with an EM. In principle, high resolutions can be achieved with an EM due to the short wavelength of electrons (~0.02 Å at 300 kV) (Egerton, 2005). However, as organic molecules interact weakly with the electron beam, the images have low contrast as well as a low signal to noise ratio (McDowall et al., 1983). Therefore, in order to extract high resolution information from cryo-EM images, a large number, typically several thousands, of images needs to be recorded. These images are then computationally processed with dedicated software tools in order to obtain a 3D reconstruction (Crowther and Wischik, 1985; Cheng et al., 2015).

By recording two-dimensional (2D) images from different angles, the 3D structure of an imaged complex can be reconstructed (De Rosier and Klug, 1968; Scheres, 2012). In the case of amyloid fibrils, their helical symmetry is an advantage, as it provides rotational views of the structure along the fibril axis (He and Scheres, 2017). In helical reconstruction of amyloid fibrils, fibril segment images are aligned and averaged in 3D space to produce a 3D map of the fibril. Through a process termed back-projection, 2D projections of this map are computationally compared to the raw data fibril segment images and the positions and angles of the image segments in the map are adjusted to yield an improved 3D map (De Rosier and Klug, 1968; Scheres, 2012). This process is repeated iteratively, which continually improves the match between the reconstructed 3D map and the raw data. Refinement and post-processing steps can further improve the map (Scheres, 2012). In order to interpret the reconstructed 3D map, a model of the polypeptide chain is fitted to the density using molecular modeling software (Jones, 1985; Brown et al., 2015).

During the course of the research project that is presented in this thesis, cryo-EM was employed by other researchers to solve the molecular structures of several pathogenic ex vivo amyloid fibrils to resolutions of 3 – 5 Å (Fitzpatrick et al., 2017; Falcon et al., 2018; Falcon et al., 2019; Kollmer et al., 2019; Liberta et al., 2019; Schmidt et al., 2019; Arakhamia et al., 2020;

Schweighauser et al., 2020). All of these ex vivo fibril structures differed from the structures of in vitro formed fibrils from the same protein (Li et al., 2018; Guerrero-Ferreira et al., 2018; Guerrero-Ferreira et al., 2019; Kollmer et al., 2019; Schmidt et al., 2019; Zhang et al., 2019; Bansal et al., 2021). The positions of the mutations could be analyzed in the fibril structures. In one case, the inhibitory effect of an amino acid substitution on fibril formation could be rationalized with the help of the ex vivo fibril structure (Liberta et al., 2019). In addition, the influence of PTMs such as proteolysis, phosphorylation and ubiquitination on the fibril structure could be clarified (Liberta et al., 2019; Scheres et al., 2020; Arakhamia et al., 2020). In this thesis, the structures of ex vivo AL amyloid fibrils have been solved using cryo-EM. The reconstructed density maps have near-atomic resolution and could be fitted with molecular models that show the general fold of the polypeptide backbone as well as the positions of a number of side chains. Based on the positions of mutations and the presence of PTMs in these structures, common steps in the misfolding pathway of LCs and a selection mechanism of fibril morphologies in vivo could be identified. In parallel to this research project, a cryo-EM structure of an ex vivo AL fibril was solved by another research group (Swuec et al., 2019). Comparisons between this structure and the three structures from this thesis are discussed in research paper #3.

5. Aims

Amyloid deposition of immunoglobulin LCs characterizes the disease AL amyloidosis. The molecular mechanisms behind the misfolding and amyloid formation of LCs are poorly understood due to the patient-specific nature of the disease and a lack of structural information. The structures and properties of in vitro formed AL fibrils have been studied by different methods, however it remains unclear whether they correspond to those of ex vivo AL amyloid fibrils. Therefore, it is important to study the structure of ex vivo fibrils directly. Cryo-EM has recently emerged as an invaluable tool for revealing the molecular structure of ex vivo amyloid fibrils.

In this thesis, I analyzed ex vivo amyloid fibrils extracted from the hearts of three different patients suffering from AL amyloidosis. My aims were to:

1. Elucidate the molecular structure of ex vivo AL fibrils from three patient cases
2. Identify common principles of misfolding in AL amyloidosis based on the structures of different ex vivo AL fibrils
3. Analyze the influence of mutations and post-translational modifications on the fibril structure

The molecular structures of ex vivo fibrils from three patient cases were solved down to near-atomic resolution using cryo-EM, helical reconstruction and molecular modeling. By comparing different AL fibril structures, common steps in the misfolding process of amyloidogenic LCs were revealed. A rotational switch around the disulfide bond is a common step in LC misfolding. Mutations and PTMs present in amyloidogenic LCs contribute to the formation of a specific, proteolytically stable morphology. Interfering with specific steps in the misfolding cascade and inhibiting the adoption of proteolytically stable morphologies could be the basis for novel therapies.

6. References to the Introduction

Alim, M.A., Yamaki, S., Hossain, M.S., Takeda, K., Yamagata, F., Takashi, I. and Shinoda, T., 1999. Structural relationship of λ-type LCs with AL amyloidosis. *Clinical immunology*, *90*(3), pp.399-403

Ando, Y., Nakamura, M., Kai, H., Katsuragi, S., Terazaki, H., Nozawa, T., Okuda, T., Misumi, S., Matsunaga, N., Hata, K. and Tajiri, T., 2002. A novel localized amyloidosis associated with lactoferrin in the cornea. *Laboratory investigation*, *82*(6), pp.757-766

Anfinsen, C.B., 1973. Principles that govern the folding of protein chains. *Science*, *181*(4096), pp.223-230

Angel-Korman, A., Stern, L., Sarosiek, S., Sloan, J.M., Doros, G., Sanchorawala, V. and Havasi, A., 2019. Long-term outcome of kidney transplantation in AL amyloidosis. *Kidney international*, *95*(2), pp.405-411

Annamalai, K., Gührs, K.H., Koehler, R., Schmidt, M., Michel, H., Loos, C., Gaffney, P.M., Sigurdson, C.J., Hegenbart, U., Schönland, S. and Fändrich, M., 2016. Polymorphism of amyloid fibrils in vivo. *Angewandte Chemie International Edition*, *55*(15), pp.4822-4825

Annamalai, K., Liberta, F., Vielberg, M.T., Close, W., Lilie, H., Gührs, K.H., Schierhorn, A., Koehler, R., Schmidt, A., Haupt, C. and Hegenbart, U., 2017. Common fibril structures imply systemically conserved protein misfolding pathways in vivo. *Angewandte Chemie*, *129*(26), pp.7618-7622

Arakhamia, T., Lee, C.E., Carlomagno, Y., Duong, D.M., Kundinger, S.R., Wang, K., Williams, D., DeTure, M., Dickson, D.W., Cook, C.N. and Seyfried, N.T., 2020. Posttranslational modifications mediate the structural diversity of tauopathy strains. *Cell*, *180*(4), pp.633-644

Arbustini, E., Merlini, G., Gavazzi, A., Grasso, M., Diegoli, M., Fasani, R., Bellotti, V., Marinone, G., Morbini, P., Dal Bello, B. and Campana, C., 1995. Cardiac immunocyte-derived (AL) amyloidosis: an endomyocardial biopsy study in 11 patients. *American heart journal*, *130*(3), pp.528-536

Baden, E.M., Owen, B.A., Peterson, F.C., Volkman, B.F., Ramirez-Alvarado, M. and Thompson, J.R., 2008a. Altered dimer interface decreases stability in an amyloidogenic protein. *Journal of Biological Chemistry*, *283*(23), pp.15853-15860.

Baden, E.M., Randles, E.G., Aboagye, A.K., Thompson, J.R. and Ramirez-Alvarado, M., 2008b. Structural insights into the role of mutations in amyloidogenesis. *Journal of Biological Chemistry*, *283*(45), pp.30950-30956

Bansal, A., Schmidt, M., Rennegarbe, M., Haupt, C., Liberta, F., Stecher, S., Puscalau-Girtu, I., Biedermann, A. and Fändrich, M., 2021. AA amyloid fibrils from diseased tissue are structurally different from in vitro formed SAA fibrils. *Nature communications*, *12*(1), pp.1-9

Bellotti, V., Mangione, P. and Merlini, G., 2000. Immunoglobulin LC amyloidosis—the archetype of structural and pathogenic variability. *Journal of structural biology*, *130*(2-3), pp.280-289

Bennhold, H., 1922. Eine spezifische Amyloidfärbung mit Kongorot. *Meunch. Med. Wocheschr.*, *69*, pp.1537-1538

Benson, M.D., Buxbaum, J.N., Eisenberg, D.S., Merlini, G., Saraiva, M.J., Sekijima, Y., Sipe, J.D. and Westermark, P., 2020. Amyloid nomenclature 2020: update and recommendations by the International Society of Amyloidosis (ISA) nomenclature committee. *Amyloid*, *27*(4), pp.217-222

Bhatti, S., Watts, E., Syed, F., Vallurupalli, S., Pandey, T., Jambekar, K., Mazur, W. and Hakeem, A., 2016. Clinical and prognostic utility of cardiovascular magnetic resonance

imaging in myeloma patients with suspected cardiac amyloidosis. *European Heart Journal-Cardiovascular Imaging*, *17*(9), pp.970-977

Blancas-Mejia, L.M., Misra, P., Dick, C.J., Cooper, S.A., Redhage, K.R., Bergman, M.R., Jordan, T.L., Maar, K. and Ramirez-Alvarado, M., 2018. Immunoglobulin LC amyloid aggregation. *Chemical communications*, *54*(76), pp.10664-10674

Blancas-Mejía, L.M., Tischer, A., Thompson, J.R., Tai, J., Wang, L., Auton, M. and Ramirez-Alvarado, M., 2014. Kinetic control in protein folding for LC amyloidosis and the differential effects of somatic mutations. *Journal of molecular biology*, *426*(2), pp.347-361

Braak, H. and Braak, E., 2000. Pathoanatomy of Parkinson's disease. *Journal of neurology*, *247*(2), pp.II3-II10

Brack, C., Hirama, M., Lenhard-Schuller, R. and Tonegawa, S., 1978. A complete immunoglobulin gene is created by somatic recombination. *Cell*, *15*(1), pp.1-14

Brambilla, F., Lavatelli, F., Di Silvestre, D., Valentini, V., Rossi, R., Palladini, G., Obici, L., Verga, L., Mauri, P. and Merlini, G., 2012. Reliable typing of systemic amyloidoses through proteomic analysis of subcutaneous adipose tissue. *Blood 119*(8), pp.1844-1847

Brown, A., Long, F., Nicholls, R.A., Toots, J., Emsley, P. and Murshudov, G., 2015. Tools for macromolecular model building and refinement into electron cryo-microscopy reconstructions. *Acta Crystallographica Section D: Biological Crystallography*, *71*(1), pp.136-153

Brumshtein, B., Esswein, S.R., Sawaya, M.R., Rosenberg, G., Ly, A.T., Landau, M. and Eisenberg, D.S., 2018. Identification of two principal amyloid-driving segments in variable domains of Ig LCs in systemic light-chain amyloidosis. *Journal of Biological Chemistry*, *293*(51), pp.19659-19671

Buxbaum, J., 1986. Aberrant immunoglobulin synthesis in LC amyloidosis. Free LC and LC fragment production by human bone marrow cells in short-term tissue culture. *The Journal of clinical investigation*, *78*(3), pp.798-806

Cai, Y., Xu, S., Li, N., Li, S. and Xu, G., 2020. Efficacy of chemotherapies and stem cell transplantation for systemic AL amyloidosis: a network meta-analysis. *Frontiers in pharmacology*, *10*, p.1601

Cheng, Y., Grigorieff, N., Penczek, P.A. and Walz, T., 2015. A primer to single-particle cryo-electron microscopy. *Cell*, *161*(3), pp.438-449

Close, W., Neumann, M., Schmidt, A., Hora, M., Annamalai, K., Schmidt, M., Reif, B., Schmidt, V., Grigorieff, N. and Fändrich, M., 2018. Physical basis of amyloid fibril polymorphism. *Nature communications*, *9*(1), pp.1-7

Cohen, A.S. and Calkins, E., 1959. Electron microscopic observations on a fibrous component in amyloid of diverse origins. *Nature*, *183*(4669), pp.1202-1203

Cohen, S. and Porter, R.R., 1964. Structure and biological activity of immunoglobulins. *Advances in immunology*, *4*, pp.287-349

Crowther, R.A. and Wischik, C.M., 1985. Image reconstruction of the Alzheimer paired helical filament. *The EMBO journal*, *4*(13B), pp.3661-3665

Davis, M.K., Kale, P., Liedtke, M., Schrier, S., Arai, S., Wheeler, M., Lafayette, R., Coakley, T. and Witteles, R.M., 2015. Outcomes after heart transplantation for amyloid cardiomyopathy in the modern era. *American Journal of Transplantation*, *15*(3), pp.650-658

De Rosier, D.J. and Klug, A., 1968. Reconstruction of three dimensional structures from electron micrographs. *Nature*, *217*(5124), pp.130-134

Deshmukh, M., Elderfield, K., Rahemtulla, A. and Naresh, K.N., 2009. Immunophenotype of neoplastic plasma cells in AL amyloidosis. *Journal of clinical pathology*, *62*(8), pp.724-730

Dispenzieri, A., Kyle, R.A., Lacy, M.Q., Jaffe, A.S., Therneau, T.M., Zeldenrust, S.R. and Gertz, M.A., 2004. Serum cardiac troponins and N-terminal pro-brain natriuretic peptide: a staging system for primary systemic amyloidosis. *Amyloid and Amyloidosis*, pp.67-69

Dispenzieri, A., Larson, D.R., Rajkumar, S.V., Kyle, R.A., Kumar, S.K., Kourelis, T., Arendt, B., Willrcih, M., Dasari, S. and Murray, D., 2020. N-glycosylation of monoclonal LCs on routine MASS-FIX testing is a risk factor for MGUS progression. *Leukemia*, *34*(10), pp.2749-2753

Dobson, C.M., 2003. Protein folding and misfolding. *Nature*, *426*(6968), pp.884-890

Dreyer, W.J. and Bennett, J.C., 1965. The molecular basis of antibody formation: a paradox. *Proceedings of the National Academy of Sciences of the United States of America*, *54*(3), p.864

Dubochet, J. and McDowall, A.W., 1981. Vitrification of pure water for electron microscopy. *Journal of Microscopy*, *124*(3), pp.3-4

Eanes, E.D. and Glenner, G.G., 1968. X-ray diffraction studies on amyloid filaments. *Journal of Histochemistry & Cytochemistry*, *16*(11), pp.673-677

Edelman, G.M. and Benacerraf, B., 1962. On structural and functional relations between antibodies and proteins of the gamma-system. *Proceedings of the National Academy of Sciences of the United States of America*, *48*(6), p.1035

Edmundson, A.B., Ely, K.R., Abola, E.E., Schiffer, M. and Panagiotopoulos, N., 1975. Rotational allomerism and divergent evolution of domains in immunoglobulin LCs. *Biochemistry*, *14*(18), pp.3953-3961

Egerton, R.F., 2005. *Physical principles of electron microscopy* (Vol. 56). New York: Springer

Eisenberg, D.S. and Sawaya, M.R., 2017. Structural studies of amyloid proteins at the molecular level. *Annual review of biochemistry*, *86*, pp.69-95

Enqvist, S., Sletten, K. and Westermark, P., 2009. Fibril protein fragmentation pattern in systemic AL amyloidosis. *The Journal of Pathology: A Journal of the Pathological Society of Great Britain and Ireland*, *219*(4), pp.473-480

Falcon, B., Zhang, W., Murzin, A.G., Murshudov, G., Garringer, H.J., Vidal, R., Crowther, R.A., Ghetti, B., Scheres, S.H. and Goedert, M., 2018. Structures of filaments from Pick's disease reveal a novel tau protein fold. *Nature*, *561*(7721), pp.137-140

Falcon, B., Zivanov, J., Zhang, W., Murzin, A.G., Garringer, H.J., Vidal, R., Crowther, R.A., Newell, K.L., Ghetti, B., Goedert, M. and Scheres, S.H., 2019. Novel tau filament fold in chronic traumatic encephalopathy encloses hydrophobic molecules. *Nature*, *568*(7752), pp.420-423

Fändrich, M., 2007. On the structural definition of amyloid fibrils and other polypeptide aggregates. *Cellular and Molecular Life Sciences*, *64*(16), pp.2066-2078

Fändrich, M., Nyström, S., Nilsson, K.P.R., Böckmann, A., LeVine III, H. and Hammarström, P., 2018. Amyloid fibril polymorphism: a challenge for molecular imaging and therapy. *Journal of internal medicine*, *283*(3), pp.218-237

Fernández de Larrea, C., Verga, L., Morbini, P., Klersy, C., Lavatelli, F., Foli, A., Obici, L., Milani, P., Capello, G.L., Paulli, M. and Palladini, G., 2015. A practical approach to the diagnosis of systemic amyloidoses. *Blood 125*(14), pp.2239-2244

Ferreira, S.T., De Felice, F.G. and Chapeaurouge, A., 2006. Metastable, partially folded states in the productive folding and in the misfolding and amyloid aggregation of proteins. *Cell biochemistry and biophysics*, *44*(3), pp.539-548

Fitzpatrick, A.W., Falcon, B., He, S., Murzin, A.G., Murshudov, G., Garringer, H.J., Crowther, R.A., Ghetti, B., Goedert, M. and Scheres, S.H., 2017. Cryo-EM structures of tau filaments from Alzheimer's disease. *Nature*, *547*(7662), pp.185-190

Fleischman, J.B., Porter, R.R. and Press, E.M., 1963. The arrangement of the peptide chains in γ-globulin. *Biochemical Journal*, *88*(2), p.220

Fotiou, D., Dimopoulos, M.A. and Kastritis, E., 2020. Systemic AL Amyloidosis: current approaches to diagnosis and management. *HemaSphere*, *4*(4)

Gertz, M.A., Greipp, P.R. and Kyle, R.A., 1991. Classification of amyloidosis by the detection of clonal excess of plasma cells in the bone marrow. *The Journal of laboratory and clinical medicine*, *118*(1), pp.33-39

Glenner, G.G., Ein, D., Eanes, E.D., Bladen, H.A., Terry, W. and Page, D.L., 1971. Creation of "amyloid" fibrils from Bence Jones proteins in vitro. *Science*, *174*(4010), pp.712-714

Glenner, G.G., Harbaugh, J., Ohms, J.I., Harada, M. and Cuatrecasas, P., 1970. An amyloid protein: the amino-terminal variable fragment of an immunoglobulin LC. *Biochemical and biophysical research communications*, *41*(5), pp.1287-1289

Goedert, M. and Spillantini, M.G., 2006. A century of Alzheimer's disease. *Science*, *314*(5800), pp.777-781

Goldsbury, C.S., Cooper, G.J., Goldie, K.N., Müller, S.A., Saafi, E.L., Gruijters, W.T.M., Misur, M.P., Engel, A., Aebi, U. and Kistler, J., 1997. Polymorphic fibrillar assembly of human amylin. *Journal of structural biology*, *119*(1), pp.17-27

Granzow, M., Hegenbart, U., Hinderhofer, K., Hose, D., Seckinger, A., Bochtler, T., Hemminki, K., Goldschmidt, H., Schönland, S.O. and Jauch, A., 2017. Novel recurrent chromosomal aberrations detected in clonal plasma cells of LC amyloidosis patients show potential adverse prognostic effect: first results from a genome-wide copy number array analysis. *Haematologica*, *102*(7), p.1281

Guerrero-Ferreira, R., Taylor, N.M., Arteni, A.A., Kumari, P., Mona, D., Ringler, P., Britschgi, M., Lauer, M.E., Makky, A., Verasdonck, J. and Riek, R., 2019. Two new polymorphic

structures of human full-length alpha-synuclein fibrils solved by cryo-electron microscopy. *Elife*, *8*, p.e48907

Guerrero-Ferreira, R., Taylor, N.M., Mona, D., Ringler, P., Lauer, M.E., Riek, R., Britschgi, M. and Stahlberg, H., 2018. Cryo-EM structure of alpha-synuclein fibrils. *Elife*, *7*, p.e36402

He, S. and Scheres, S.H., 2017. Helical reconstruction in RELION. *Journal of structural biology*, *198*(3), pp.163-176

Hilschmann, N. and Craig, L.C., 1965. Amino acid sequence studies with Bence-Jones proteins. *Proceedings of the National Academy of Sciences of the United States of America*, *53*(6), p.1403

Hoult, D.I. and Bhakar, B., 1997. NMR signal reception: Virtual photons and coherent spontaneous emission. *Concepts in Magnetic Resonance: An Educational Journal*, *9*(5), pp.277-297

Hozumi, N. and Tonegawa, S., 1976. Evidence for somatic rearrangement of immunoglobulin genes coding for variable and constant regions. *Proceedings of the National Academy of Sciences*, *73*(10), pp.3628-3632

Hurle, M.R., Helms, L.R., Li, L.I.N., Chan, W. and Wetzel, R., 1994. A role for destabilizing amino acid replacements in light-chain amyloidosis. *Proceedings of the National Academy of Sciences*, *91*(12), pp.5446-5450

Jones, T.A., 1985. Interactive computer graphics: FRODO. *Methods in enzymology*, *115*, pp.157-171

Kastritis, E., Leleu, X., Arnulf, B., Zamagni, E., Cibeira, M.T., Kwok, F., Mollee, P., Hájek, R., Moreau, P., Jaccard, A. and Schönland, S.O., 2020. Bortezomib, melphalan, and dexamethasone for light-chain amyloidosis. *Journal of Clinical Oncology*, *38*(28), pp.3252-3260

Katzmann, J.A., Clark, R.J., Abraham, R.S., Bryant, S., Lymp, J.F., Bradwell, A.R. and Kyle, R.A., 2002. Serum reference intervals and diagnostic ranges for free κ and free λ immunoglobulin LCs: relative sensitivity for detection of monoclonal LCs. *Clinical chemistry*, *48*(9), pp.1437-1444

Kazman, P., Vielberg, M.T., Cendales, M.D.P., Hunziger, L., Weber, B., Hegenbart, U., Zacharias, M., Köhler, R., Schönland, S., Groll, M. and Buchner, J., 2020. Fatal amyloid formation in a patient's antibody LC is caused by a single point mutation. *Elife*, *9*, p.e52300

Klafki, H.W., Kratzin, H.D., Pick, A.I., Eckart, K., Karas, M. and Hilschmann, N., 1992. Complete amino acid sequence determinations demonstrate identity of the urinary Bence Jones protein (BJP-DIA) and the amyloid fibril protein (AL-DIA) in a case of AL-amyloidosis. *Biochemistry*, *31*(12), pp.3265-3272

Klimtchuk, E.S., Gursky, O., Patel, R.S., Laporte, K.L., Connors, L.H., Skinner, M. and Seldin, D.C., 2010. The critical role of the constant region in thermal stability and aggregation of amyloidogenic immunoglobulin LC. *Biochemistry*, *49*(45), pp.9848-9857

Knowles, T.P., Vendruscolo, M. and Dobson, C.M., 2014. The amyloid state and its association with protein misfolding diseases. *Nature reviews Molecular cell biology*, *15*(6), pp.384-396

Kollmer, M., Close, W., Funk, L., Rasmussen, J., Bsoul, A., Schierhorn, A., Schmidt, M., Sigurdson, C.J., Jucker, M. and Fändrich, M., 2019. Cryo-EM structure and polymorphism of Aβ amyloid fibrils purified from Alzheimer's brain tissue. *Nature communications*, *10*(1), pp.1-8

Kourelis, T.V., Dasari, S., Theis, J.D., Ramirez-Alvarado, M., Kurtin, P.J., Gertz, M.A., Zeldenrust, S.R., Zenka, R.M., Dogan, A. and Dispenzieri, A., 2017. Clarifying immunoglobulin gene usage in systemic and localized immunoglobulin light-chain amyloidosis by mass spectrometry. *Blood 129*(3), pp.299-306

Kristen, A.V., Kreusser, M.M., Blum, P., Schönland, S.O., Frankenstein, L., Dösch, A.O., Knop, B., Helmschrott, M., Schmack, B., Ruhparwar, A. and Hegenbart, U., 2018. Improved outcomes after heart transplantation for cardiac amyloidosis in the modern era. *The journal of heart and lung transplantation*, *37*(5), pp.611-618

Kumar, S., Dispenzieri, A., Lacy, M.Q., Hayman, S.R., Buadi, F.K., Colby, C., Laumann, K., Zeldenrust, S.R., Leung, N., Dingli, D. and Greipp, P.R., 2012. Revised prognostic staging system for light chain amyloidosis incorporating cardiac biomarkers and serum free light chain measurements. *Journal of Clinical Oncology*, *30*(9), p.989

Kumar, S., Murray, D., Dasari, S., Milani, P., Barnidge, D., Madden, B., Kourelis, T., Arendt, B., Merlini, G., Ramirez-Alvarado, M. and Dispenzieri, A., 2019. Assay to rapidly screen for immunoglobulin LC glycosylation: a potential path to earlier AL diagnosis for a subset of patients. *Leukemia*, *33*(1), pp.254-257

Kurouski, D., 2016. *Supramolecular organization of amyloid fibrils* (pp. 73-98). IntechOpen

Lavatelli, F., Mazzini, G., Ricagno, S., Iavarone, F., Rognoni, P., Milani, P., Nuvolone, M., Swuec, P., Caminito, S., Tasaki, M. and Chaves-Sanjuan, A., 2020. Mass spectrometry characterization of LC fragmentation sites in cardiac AL amyloidosis: insights into the timing of proteolysis. *Journal of Biological Chemistry*, *295*(49), pp.16572-16584

Lecoq, L., Wiegand, T., Rodriguez-Alvarez, F.J., Cadalbert, R., Herrera, G.A., del Pozo-Yauner, L., Meier, B.H. and Böckmann, A., 2019. A Substantial Structural Conversion of the Native Monomer Leads to in-Register Parallel Amyloid Fibril Formation in Light-Chain Amyloidosis. *Chembiochem*, *20*(8), pp.1027-1031

Lefranc, M.P., 2001. IMGT, the international ImMunoGeneTics database. *Nucleic acids research*, *29*(1), pp.207-209

Li, B., Ge, P., Murray, K.A., Sheth, P., Zhang, M., Nair, G., Sawaya, M.R., Shin, W.S., Boyer, D.R., Ye, S. and Eisenberg, D.S., 2018. Cryo-EM of full-length α-synuclein reveals fibril polymorphs with a common structural kernel. *Nature communications*, *9*(1), pp.1-10

Liberta, F., Loerch, S., Rennegarbe, M., Schierhorn, A., Westermark, P., Westermark, G.T., Hazenberg, B.P., Grigorieff, N., Fändrich, M. and Schmidt, M., 2019. Cryo-EM fibril structures from systemic AA amyloidosis reveal the species complementarity of pathological amyloids. *Nature communications*, *10*(1), pp.1-10

Lilleness, B., Ruberg, F.L., Mussinelli, R., Doros, G. and Sanchorawala, V., 2019. Development and validation of a survival staging system incorporating BNP in patients with LC amyloidosis. *Blood 133*(3), pp.215-223

Lim, A., Wally, J., Walsh, M.T., Skinner, M. and Costello, C.E., 2001. Identification and location of a cysteinyl posttranslational modification in an amyloidogenic κ1 LC protein by electrospray ionization and matrix-assisted laser desorption/ionization mass spectrometry. *Analytical biochemistry*, *295*(1), pp.45-56

Lu, Y., Jiang, Y., Prokaeva, T., Connors, L.H. and Costello, C.E., 2017. Oxidative post-translational modifications of an amyloidogenic immunoglobulin LC protein. *International journal of mass spectrometry*, *416*, pp.71-79

Mahmood, S., Bridoux, F., Venner, C.P., Sachchithanantham, S., Gilbertson, J.A., Rowczenio, D., Wagner, T., Sayed, R., Patel, K., Fontana, M. and Whelan, C.J., 2015. Natural history and outcomes in localised immunoglobulin light-chain amyloidosis: a long-term observational study. *The Lancet Haematology*, *2*(6), pp.e241-e250

Manwani, R., Foard, D., Mahmood, S., Sachchithanantham, S., Lane, T., Quarta, C., Youngstein, T., Rezk, T., Lachmann, H.J., Gillmore, J.D. and Fontana, M., 2018. Rapid hematologic responses improve outcomes in patients with very advanced (stage IIIb) cardiac immunoglobulin LC amyloidosis. *Haematologica*, *103*(4), p.e165

Marin-Argany, M., Güell-Bosch, J., Blancas-Mejía, L.M., Villegas, S. and Ramirez-Alvarado, M., 2015. Mutations can cause LCs to be too stable or too unstable to form amyloid fibrils. *Protein Science*, *24*(11), pp.1829-1840

McCausland, K.L., White, M.K., Guthrie, S.D., Quock, T., Finkel, M., Lousada, I. and Bayliss, M.S., 2018. LC (AL) amyloidosis: the journey to diagnosis. *The Patient-Patient-Centered Outcomes Research*, *11*(2), pp.207-216.

McDowall, A.W., Chang, J.J., Freeman, R., Lepault, J., Walter, C.A. and Dubochet, J., 1983. Electron microscopy of frozen hydrated sections of vitreous ice and vitrified biological samples. *Journal of microscopy*, *131*(1), pp.1-9

Mellors, P.W., Dasari, S., Kohlhagen, M.C., Kourelis, T., Go, R.S., Muchtar, E., Gertz, M.A., Kumar, S.K., Buadi, F.K., Willrich, M.A. and Lust, J.A., 2021. MASS-FIX for the detection of monoclonal proteins and LC N-glycosylation in routine clinical practice: a cross-sectional study of 6315 patients. *Blood cancer journal*, *11*(3), pp.1-9

Merlini, G., 2017. AL amyloidosis: from molecular mechanisms to targeted therapies. *Hematology 2014, the American Society of Hematology Education Program Book*, *2017*(1), pp.1-12

Morgan, G.J. and Kelly, J.W., 2016. The kinetic stability of a full-length antibody LC dimer determines whether endoproteolysis can release amyloidogenic variable domains. *Journal of molecular biology*, *428*(21), pp.4280-4297

Morgan, G.J., Yan, N.L., Mortenson, D.E., Rennella, E., Blundon, J.M., Gwin, R.M., Lin, C.Y., Stanfield, R.L., Brown, S.J., Rosen, H. and Spicer, T.P., 2019. Stabilization of amyloidogenic immunoglobulin LCs by small molecules. *Proceedings of the National Academy of Sciences*, *116*(17), pp.8360-8369

Murphy, K. and Weaver, C., 2016. *Janeway's immunobiology*. Garland science

Nelson, R., Sawaya, M.R., Balbirnie, M., Madsen, A.Ø., Riekel, C., Grothe, R. and Eisenberg, D., 2005. Structure of the cross-β spine of amyloid-like fibrils. *Nature*, *435*(7043), pp.773-778

Nokwe, C.N., Hora, M., Zacharias, M., Yagi, H., Peschek, J., Reif, B., Goto, Y. and Buchner, J., 2016. A stable mutant predisposes antibody domains to amyloid formation through specific non-native interactions. *Journal of molecular biology*, *428*(6), pp.1315-1332

Oberti, L., Rognoni, P., Barbiroli, A., Lavatelli, F., Russo, R., Maritan, M., Palladini, G., Bolognesi, M., Merlini, G. and Ricagno, S., 2017. Concurrent structural and biophysical traits link with immunoglobulin LCs amyloid propensity. *Scientific reports*, *7*(1), pp.1-11

Omtvedt, L.A., Husby, G., Cornwell Iii, G.G., Kyle, R.A. and Sletten, K., 1997. The amino acid sequence of the glycosylated amyloid immunoglobulin LC protein AL MS. *Scandinavian journal of immunology*, *45*(5), pp.551-556

Pedersen, J.S., Andersen, C.B. and Otzen, D.E., 2010. Amyloid structure–one but not the same: the many levels of fibrillar polymorphism. *The FEBS journal*, *277*(22), pp.4591-4601

Pepys, M.B., Rademacher, T.W., Amatayakul-Chantler, S., Williams, P., Noble, G.E., Hutchinson, W.L., Hawkins, P.N., Nelson, S.R., Gallimore, J.R. and Herbert, J., 1994. Human serum amyloid P component is an invariant constituent of amyloid deposits and has a uniquely homogeneous glycostructure. *Proceedings of the National Academy of Sciences*, *91*(12), pp.5602-5606

Perfetti, V., Garini, P., Vignarelli, M.C., Marinone, M.G., Zorzoli, I. and Merlini, G., 1995. Diagnostic approach to and follow-up of difficult cases of AL amyloidosis. *Haematologica*, *80*(5), pp.409-415

Perfetti, V., Palladini, G., Casarini, S., Navazza, V., Rognoni, P., Obici, L., Invernizzi, R., Perlini, S., Klersy, C. and Merlini, G., 2012. The repertoire of λ LCs causing predominant

amyloid heart involvement and identification of a preferentially involved germline gene, IGLV1-44. *Blood 119*(1), pp.144-150

Piehl, D.W., Blancas-Mejía, L.M., Ramirez-Alvarado, M. and Rienstra, C.M., 2017a. Solid-state NMR chemical shift assignments for AL-09 V L immunoglobulin LC fibrils. *Biomolecular NMR assignments*, *11*(1), pp.45-50

Piehl, D.W., Blancas-Mejía, L.M., Wall, J.S., Kennel, S.J., Ramirez-Alvarado, M. and Rienstra, C.M., 2017b. Immunoglobulin LCs form an extensive and highly ordered fibril involving the N-and C-termini. *ACS omega*, *2*(2), pp.712-720.

Porter, R.R., 1967. The structure of antibodies. *Scientific American*, *217*(4), pp.81-93

Poshusta, T.L., Sikkink, L.A., Leung, N., Clark, R.J., Dispenzieri, A. and Ramirez-Alvarado, M., 2009. Mutations in specific structural regions of immunoglobulin LCs are associated with free LC levels in patients with AL amyloidosis. *PloS one*, *4*(4), p.e5169

Pradhan, T., Annamalai, K., Sarkar, R., Hegenbart, U., Schönland, S., Fändrich, M. and Reif, B., 2021. Solid state NMR assignments of a human λ-III immunoglobulin LC amyloid fibril. *Biomolecular NMR Assignments*, *15*(1), pp.9-16

Pradhan, T., Annamalai, K., Sarkar, R., Huhn, S., Hegenbart, U., Schönland, S., Fändrich, M. and Reif, B., 2020. Seeded fibrils of the germline variant of human λ-III immunoglobulin LC FOR005 have a similar core as patient fibrils with reduced stability. *Journal of Biological Chemistry*, *295*(52), pp.18474-18484

Pras, M., Schubert, M., Zucker-Franklin, D., Rimon, A. and Franklin, E.C., 1968. The characterization of soluble amyloid prepared in water. *The Journal of clinical investigation*, *47*(4), pp.924-933

Quock, T.P., Yan, T., Chang, E., Guthrie, S. and Broder, M.S., 2018. Epidemiology of AL amyloidosis: a real-world study using US claims data. *Blood advances*, *2*(10), pp.1046-1053

Romhányi, G., 1971. Selective differentiation between amyloid and connective tissue structures based on the collagen specific topo-optical staining reaction with Congo red. *Virchows Archiv A*, *354*(3), pp.209-222

Rottenaicher, G.J., Weber, B., Rührnößl, F., Kazman, P., Absmeier, R.M., Hitzenberger, M., Zacharias, M. and Buchner, J., 2021. Molecular mechanism of amyloidogenic mutations in hypervariable regions of antibody LCs. *Journal of Biological Chemistry*, *296*

Sakano, H., Maki, R., Kurosawa, Y., Roeder, W. and Tonegawa, S., 1980. Two types of somatic recombination are necessary for the generation of complete immunoglobulin heavy-chain genes. *Nature*, *286*(5774), pp.676-683

Sawaya, M.R., Sambashivan, S., Nelson, R., Ivanova, M.I., Sievers, S.A., Apostol, M.I., Thompson, M.J., Balbirnie, M., Wiltzius, J.J., McFarlane, H.T. and Madsen, A.Ø., 2007. Atomic structures of amyloid cross-β spines reveal varied steric zippers. *Nature*, *447*(7143), pp.453-457

Scheres, S.H., 2012. RELION: implementation of a Bayesian approach to cryo-EM structure determination. *Journal of structural biology*, *180*(3), pp.519-530

Scheres, S.H., Zhang, W., Falcon, B. and Goedert, M., 2020. Cryo-EM structures of tau filaments. *Current Opinion in Structural Biology*, *64*, pp.17-25

Schmidt, A., Annamalai, K., Schmidt, M., Grigorieff, N. and Fändrich, M., 2016. Cryo-EM reveals the steric zipper structure of an LC-derived amyloid fibril. *Proceedings of the National Academy of Sciences*, *113*(22), pp.6200-6205

Schmidt, M., Wiese, S., Adak, V., Engler, J., Agarwal, S., Fritz, G., Westermark, P., Zacharias, M. and Fändrich, M., 2019. Cryo-EM structure of a transthyretin-derived amyloid fibril from a patient with hereditary ATTR amyloidosis. *Nature communications*, *10*(1), pp.1-9

Schönland, S.O., Hegenbart, U., Bochtler, T., Mangatter, A., Hansberg, M., Ho, A.D., Lohse, P. and Röcken, C., 2012. Immunohistochemistry in the classification of systemic forms of amyloidosis: a systematic investigation of 117 patients. *Blood 119*(2), pp.488-493

Schroeder, J.S., Billingham, M.E. and Rider, A.K., 1975. Cardiac amyloidosis: diagnosis by transvenous endomyocardial biopsy. *The American journal of medicine*, *59*(2), pp.269-273

Schweighauser, M., Shi, Y., Tarutani, A., Kametani, F., Murzin, A.G., Ghetti, B., Matsubara, T., Tomita, T., Ando, T., Hasegawa, K. and Murayama, S., 2020. Structures of α-synuclein filaments from multiple system atrophy. *Nature*, *585*(7825), pp.464-469

Serpell, L.C., Sunde, M., Benson, M.D., Tennent, G.A., Pepys, M.B. and Fraser, P.E., 2000. The protofilament substructure of amyloid fibrils. *Journal of molecular biology*, *300*(5), pp.1033-1039

Shimazaki, C., 2019. Current diagnosis and treatment of AL amyloidosis in Japan: a nationwide epidemiological survey. *[Rinsho ketsueki] The Japanese journal of clinical hematology*, *60*(8), pp.973-978

Sikkink, L.A. and Ramirez-Alvarado, M., 2008. Biochemical and aggregation analysis of Bence Jones proteins from different LC diseases. *Amyloid*, *15*(1), pp.29-39

Staron, A., Zheng, L., Doros, G., Connors, L.H., Mendelson, L.M., Joshi, T. and Sanchorawala, V., 2021. Marked progress in AL amyloidosis survival: a 40-year longitudinal natural history study. *Blood Cancer Journal*, *11*(8), pp.1-1

Sunde, M., Serpell, L.C., Bartlam, M., Fraser, P.E., Pepys, M.B. and Blake, C.C., 1997. Common core structure of amyloid fibrils by synchrotron X-ray diffraction. *Journal of molecular biology*, *273*(3), pp.729-739

Swuec, P., Lavatelli, F., Tasaki, M., Paissoni, C., Rognoni, P., Maritan, M., Brambilla, F., Milani, P., Mauri, P., Camilloni, C. and Palladini, G., 2019. Cryo-EM structure of cardiac

amyloid fibrils from an immunoglobulin light chain AL amyloidosis patient. *Nature communications*, *10*(1), pp.1-9

Symmers, W.S.C., 1956. Primary amyloidosis: a review. *Journal of clinical pathology*, *9*(3), p.187

Tonegawa, S., 1983. Somatic generation of antibody diversity. *Nature*, *302*(5909), pp.575-581

Valentine, R.C. and Green, N.M., 1967. Electron microscopy of an antibody-hapten complex. *Journal of molecular biology*, *27*(3), pp.615-617

Varr, B.C., Liedtke, M., Arai, S., Lafayette, R.A., Schrier, S.L. and Witteles, R.M., 2012. Heart transplantation and cardiac amyloidosis: approach to screening and novel management strategies. *The Journal of heart and lung transplantation*, *31*(3), pp.325-331

Vrana, J.A., Gamez, J.D., Madden, B.J., Theis, J.D., Bergen III, H.R. and Dogan, A., 2009. Classification of amyloidosis by laser microdissection and mass spectrometry–based proteomic analysis in clinical biopsy specimens. *Blood 114*(24), pp.4957-4959

Wechalekar, A.D., Gillmore, J.D. and Hawkins, P.N., 2016. Systemic amyloidosis. *The Lancet*, *387*(10038), pp.2641-2654

Wechalekar, A.D., Schonland, S.O., Kastritis, E., Gillmore, J.D., Dimopoulos, M.A., Lane, T., Foli, A., Foard, D., Milani, P., Rannigan, L. and Hegenbart, U., 2013. A European collaborative study of treatment outcomes in 346 patients with cardiac stage III AL amyloidosis. *Blood 121*(17), pp.3420-3427

Westermark, P. and Stenkvist, B., 1973. A new method for the diagnosis of systemic amyloidosis. *Archives of internal medicine*, *132*(4), pp.522-523

Wisniowski, B., McLeod, D.S., Adams, R., Harvey, Y., Brown, I., McGuire, L., Armes, J. and Mollee, P., 2019. The epidemiology of amyloidosis in Queensland, Australia. *British journal of haematology*, *186*(6), pp.829-836.

Wolf, B.C., Kumar, A., Vera, J.C. and Neiman, R.S., 1986. Bone marrow morphology and immunology in systemic amyloidosis. *American journal of clinical pathology*, *86*(1), pp.84-88

Woolfson, M.M. and Woolfson, M.M., 1997. *An introduction to X-ray crystallography*. Cambridge University Press

Wu, T.T. and Kabat, E.A., 1970. An analysis of the sequences of the variable regions of Bence Jones proteins and myeloman LCs and their implications for antibody complementarity. *Journal of Experimental Medicine*, *132*(2), pp.211-250

Yazaki, M., Liepnieks, J.J., Callaghan, J., Connolly, C.E. and Benson, M.D., 2004. Chemical characterization of a lambda I amyloid protein isolated from formalin-fixed and paraffin-embedded tissue sections. *Amyloid*, *11*(1), pp.50-55

Zhang, C., Huang, X. and Li, J., 2017. LC amyloidosis: Where are the LCs from and how they play their pathogenic role?. *Blood reviews*, *31*(4), pp.261-270

Zhang, W., Falcon, B., Murzin, A.G., Fan, J., Crowther, R.A., Goedert, M. and Scheres, S.H., 2019. Heparin-induced tau filaments are polymorphic and differ from those in Alzheimer's and Pick's diseases. *Elife*, *8*, p.e43584

List of Publications

Publication I:

"Cryo-EM structure of a light chain-derived amyloid fibril from a patient with systemic AL amyloidosis."

Radamaker, L., Lin, Y.H., Annamalai, K., Huhn, S., Hegenbart, U., Schönland, S.O., Fritz, G., Schmidt, M. and Fändrich, M.

Nature Communications **10,** 1103 (2019)

DOI: 10.1038/s41467-019-09032-0

Publication II:

"Cryo-EM reveals structural breaks in a patient-derived amyloid fibril from systemic AL amyloidosis."

Radamaker, L., Baur, J., Huhn, S., Haupt, C., Hegenbart, U., Schönland, S.O., Bansal, A., Schmidt, M. and Fändrich, M.

Nature Communications **12,** 875 (2021)

DOI: 10.1038/s41467-021-21126-2

Publication III:

“Role of mutations and post-translational modifications in systemic AL amyloidosis studied by cryo-EM”

Radamaker, L., Karimi-Farsijani, S., Andreotti, G., Baur, J., Neumann, M., Schreiner, S., Berghaus, N., Motika, R., Walther, P., Schmidt, V., Huhn, S., Hegenbart, U., Schönland, S.O., Wiese, S., Read, C., Schmidt, M. and Fändrich, M.

Manuscript accepted by Nature Communications

Publication I:

"Cryo-EM structure of a light chain-derived amyloid fibril from a patient with systemic AL amyloidosis." Radamaker, L., Lin, Y.H., Annamalai, K., Huhn, S., Hegenbart, U., Schönland, S.O., Fritz, G., Schmidt, M. and Fändrich, M. *Nature Communications* **10,** 1103 (2019).

DOI: 10.1038/s41467-019-09032-0.

Licensed under a Creative Commons Attribution 4.0 International License (CC BY 4.0), https://creativecommons.org/li

Contribution to publication I:

- Performed the research and analyzed the data presented in in SI Fig. 2,3,4,5d. Also Fig. 1a,b,c in co-operation with Matthias Schmidt and Karthikeyan Annamalai.
- Contributed to writing and revising the manuscript in co-operation with Marcus Fändrich, Matthias Schmidt and Yin-Hsi Lin.

Summary

In this publication, the cryo-EM structure of a cardiac ex vivo AL fibril is presented. The fibril is formed by a 91-residue LC fragment that shows ten mutational changes compared to the *IGLV1-44* germ line segment. The fibril protein fold shows three cavities: two water-filled and one with an additional density inclusion which is most likely of a hydrophobic nature. A higly acidic motif is buried in the fibril structure and the N- and C-termini are conformationally disordered. The fibril protein fold differs drastically from the native LC structure. The polypeptide chain shows a nearly flat and extended conformation in the amyloid fibril, whereas the fold is compact and globular in the native structure. In the fibril structure, the polypeptide chain runs anti-parallel around the disulfide bond, whereas it runs parallel in the native structure. This indicates that a 180° rotational switch has occurred during the process of misfolding.

nature COMMUNICATIONS

ARTICLE

https://doi.org/10.1038/s41467-019-09032-0 OPEN

Cryo-EM structure of a light chain-derived amyloid fibril from a patient with systemic AL amyloidosis

Lynn Radamaker[1], Yin-Hsi Lin[1], Karthikeyan Annamalai[1], Stefanie Huhn[2], Ute Hegenbart[3], Stefan O. Schönland[3], Günter Fritz[4,5], Matthias Schmidt[1] & Marcus Fändrich[1]

Amyloid fibrils derived from antibody light chains are key pathogenic agents in systemic AL amyloidosis. They can be deposited in multiple organs but cardiac amyloid is the major risk factor of mortality. Here we report the structure of a λ1 AL amyloid fibril from an explanted human heart at a resolution of 3.3 Å which we determined using cryo-electron microscopy. The fibril core consists of a 91-residue segment presenting an all-beta fold with ten mutagenic changes compared to the germ line. The conformation differs substantially from natively folded light chains: a rotational switch around the intramolecular disulphide bond being the crucial structural rearrangement underlying fibril formation. Our structure provides insight into the mechanism of protein misfolding and the role of patient-specific mutations in pathogenicity.

[1] Institute of Protein Biochemistry, Ulm University, 89081 Ulm, Germany. [2] Medical Department V, Section of Multiple Myeloma, Heidelberg University Hospital, 69120 Heidelberg, Germany. [3] Medical Department V, Amyloidosis Center, Heidelberg University Hospital, 69120 Heidelberg, Germany. [4] Institute of Microbiology, University of Hohenheim, 70599 Stuttgart, Germany. [5] Institute for Neuropathology, Faculty of Medicine, University of Freiburg, 79106 Freiburg, Germany. Correspondence and requests for materials should be addressed to M.F. (email: marcus.faendrich@uni-ulm.de)

Antibodies are protein structures of utmost importance to human health. They underlie the humoral immune system and many top-selling biopharmaceutical agents; yet, they can be the basis of devastating human diseases with systemic AL amyloidosis (i.e. the amyloidosis caused by immunoglobulin light chains) being a particularly important one[1]. Moreover, antibodies or antibody fragments can misfold during biopharmaceutical production, leading to a great need to improve our understanding of the misfolding of these proteins[2]. Systemic AL amyloidosis belongs to the most common forms of systemic amyloidosis in industrialized countries[3]. In the USA it occurs with an incidence of ~9–14 patients per 1 million inhabitants[4]. The misfolding of immunoglobulin light chains (LCs), which are constituents of natural antibodies[5], gives rise to the disease. Precondition is a clonal B cell disorder, such as a multiple myeloma, which elevates the concentration of one monoclonal LC in the serum.

The clinical and pathological disease manifestations are diverse and AL amyloid deposits can be found in different tissues and organs[6]. Especially important are those variants of the disease that are associated with cardiac amyloidosis. Cardiac involvement is a major cause of mortality[7]. Untreated patients show a median survival of 7 months after initial diagnosis[8]. The current treatment standard is to stop the production of LCs with chemotherapy directed against the underlying B cell clone. In case of advanced heart involvement, patients may additionally have to undergo a heart transplantation[9,10], which provides access to large quantities of amyloid fibrils for research purposes.

Several studies demonstrate that the properties of the precursor LCs predispose patients to develop the disease or a specific disease variant. There is a preponderance of λ-LCs versus κ-LCs (λ:κ = 3:1) in patients with AL amyloidosis, while κ-LCs are more abundant (λ:κ = 1:2) in healthy individuals and in patients with multiple myeloma[11]. Mutations in LC domains can destabilize the protein and/or accelerate the fibrillation of model proteins in vitro[12–15]. The presence of the *IGLV1-44* germ line segment in the LCs correlates positively with cardiomyopathy, while the *IGLV6-57* germ line segment correlates positively with kidney involvement[7,16–18].

Amyloid fibrils are much better established as pathogenic agents in systemic amyloidosis[19] than in many neurodegenerative amyloid diseases that rather depend on toxic amyloid oligomers[20]. Although free LCs or LC oligomers can make pathological contributions to systemic AL amyloidosis[7], cardiac pathology arises largely from massive amyloid fibril deposits that impair the natural ability of the heart to pump and to contract. So far, little is known about the structure of pathogenic LC aggregates. AL fibrils have generic structural characteristics of amyloid fibrils, such as a cross-β structure, a width of ~15 nm and a twisted fibril architecture leading to regularly spaced crossovers[21–23]. A deeper understanding of the mechanism of LC misfolding and consequent disease pathology is hampered by a lack of detailed structural information.

In this study, we used electron cryo microscopy (cryo-EM) to determine the molecular structure of an amyloid fibril underlying the pathology in an AL patient with severe cardiac amyloidosis. The fibrils were previously shown to consist of a LC fragment that corresponds to residues Val3–Ser118 of a λ-LC[22] and they match the size of other AL fibril proteins in cardiac amyloidosis[22,23]. The fibril protein is not glycosylated and encompasses mainly the variable light (V_L) domain, which is typical for λ-AL amyloidosis[13,22,23]. Using negatively stained transmission electron microscopy (TEM), we recently demonstrated that the fibrils from this patient contain a dominant fibril morphology, exhibiting a width of 13.6 ± 0.9 nm, and a minor morphology with a width of 20.4 ± 0.4 nm[23]. The cryo-EM structure of this dominant fibril morphology, which we present here, is informative about the mechanism of LC misfolding and illuminates the role of patient-specific mutations for the development of amyloidosis.

Results

Structural rigidity of the extracted fibrils. Using a previously established protocol to extract amyloid fibrils from diseased tissue[22], we obtained AL amyloid fibrils from heart muscle tissue of a patient who underwent a heart transplantation as a consequence of severe cardiac AL amyloidosis (Supplementary Table 1). The fibrils are derived from the germ line segments *IGLV1-44, IGLJ3*, and *IGLC2*, demonstrating that the fibrils are representative for a λ-subtype causing cardiac involvement. The dominant fibril morphology in the extract is relatively straight, indicating its resistance to bending deformations. Quantitatively, measurement of the fibril contour length and its end to end distance yielded values of 6.7 ± 0.5 μm for the persistence length and $2.78 \pm 0.21 \times 10^{-26}$ N m^2 for the bending rigidity (Supplementary Figure 1).

Fibril topology obtained by cryo-EM. Cryo-EM imaging of the extracted fibrils at 300 kV (Fig. 1a) allowed us to reconstruct the dominant fibril morphology at 3.3 Å resolution (Fig. 1b, Table 1) based on the 0.143 Fourier-shell correlation (FSC) criterion (Supplementary Figure 2). The two-dimensional (2D) class averages cover the entire fibril (Supplementary Figure 3). The reconstructed density shows a width of ~12 nm (Fig. 1b–d), in agreement with measurements from negatively stained samples[23]. The fibril consists of a single protein stack, termed here protofilament. It contains parallel cross-β sheets with intramolecular backbone hydrogen bonds (Fig. 2a, b). The fibril cross-section is asymmetrical (Fig. 1b), therefore a C1 symmetry was assumed during reconstruction. The fibril helix is left-hand twisted as confirmed by map-inversion and shows a pitch of ~300 nm as well as a polar topology (Fig. 1d).

Fold of the fibril protein. The three-dimensional (3D) cryo-EM map was fitted with a continuous polypeptide segment (Supplementary Table 2), corresponding to residues Gly15–Thr105 of the AL fibril protein (Fig. 2c, d). The protein N-terminal and C-terminal ends are juxtaposed in the structure and form a protruding stalk. The remaining part of the protein roughly outlines the shape of a ram head (Supplementary Figure 4). Head region and stalk lie on either side of an intramolecular disulfide bond that is formed between residues Cys22 and Cys89 (Fig. 2c, see below). The N-terminal and C-terminal ends of the stalk are surrounded by diffuse density (Supplementary Figure 4), indicating structural disorder of the first and last 12 residues (Fig. 2c).

The fibril protein belongs to the all-beta class of protein folds, consisting of 12 β-strands (β1–β12). The strands vary in length from two to eight residues. The folded structure shows several non-local contacts, such as between segments Gln16–Val18 and Asn97–Trp99, Cys22–Arg25 and Glu84–Cys89, Trp36–Gly58 and Thr70–Gln80, as well as Arg62–Lys67 and Asp83–Trp92. The polypeptide chain changes height by 8.2 Å along the fibril main axis (Supplementary Figure 5a), interdigitating the fibril proteins in the direction of the main axis. The intermolecular interactions in the fibril rarely extend beyond the next molecular layer. For example, strand β4 from layer *i* is in contact with strand β8 in layers *i* and *i* + 1 (Supplementary Figure 5b). Residue Arg25 interacts with residues Glu84 and Asp86 from layer *i* + 1 (Supplementary Figure 5c). The height change produces different tip structures at the two fibril ends (Supplementary Figure 5d), resembling other cross-β fibrils[24–28]. It was suggested that this

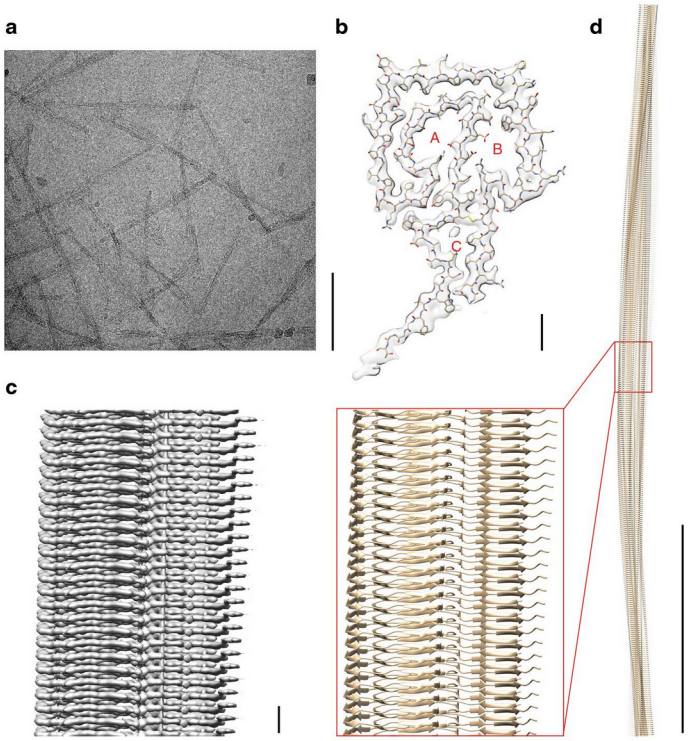

Fig. 1 Cryo-EM structure of an amyloid fibril from systemic AL amyloidosis. **a** Raw cryo-EM image. Scale bar: 100 nm. **b** Cross-section of the reconstruction superimposed with a molecular model. Three internal cavities are labeled A–C. Scale bar: 1 nm. **c** Side view of the reconstructed density. Scale bar: 1 nm. **d** Side views of the molecular model. A segment corresponding to the reconstruction (**c**) is boxed. Scale bar: 50 nm

Table 1 Cryo-EM data collection and image processing

Microscope	Titan Krios (Thermo Fisher Scientific)
Camera	K2 Summit (Gatan)
Acceleration voltage (kV)	300
Magnification	130,000
Defocus range (μm)	0.4–4.6
Dose rate (e^- pixel^{-1} s^{-1})	5.78
Number of movie frames	30
Exposure time (s)	6
Total electron dose (e^- Å^{-2})	32
Pixel size (Å)	1.041
Gatan imaging filter	20 eV
Mode	Counting mode
Box size (pixel)	320
Inter box distance (Å)	28.8
Number of extracted segments	119,395
Number of segments after 2D classification	62,250
Number of segments after 3D classification	32,677
Resolution, 0.143 FSC criterion (Å)	3.3
Map sharpening B-Factor (Å^2)	119.6
Helical rise (Å)	4.8
Helical twist (°)	0.58
Symmetry imposed	C1

fact may give rise to different mechanisms/kinetics of fibril outgrowth[26,29].

The protein fold encloses three major cavities, labeled A–C (Fig. 1b). Cavities A and B are hydrophilic and occur within the head region. They are lined with many polar and ionic amino acid side chains, suggesting the presence of water. Cavity C is hydrophobic and located within the stalk region. This cavity is lined with hydrophobic side chains and the intramolecular disulfide bond. It also contains a small density that cannot be assigned to the polypeptide chain (Fig. 1b), indicating the presence of a molecular inclusion of low polarity.

Location of sequence elements in the fibril protein. The most aggregation-prone segments of the protein exist at residues Asn97–Phe101, Lys46–Tyr50, Tyr87–Ala91, and Val34–Gln39 (Fig. 3a, Supplementary Table 3), similar to other λ1-LCs[30]. These segments do not correspond well with the β-strands in the fibril (Fig. 2a, c). Three segments are solvent-exposed, while residues Tyr87–Ala91 are buried (Fig. 3b). The fibril protein lacks a typical hydrophobic core (Fig. 2d). One of its most central structural elements is stand β9, which contains a highly acidic motif (Fig. 2d, Fig. 3c). The charges of this segment are only partially compensated by buried residues of the opposite charge (Arg25 and Lys73) (Fig. 2d). The complementarity determining regions (CDRs) are located on the fibril surface (Fig. 3d) and there are 10 mutations compared with the amino acid sequence encoded by the *IGLV1-44* germ line segment (Fig. 3d).

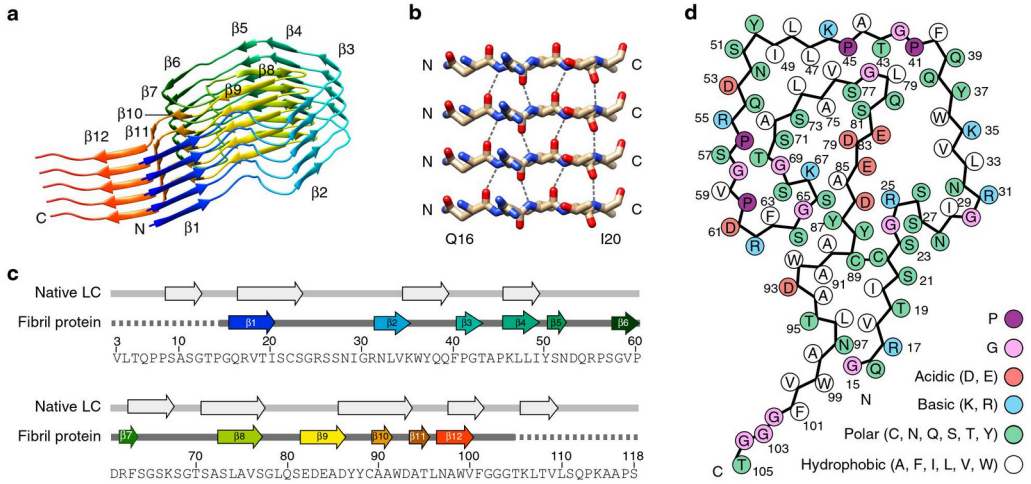

Fig. 2 Fibril protein β-sheet structure. **a** Ribbon representation of a stack of five fibril proteins rainbow colored from N-terminus to C-terminus. **b** Close-up of the parallel cross-β sheet β1. **c** Position of the β-strands (arrows) in the fibril protein and in the natively folded LC as defined in PDB entry 1BJM[60]. Residue numbers refer to the native LC without signal sequence. The color of the β-strands in the fibril corresponds to panel **a**. Dotted gray line refers to the part of the protein that is disordered in the fibril. **d** Schematic representation of the fibril protein packing

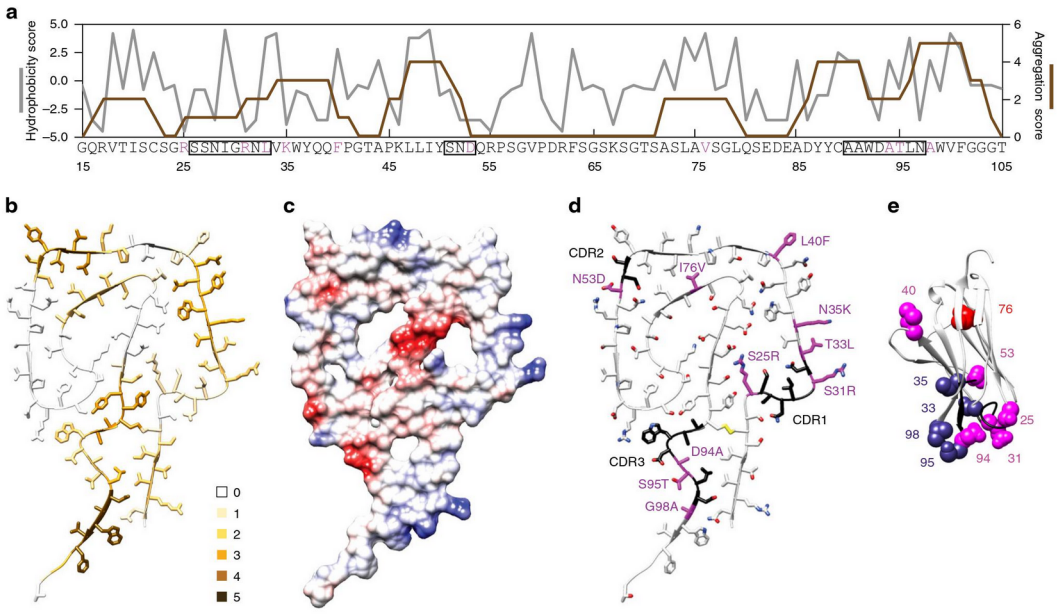

Fig. 3 Location of specific sequence elements in the structure. **a** Hydrophobicity (gray) and aggregation score (brown) of the ordered part of the fibril protein. Magenta letters: mutations compared to the *IGLV1-44* germ line segment. Boxes: CDRs. Residue numbers refer to the native LC without signal sequence. **b** Fibril protein showing the residue-specific aggregation score (0–5). **c** Electrostatic surface representation of the fibril protein. **d** Fibril protein with CDRs (black) and mutations (magenta) highlighted. **e** Ribbon diagram of a native V_L domain (PDB entry 1BJM)[60] showing residues 3–113. CDRs are colored black; mutations are colored in red if they affect the core (residue 76), purple (surface residues with potential relevance for domain–domain interactions), or magenta (other surface residues)

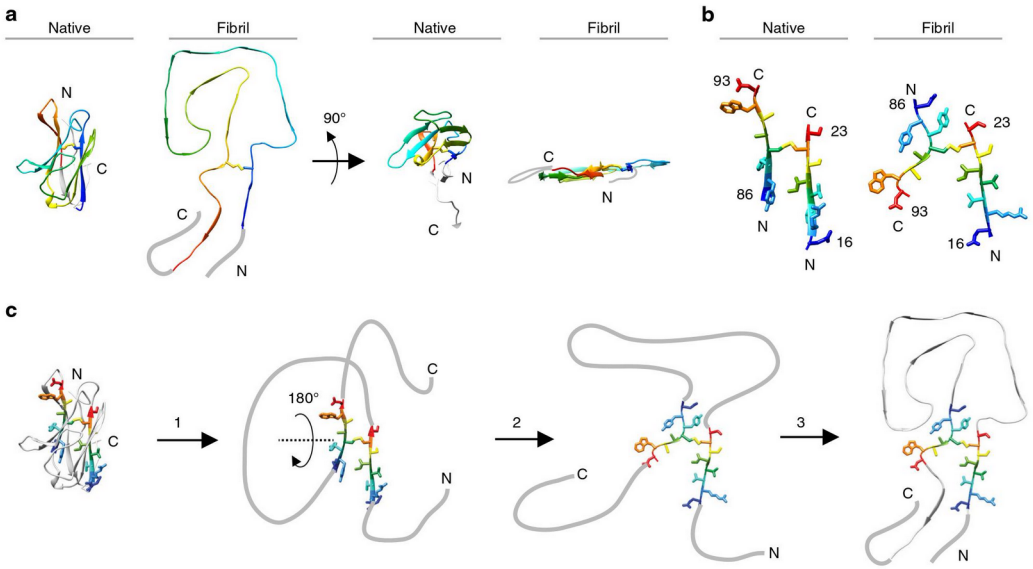

Fig. 4 Comparison of the fibril structure and the native V_L domain fold. **a** Comparison of the native V_L domain fold (PDB entry 1BJM)[60] with the fibril state. Residues 15–105 are shown in rainbow color. The native conformation is truncated at residue 118, corresponding to our fibril protein. The diffuse N-terminal and C-terminal tails of the fibril structure are schematically added with a gray line. **b** Part of the native structure and of the fibril state showing the conformational switch of segments 86–93 and 16–23 relative to one another around the protein disulfide bond. **c** Schematic representation of the hypothetical misfolding reaction consisting of an unfolding reaction (1), the rotational switch (2) and the assembly into the fibril structure (3)

Three of these mutations add a surface charge to the fibril (Ser31Arg, Asn35Lys, Asn53Asp) (Fig. 2d). One mutation removes a charge from the non-polar cavity C (Asp94Ala). Ser25Arg inserts a basic residue into the polar cavity B, where it helps to compensate the charges of Glu84 and Asp86 and to interdigitate two molecular layers of the fibril Supplementary Figure 5c). Gly98Ala occurs in the highly aggregation-prone segment at residues Asn97–Phe101 (Fig. 3a). Thr33Leu, Leu40Phe, Ile76Val, and Ser95Thr have no obvious structural effect on the fibril. None of the replacements is clearly unfavorable to the fibril structure. No mutational change occurs within the *IGLJ3* and *IGLC2* germ line segments, nor within residues Gln1–Thr13, a previously described mutational hot spot of some amyloidogenic λ-LCs[31]. This segment is conformationally disordered or missing in the fibril (Supplementary Figure 4), which implies that at least for some patients this segment is not relevant to fibril formation. Indeed, mutational changes to the N-terminus were found to be more relevant to a λ6-LC-derived V_L domain, which is destabilized upon mutation[32], and λ6-LCs may form fibrils with an ordered N-terminus[29,33].

Comparison with native LC conformations. The majority of the mutations occur at surface positions in the globular V_L domain (Fig. 3e). Four of these changes (Thr33Leu, Asn35Lys, Ser95Thr, Gly98Ala) may potentially impact the interactions with other immunoglobulin domains. Only Ile76Val affects a buried residue. This mutation removes a methylene group from the protein core, which typically destabilizes a protein by 6 kJ/mol[34]. Taken together, we find one out of 10 mutations in this patient to be unfavorable to the native state, while two to six changes make the LC more compatible with the fibril structure than the germ line segment.

The fibril structure is profoundly different from a natively folded V_L domain. Both protein states contain a high β-sheet content, but there are differences in the number and position of the β-strands within the sequence (Fig. 2c). The fibril conformation is more extended and flattened compared to the native state (Fig. 4a), enabling the polypeptide chain to form one molecular fibril layer. A particularly substantial structural rearrangement happens in the region around the disulfide bond which cross-links the N-terminal and C-terminal segments of the protein. These segments show a parallel N to C orientation in the native state and an antiparallel orientation in the fibril (Fig. 4b). Therefore, misfolding induces a 180° rotational switch of one segment relative to the other around the disulfide bond, placing the stalk on one side of the disulfide bond and the head region on the other (Fig. 4c). These stark structural differences between the native and misfolded state are consistent with our previous observation that AL amyloid fibrils and refolded fibril proteins differ in several structural features, such as their infrared spectral characteristics and their affinity for the amyloid-binding dyes Thioflavin T and Congo red[23].

Discussion

In this study, we have analyzed the molecular structure of an amyloid fibril that was purified from patient tissue and is therefore directly relevant to disease. Interestingly, we previously found that the fibril protein constituting this fibril is able to form amyloid-like fibrils in vitro that possess a different morphology, and possibly also a different protofilament substructure, than the bona fide pathogenic aggregates studied here[23]. These observations indicate that it is essential to investigate patient-derived rather than in vitro formed fibrils when scrutinizing the molecular basis of a protein misfolding disease.

The reconstructed fibril has an elongated and rigid structure, consisting of a single protofilament. Values measured for the bending rigidity of the AL fibrils ($2.78 \pm 0.21 \times 10^{-26}$ N m^2) correspond to previously reported values, which were on the

order of 10^{-28}–10^{-25} N m^2 for different amyloid-like fibrils[35]. The stiffness of the fibrils could explain why amyloid fibril deposits impair the natural function of the heart. Cryo-EM and reconstruction of the 3D map enabled us to reveal the molecular structure underlying these effects. We could show that residues Gly15–Thr105 adopt a stable conformation in the fibril, while the first and last 12 amino acid residues are not resolved in our structure and are conformationally disordered (Supplementary Figure 4). The fibril proteins are interdigitated along the main axis of the fibril, providing resilience to mechanical stress (Supplementary Figure 1). The fold of the AL fibril protein is novel and differs from previously published fibril protein structures. It consists of a head and stalk region and encompasses one non-polar and two polar cavities (Figs. 1b, 2d).

The single-protofilament architecture of this AL amyloid fibril contrasts with the majority of previously described cross-β fibrils, which consist of multiple protofilaments[24,26–28,36]. However, we cannot exclude the formation of multi-protofilament AL amyloid fibrils, as our sample contains a second fibril morphology that is thicker than the presently studied one[23]. Furthermore, the presently investigated fibril contains surface-exposed charge pairs, for example at residues Asp53 and Arg55, which were previously identified as protofilament–protofilament interaction sites in murine AA amyloid fibrils[28]. However, the majority of the fibrils in the AL fibril sample does not contain multiple protofilaments, indicating that the assembly into higher-order structures is unfavorable for this fibril protein.

The protein fold provides insight into the mechanism of LC misfolding. It does not support mechanisms that assume of the initial formation of fibril segments consisting of dimeric proteins or peptides[13,37,38]. Nor is there evidence for an assembly of domain-swapped molecules, consistent with other studies[37,39]. The substantial conformational differences between the fibril structure and the native state imply instead that the native conformation must be largely, if not entirely, unfolded to allow fibril formation to occur (Fig. 4c). In particular, we identified a rotational switch of the polypeptide chain around the disulfide bond that is only possible if most of the native strand–strand interactions are lost. Unfolding and the rotational switch are crucial for fibril formation as unfolding is the prerequisite for the rotational switch, which in turn represents the basis for the formation of a flat protein structure that lacks chain crossings (Fig. 4c). This conformation is then able to associate into the intermolecular hydrogen bond network of a cross-β sheet.

As the disulfide bond occurs at the same position in the fibril as in the native V_L domain, previous research suggested that the misfolding of the LC occurs under oxidizing conditions and maintains the cysteine disulfide bond[23]. Our structure lends further support to this view, as we reveal a number of notable imperfections in the fibril packing. There are three major internal cavities (Fig. 1b) and the protein is packed inside-out or outside-in. A highly acidic segment of low aggregation propensity is buried in the core and only partially compensated by basic charges, whereas segments that are much more hydrophobic and aggregation-prone are exposed to the solvent (Fig. 3b, c). The situation looks drastically different in systemic AA amyloidosis, where the most aggregation-prone and hydrophobic segments are buried in the fibril core and where buried acidic residues are compensated by an equal number of buried basic residues[28]. AA amyloid fibrils, which contain no disulfide bond, accomplish a tighter packing than AL amyloid fibrils and form much smaller internal cavities.

The detailed information provided by our structure helps to explain the effects of mutational variants in systemic AL amyloidosis. Several mutational changes have a beneficial effect on the fibril structure (Fig. 3d), while only one mutation is clearly unfavorable to the native protein conformation (Fig. 3e). The analyzed fibril is representative for amyloid fibrils from cardiac AL amyloidosis as it is derived from an *IGLV1-44* germ line segment, the major germ line segment leading to heart involvement[7,16–18]. The mass of the fibril protein corresponds to that of other AL fibril proteins and consists mainly of a V_L domain[22,23]. The observed fibril morphology resembles fibril morphologies from other AL patients with cardiomyopathy[22,23], despite clear patient-specific differences. However, systemic AL amyloidosis is an extraordinarily variable disease and other LC subtypes may be associated with different structural properties, particularly at the protein N-terminus, as was indicated recently for fibrils derived from λ6-LCs[29,33].

The current data from cryo-EM sheds light onto the misfolding of proteins and their pathogenicity, representing a solid basis for further investigation of molecular mechanisms underlying human pathology, for example by in vitro aggregation studies. Detailed knowledge of the molecular structure of pathogenic protein states may lead to the development of novel ligands which recognize these structures and form the basis of new detection methods or therapeutic strategies. However, due to the heterogeneity of systemic AL amyloidosis further work will be necessary to dissect the structural characteristics of fibrils from different groups of patients and to identify common structural themes between different cohorts of patients as well as systematic variations.

Methods

Source of AL fibrils. AL amyloid fibrils were extracted from the heart of a woman (Supplementary Table 1), suffering from advanced heart failure due to AL amyloidosis[22,23]. First symptoms (dyspnea, fatigue) started 1 year before diagnosis of AL amyloidosis. A monoclonal plasma cell disorder (smoldering myeloma) was diagnosed at the same time as AL amyloidosis. Bone marrow cytology showed 19% plasma cells (<5% λ-positive in bone marrow histology) and interphase fluorescence in situ-hybridization analysis of CD138+ enriched plasma cells showed the t (11;14) translocation and the 13q14 deletion. The patient received 5 months of treatment with bortezomib and dexamethasone, and achieved a serological complete remission of the smoldering myeloma. Ten months later, free λ-LCs increased and treatment with lenalidomide and dexamethasone was started but stopped after 2 months due to cardiac decompensation. 1 month later high urgency listing was done and the transplantation was performed 2 months later. Informed consent was obtained from the patient for the analysis of the amyloid deposits.

The fibril extraction was performed from heart muscle tissue as described previously[22]. In brief, 250 mg of tissue were diced and washed five times with 0.5 mL Tris calcium buffer (20 mM Tris, 138 mM NaCl, 2 mM $CaCl_2$, 0.1 % NaN_3, pH 8.0). Each washing step consisted of gentle vortexing and centrifugation at 3100 × *g* for 1 min at 4 °C. The supernatant was discarded and the pellet was resuspended in 1 mL of freshly prepared 5 mg mL^{-1}*Clostridium histolyticum* collagenase (Sigma) in Tris calcium buffer. After incubation overnight at 37 °C the tissue material was centrifuged at 3100 × *g* for 30 min at 4 °C. The retained pellet was resuspended in 0.5 mL buffer containing 20 mM Tris, 140 mM NaCl, 10 mM ethylenediaminetetraacetic acid, 0.1 % NaN_3, pH 8.0, and subjected to 10 cycles of homogenization in fresh buffer and centrifugation for 5 min at 3100 × *g* at 4 °C. The remaining pellet was homogenized in 0.5 mL ice cold water, centrifuged for 5 min at 3100 × *g* at 4 °C and the fibril-containing supernatant was analyzed. The study was approved by the ethical committees of the University of Heidelberg (123/2006) and of Ulm University (210/13)

Measurement of the persistence length. Patient-derived fibrils were dried onto a carbon-coated grid and negatively stained with uranyl acetate as described previously[22]. Images were taken at 120 kV using a JEM-1400Plus microscopy (Jeol) equipped with a TemCam-F216 camera (TVIPS). The contour length *L* and end-to-end distance *D* of 124 well-resolved fibrils was determined using the program Fiji (http://fiji.sc). The plot of the squared end-to-end distance was fit with Eq. (1) to obtain the persistence length *P*:

$$\langle D^2 \rangle = 4PL \cdot \left[1 - \frac{2P}{L}\left(1 - e^{(-L/2P)}\right)\right] \quad (1)$$

The persistence length can be converted into the bending rigidity *B* as described by:

$$B = P \cdot k_B \cdot T \quad (2)$$

In this equation, k_B refers to the Boltzmann constant and *T* to the temperature (300 K).

Cryo-EM. A 3.5 µL aliquot was applied to a glow-discharged holey carbon-coated grid (C-flat 1.2/1.3 400 mesh) blotted from the back side after an incubation time of 4 s at a humidity of >80% and plunge-frozen in liquid ethane using a Cryoplunge 3 System (Gatan). For image acquisition a K2-Summit detector (Gatan) in counting mode on a Titan Krios transmission electron microscope (Thermo Fisher Scientific) at 300 kV was used, using a Gatan imaging filter with a 20 eV slit. Table 1 lists the data acquisition parameters. The raw data have been deposited at https://www.ebi.ac.uk/pdbe/emdb/ with the accession code EMPIAR-10245.

Helical reconstruction. The raw data movie frames were gain-corrected with IMOD[40] and aligned, motion-corrected and dose-weighted using MOTIONCOR2[41]. Gctf[42] was used to estimate the contrast transfer function from the aligned and motion-corrected images. RELION 2.1[43] was used for the helical reconstruction of the fibril density. After manual selection of the fibrils from the aligned, motion-corrected micrographs, segments were extracted with a box size of ~333 Å and an inter-box distance of ~9% of the box length. Reference-free 2D classification with a regularization value of $T = 3$ produced class averages showing the helical repeat along the fibril axis. Class averages were selected based on a manual arrangement into a fibril structure. From the selected class averages, 200 randomly picked particles per class were used to generate an initial 3D model using the Stochastic Gradient Descent algorithm implemented in RELION. These initial models were low-pass filtered to 60 Å and used to generate a single-fibril model of two selected fibrils with clearly visible cross-overs. The single-fibril model showed the general shape of the fibril, and was then used as an initial model for 3D classification with $K = 4$. Two out of four classes were selected. The ~30k particles from these two classes were then used for a second 3D classification run with $T = 3$ using as a reference the model showing most features from the initial classification. This second classification produced a model showing the peptide backbone in the cross-section. Increasing the T-value to 20 and performing a third 3D-classification yielded a model showing a clear β-strand separation and some side-chain densities. Repeating the 3D-classification several times while increasing the T-value and decreasing the angular sampling rate further improved the model. Auto-refinement and post-processing with a soft-edged mask and an estimated map sharpening B-factor of -119.6 Å^2 yielded the final model with a twist of 0.58° and 4.8 Å helical rise which are in good agreement with measurements of the cross-over distances, layer-line profiles of the 2D class averages and power spectra of the raw data. 3D classification and auto-refine processes used a central part of 10% of the intermediate reconstruction[43] (except the initial classification with $K = 4$ which used 30%). Resolution estimates were obtained from the FSC at 0.143 between two independently refined half-maps.

Model building and refinement. An initial model was built into a B-factor sharpened map (phenix.auto_sharpen)[44] by the ARP/wARP EM module[45] followed by manually rebuilding in Coot[46]. The resulting model was refined by real space refinement using phenix.real_space_refine[47] with NCS and secondary structure restraints.

Sequence analysis. V-germline, J-germline, and C-germline segments and CDRs were identified by http://www.vbase2.org/ database search[48], BLAT search on UCSC (http://genome-euro.ucsc.edu/)[49], and BLAST/BLAT search on ENSEMBL (http://www.ensembl.org/Multi/Tools/Blast?db = core)[50] of the disposed fibril protein and its respective cDNA sequence. From these databases, cDNA and peptide sequences from the best candidates for each segment (fit > 80%) were retrieved and analyzed segment-wise for their fit to the disposed fibril protein using "MEGA Molecular Evolutionary Genetics Analysis" software and the multiple sequencing alignment tool "MUSCLE"[51]. Genetic distances were calculated by Maximum Composite Likelihood to identify the most probable V-segment, J-segment, and C-segment family which were then simultaneously aligned to the fibril protein and its respective cDNA sequence in order to gain a full length picture of sequence variation by MEGA and Clustal Omega (https://www.ebi.ac.uk/Tools/msa/clustalo/)[52]. The hydropathy score for each amino acid from residue Gly15 to Thr105 was assigned according to the Kyte–Doolittle scale of hydropathy[53]. The amyloid score for each residue was calculated based on the prediction of amyloid-prone regions using the programs WALTZ[54], TANGO[55], AmylPred[56], Foldamyloid[57], and Aggrescan[58]. An amyloid score of 0 means that none of the five programs identifies this residue as amyloidogenic. An amyloid score of 5 means that all five programs suggest this residue to be aggregation prone (Supplementary Table 3). WALTZ: values above 0.00 are considered as hits. TANGO: Beta sheet aggregation values above 0.00 are considered as hits. Fold amyloid: Amino acid residues having values above 21.4 for five consecutive residues are considered as hits. Aggrescan: Amino acid residues having value greater than −0.02 are considered as hot spots. AmylPred: Sequence regions predicted as hits by the Consensus method.

Protein structure representation. Representations of reconstructed densities and refined models were created with UCSF Chimera[59]. A native LC structure was reproduced from protein data base (PDB) entry 1BJM[60] based on its sequential similarity to our fibril protein and the presence of an *IGLV1-44* germ line segment.

Reporting summary. Further information on experimental design is available in the Nature Research Reporting Summary linked to this article.

Data availability

The reconstructed cryo-EM map was deposited in the Electron Microscopy Data Bank with the accession code EMD-4452. The coordinates of the fitted atomic model were deposited in the PDB under the accession code 6IC3. The Cryo-EM data were deposited on EMPIAR with the accession code EMPIAR-10245. The datasets and materials used during the current study are available from the corresponding author on reasonable request. The data underlying the Supplementary Figures 1 and 2 are provided as a Source Data File.

Received: 6 December 2018 Accepted: 15 February 2019
Published online: 20 March 2019

References

1. Ramirez-Alvarado, M. et al. Systemic misfolding of immunoglobulins in the test tube and in the cell. *FASEB J.* **32**, abstr. 247.3 (2018).
2. van der Kant, R. et al. Prediction and reduction of the aggregation of monoclonal antibodies. *J. Mol. Biol.* **429**, 1244–1261 (2017).
3. Gertz, M. A. et al. Immunoglobulin light chain amyloidosis: 2016 update on diagnosis, prognosis, and treatment. *Am. J. Hematol.* **91**, 947–956 (2016).
4. Quock, T. P., Yan, T., Chang, E., Guthrie, S. & Broder, M. S. Epidemiology of AL amyloidosis: a real-world study using US claims data. *Blood Adv.* **2**, 1046–1053 (2018).
5. Buxbaum, J. N., Chuba, J. V., Hellman, G. C., Solomon, A. & Gallo, G. R. Monoclonal immunoglobulin deposition disease: light chain and light and heavy chain deposition diseases and their relation to light chain amyloidosis. Clinical features, immunopathology, and molecular analysis. *Ann. Intern. Med.* **112**, 455–464 (1990).
6. Nienhuis, H. L. A., Bijzet, J. & Hazenberg, B. P. C. The prevalence and management of systemic amyloidosis in western countries. *Kidney Dis.* **2**, 10–19 (2016).
7. Perfetti, V. et al. The repertoire of λ light chains causing predominant amyloid heart involvement and identification of a preferentially involved germline gene, IGLV1-44. *Blood* **119**, 144–150 (2012).
8. Wechalekar, A. D. et al. A European collaborative study of treatment outcomes in 346 patients with cardiac stage III AL amyloidosis. *Blood* **121**, 3420–3427 (2013).
9. Merlini, G., Comenzo, R. L., Seldin, D. C., Wechalekar, A. & Gertz, M. A. Immunoglobulin light chain amyloidosis. *Expert Rev. Gastroent.* **7**, 143–156 (2014).
10. Schönland, S. O. et al. Immunohistochemistry in the classification of systemic forms of amyloidosis: a systematic investigation of 117 patients. *Blood* **119**, 488–493 (2012).
11. Merlini, G. & Bellotti, V. Molecular mechanisms of amyloidosis. *N. Engl. J. Med.* **349**, 583–596 (2003).
12. Hurle, M. R., Helms, L. R., Li, L., Chan, W. & Wetzel, R. A role for destabilizing amino acid replacements in light-chain amyloidosis. *Proc. Natl Acad. Sci. USA* **91**, 5446–5450 (1994).
13. Blancas-Mejía, L. M. & Ramirez-Alvarado, M. Systemic amyloidoses. *Annu. Rev. Biochem.* **82**, 745–774 (2013).
14. McWilliams-Koeppen, H. P. et al. Light chain amyloid fibrils cause metabolic dysfunction in human cardiomyocytes. *PLoS ONE* **9**, e0137716 (2015).
15. Nokwe, C. N. et al. A Stable mutant predisposes anti-body domains to amyloid formation through specific non-native interactions. *J. Mol. Biol.* **428**, 1315–1332 (2016).
16. Comenzo, R. L., Zhang, Y., Martinez, C., Osman, K. & Herrera, G. A. The tropism of organ involvement in primary systemic amyloidosis: contributions of Ig VL germ line gene use and clonal plasma cell burden. *Blood* **98**, 714–720 (2001).
17. Abraham, R. S. et al. Immunoglobulin light chain variable (V) region genes influence clinical presentation and outcome in light chain-associated amyloidosis (AL). *Blood* **101**, 3801–3808 (2003).
18. Kourelis, T. V. et al. Clarifying immunoglobulin gene usage in systemic and localized immunoglobulin light-chain amyloidosis by mass spectrometry. *Blood* **129**, 299–306 (2017).
19. Pepys, M. B. Amyloidosis. *Annu. Rev. Med.* **57**, 223–241 (2006).
20. Chiti, F. & Dobson, C. M. Protein misfolding, amyloid formation, and human disease: a summary of progress over the last decade. *Annu. Rev. Biochem.* **86**, 27–68 (2017).
21. Sunde, M. et al. Common core structure of amyloid fibrils by synchrotron X-ray diffraction. *J. Mol. Biol.* **273**, 729–739 (1997).

22. Annamalai, K. et al. Polymorphism of amyloid fibrils in vivo. *Angew. Chem. Int. Ed.* **55**, 4822–4825 (2016).
23. Annamalai, K. et al. Common fibril structures imply systemically conserved protein misfolding pathways in vivo. *Angew. Chem. Int. Ed.* **56**, 7510–7514 (2017).
24. Fitzpatrick, A. W. P. et al. Cryo-EM structures of tau filaments from Alzheimer's disease. *Nature* **547**, 185–190 (2017).
25. Falcon, B. et al. Structures of filaments from Pick's disease reveal a novel tau protein fold. *Nature* **561**, 137–140 (2018).
26. Gremer, L. et al. Fibril structure of amyloid-β(1–42) by cryo-electron microscopy. *Science* **358**, 116–119 (2017).
27. Guerrero-Ferreira, R. et al. Cryo-EM structure of alpha-synuclein fibrils. *eLife* **7**, e36402 (2018).
28. Liberta, F. et al. Cryo-EM structure of an amyloid fibril from systemic amyloidosis. Preprint at *bioRxiv* https://doi.org/10.1101/357129 (2018).
29. Swuec, P. et al. Cryo-EM structure of cardiac amyloid fibrils from an immunoglobulin light chain (AL) amyloidosis patient. Preprint at *bioRxiv* https://doi.org/10.1101/444901 (2018).
30. Schmidt, A., Annamalai, K., Schmidt, M., Grigorieff, N. & Fändrich, M. Cryo-EM reveals the steric zipper structure of a light chain-derived amyloid fibril. *Proc. Natl Acad. Sci. USA* **113**, 6200–6205 (2016).
31. Blancas-Mejia, L. M. et al. Immunoglobulin light chain amyloid aggregation. *Chem. Commun.* **54**, 10664–10674 (2018).
32. del Pozo-Yauner, L. et al. The N-terminal strand modulates immunoglobulin light chain fibrillogenesis. *Biochem. Biophys. Res. Commun.* **443**, 495–499 (2014).
33. Piehl, W. et al. Immunoglobulin light chains form an extensive and highly ordered fibril involving the N- and C-termini. *ACS Omega* **2**, 712–720 (2017).
34. Fersht, A. *Structure and Mechanism in Protein Science* (W.H. Freeman and Company, New York, 1999).
35. Choi, B., Kim, T., Lee, S. W. & Eom, K. Nanomechanical characterization of amyloid fibrils using single-molecule experiments and computational simulations. *J. Nanomater.* **2016**, 5873695 (2016).
36. White, H. E. et al. Globular tetramers of β2-microglobulin assemble into elaborate amyloid fibrils. *J. Mol. Biol.* **389**, 48–57 (2009).
37. Brumshtein, B. et al. Formation of amyloid fibers by monomeric light chain variable domains. *J. Biol. Chem.* **289**, 27513–27525 (2014).
38. Brumshtein, B. et al. Identification of two principal amyloid-driving segments in variable domains of Ig light chains in systemic light chain amyloidosis. *J. Biol. Chem.* **293**, 19659–19671 (2018).
39. Hora, M. et al. MAK33 antibody light chain amyloid fibrils are similar to oligomeric precursors *PLoS ONE* **7**, e0181799 (2017).
40. Kremer, J. R., Mastronarde, D. N. & McIntosh, J. R. Computer visualization of three-dimensional image data using IMOD. *J. Struct. Biol.* **116**, 71–76 (1996).
41. Zheng, S. Q. et al. MotionCor2: anisotropic correction of beam-induced motion for improved cryo-electron microscopy. *Nat. Methods* **14**, 331–332 (2017).
42. Zhang, K. Gctf: Real-time CTF determination and correction. *J. Struct. Biol.* **193**, 1–12 (2016).
43. He, S. & Scheres, S. H. W. Helical reconstruction in RELION. *J. Struct. Biol.* **198**, 163–176 (2017).
44. Afonine, P. V. et al. New tools for the analysis and validation of cryo-EM maps and atomic models. *Acta Crystallogr. D* **74**, 814–840 (2018).
45. Langer, G., Cohen, S. X., Lamzin, V. S. & Perrakis, A. Automated macromolecular model building for X-ray crystallography using ARP/wARP version 7. *Nat. Protoc.* **3**, 1171–1179 (2008).
46. Emsley, P., Lohkamp, B., Scott, W. G. & Cowtan, K. Features and development of coot. *Acta Crystallogr. D* **66**, 486–501 (2010).
47. Afonine, P. V. et al. Real-space refinement in PHENIX for cryo-EM and crystallography. *Acta Crystallogr. D* **74**, 531–544 (2018).
48. Retter, I., Althaus, H. H., Munch, R. & Muller, W. VBASE2, an integrative V gene database. *Nucleic Acids Res.* **33**, D671–D674 (2005).
49. Kent, W. J. BLAT–the BLAST-like alignment tool. *Genome Res.* **12**, 656–664 (2002).
50. Altschul, S. F., Gish, W., Miller, W., Myers, E. W. & Lipman, D. J. Basic local alignment search tool. *J. Mol. Biol.* **215**, 403–410 (1990).
51. Tamura, K., Stecher, G., Peterson, D., Filipski, A. & Kumar, S. MEGA6: Molecular Evolutionary Genetics Analysis version 6.0. *Mol. Biol. Evol.* **30**, 2725–2729 (2013).
52. Sievers, F. et al. Fast, scalable generation of high-quality protein multiple sequence alignments using Clustal Omega. *Mol. Syst. Biol.* **7**, 539 (2011).
53. Kyte, J. & Doolittle, R. F. A simple method for displaying the hydropathic character of a protein. *J. Mol. Biol.* **157**, 105–132 (1982).
54. Maurer-Stroh, S. et al. Exploring the sequence determinants of amyloid structure using position-specific scoring matrices. *Nat. Methods* **7**, 237–242 (2010).
55. Fernandez-Escamilla, A. M., Rousseau, F., Schymkowitz, J. & Serrano, L. Prediction of sequence-dependent and mutational effects on the aggregation of peptides and proteins. *Nat. Biotechnol.* **22**, 1302–1306 (2004).
56. Frousios, K. K., Iconomidou, V. A., Karletidi, C. M. & Hamodrakas, S. J. Amyloidogenic determinants are usually not buried. *BMC Struct. Biol.* **9**, 44 (2009).
57. Garbuzynskiy, S. O., Lobanov, M. Y. & Galzitskaya, O. V. FoldAmyloid: a method of prediction of amyloidogenic regions from protein sequence. *Bioinformatics* **26**, 326–332 (2010).
58. Conchillo-Solé, O. et al. AGGRESCAN: a server for the prediction and evaluation of "hot spots" of aggregation in polypeptides. *BMC Bioinforma.* **8**, 65 (2007).
59. Pettersen, E. F. et al. UCSF Chimera—a visualization system for exploratory research and analysis. *J. Comput. Chem.* **25**, 1605–1612 (2004).
60. Huang, D. B., Ainsworth, C. F., Stevens, F. J. & Schiffer, M. Three quaternary structures for a single protein. *Proc. Natl Acad. Sci. USA* **93**, 7017–7021 (1996).

Acknowledgements

M.S. is supported by the Deutsche Forschungsgemeinschaft (grants Sonderforschungsbereich 1279/A03 to M.F. and SCHM 3276/1 to M.S.). All cryo-EM data were collected at the European Molecular Biology Laboratory, Heidelberg (Germany), funded by iNEXT (Horizon 2020, European Union).

Author contributions

L.R., Y.-H.L., K.A., S.H., G.F. and M.S. performed research. L.R., Y.-H.L., K.A., S.H., G.F., M.S. and M.F. analyzed data. U.H. and S.O.S. contributed tools and reagents. M.F. designed research. L.R., Y.-H.L., M.S. and M.F. wrote the paper.

Additional information

Supplementary Information accompanies this paper at https://doi.org/10.1038/s41467-019-09032-0.

Competing interests: The authors declare no competing interests.

Reprints and permission information is available online at http://npg.nature.com/reprintsandpermissions/

Journal peer review information: *Nature Communications* thanks D. Alejandro Fernández-Velasco, Henning Stahlberg and the other anonymous reviewer(s) for their contribution to the peer review of this work.

Publisher's note: Springer Nature remains neutral with regard to jurisdictional claims in published maps and institutional affiliations.

Open Access This article is licensed under a Creative Commons Attribution 4.0 International License, which permits use, sharing, adaptation, distribution and reproduction in any medium or format, as long as you give appropriate credit to the original author(s) and the source, provide a link to the Creative Commons license, and indicate if changes were made. The images or other third party material in this article are included in the article's Creative Commons license, unless indicated otherwise in a credit line to the material. If material is not included in the article's Creative Commons license and your intended use is not permitted by statutory regulation or exceeds the permitted use, you will need to obtain permission directly from the copyright holder. To view a copy of this license, visit http://creativecommons.org/licenses/by/4.0/.

© The Author(s) 2019

Supplementary Figure 1

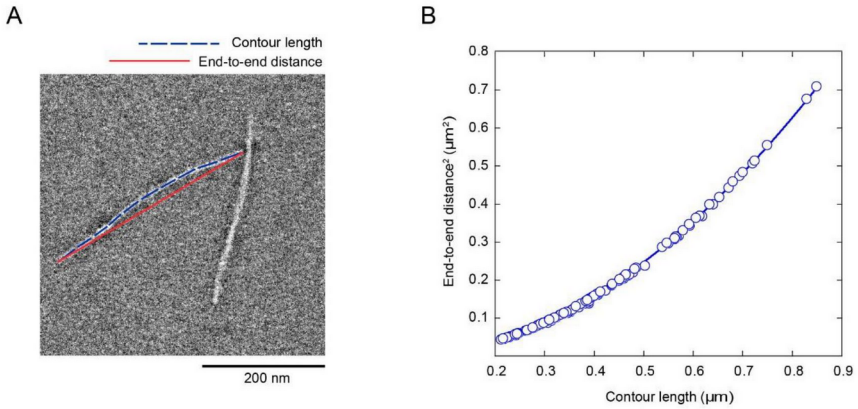

Quantification of the fibril bending rigidity

(a) Representative negatively stained TEM image of the analyzed fibrils showing the contour length and the end-to-end distance. (b) Plot of the squared end-to-end distance versus the contour length for 124 fibrils, fitted with a formula as described in the methods to obtain the fibril persistence length. The fit produced a value of 6.7 ± 0.5 µm for the persistence length and of 2.78 ± 0.21 10^{-26} Nm^2 for the bending rigidity (R^2 = 0.9995, errors refer to standard deviation).

Supplementary Figure 2

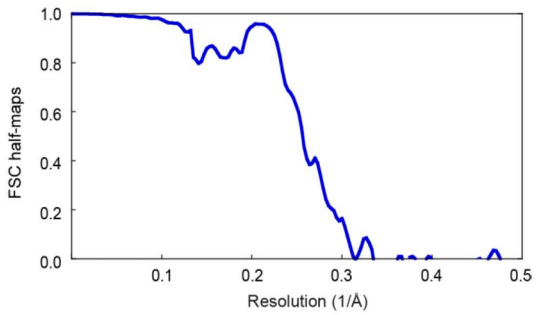

FSC curve of the reconstructed density

Supplementary Figure 3

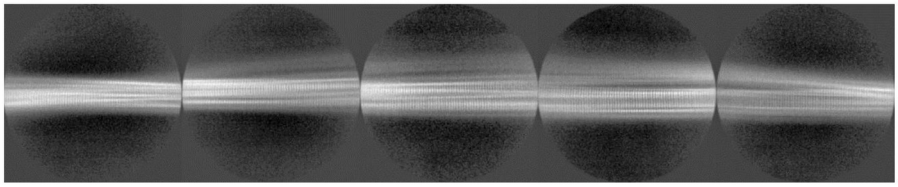

2D class averages

Selection of 2D class averages showing five classes which roughly cover one cross-over distance.

Supplementary Figure 4

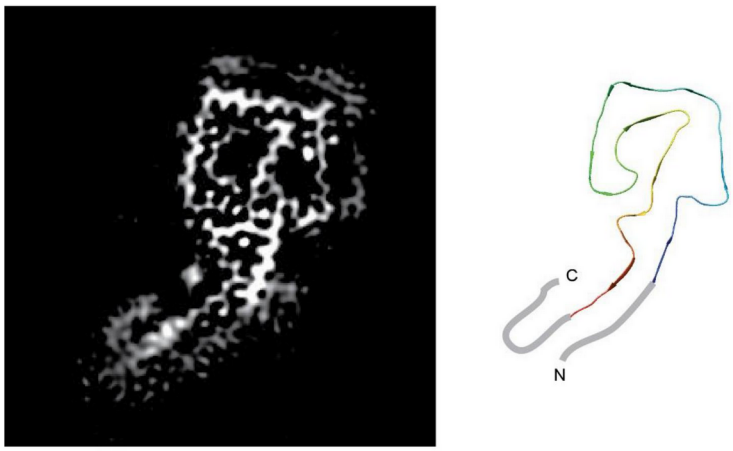

Presence of ordered and disordered regions in the fibril structure

Left: A 29 Å thick cross-sectional slice of the unmasked 3D map of the AL fibril. Right: Ribbon diagrams of one fibril molecule with a schematic drawing of the disordered C-terminus (grey). The drawing of the C-terminus corresponds to some of the diffuse density in the 3D map. Additional diffuse density of uncertain origin can be seen, similar to other *ex vivo* fibrils[1,2,3].

Supplementary Figure 5

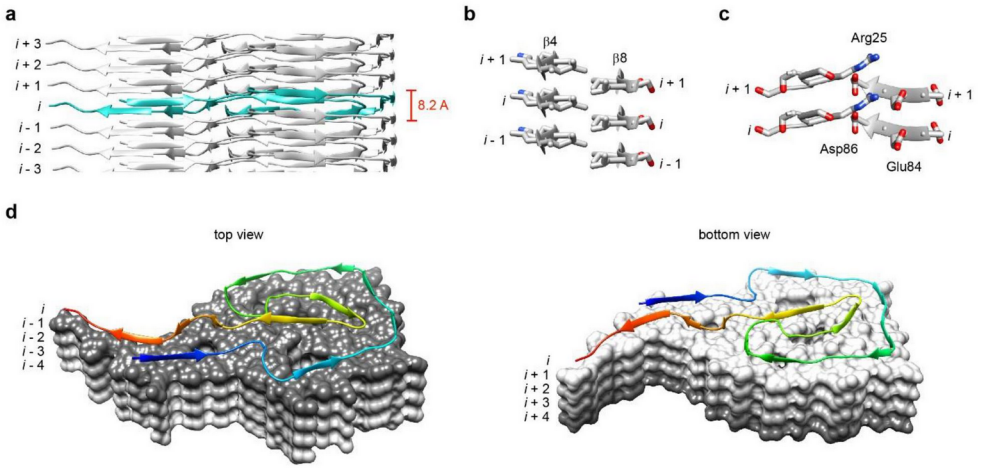

Intermolecular interactions along the fibril axis

(a) The height change of the fibril protein (8.2 Å) was determined between the Cα atom of Asn28 (highest point) and the Cα of Ala72 (lowest point). (b) Staggering of sheet β4 relative to sheet β8. Sheet β4 from layer *i* interacts with sheets β8 in layers in layers *i* and *i* + 1. (c) Interaction of Arg 25 from layer *i* with Glu84 and Asp86 in layer *i* + 1. (d) Different structural topology of the two fibril tips (left/right). Four layers are shown in gray scale (spacefill). The terminal layer is shown as a ribbon diagram in rainbow color from N (blue) to C (red).

Supplementary Table 1

Patient characteristics

Parameter	At AL diagnosis	At heart transplantation
Karnofsky Index / New York Heart Association cardiac stage	80% / III	70% / III-IV
Difference free LC value	137 mg/l	40 mg/l
Concentration of λ-LC in the urine	36 mg/d	Not determined
N-terminal pro brain natriuretic peptide concentration in the plasma	8,300 ng/l	19,800 ng/l
High sensitive troponin T concentration in the plasma	53 pg/ml	136 pg/ml
Cardiac stage	III A	III B
Septum thickness	18 mm	19 mm
Estimated glomerular filtration rate	94 ml/min	56 ml/min

Supplementary Table 2

Modeling parameters

Model resolution (Å)	
FSC threshold 0.143	3.3
FSC threshold 0.5	3.9
Model resolution range (Å)	330-3.3
Map sharpening *B* factor (Å^2)	-119.6
Model composition	
Non-hydrogen atoms	5472
Protein residues	728
Ligands	-
B factors (Å^2)	
Protein	111.43
Ligand	-
R.m.s. deviations	
Bond lengths (Å)	0.010
Bond angles (°)	1.257
Validation	
MolProbity score	2.29
Clashscore	9.22
Poor rotamers (%)	1.4
Ramachandran plot	
Favored (%)	83.1
Allowed (%)	16.9
Disallowed (%)	0

Supplementary Table 3

Analysis of the aggregation score for residues Val3-Ser118. Please refer to the Methods section for details. Hits are presented in bold print, and for AmylPred as +

Sequence	WALTZ	TANGO	Fold amyloid	Aggrescan	AmylPred	Score
V	0.00	0.00	23.00	-0.10	–	0
L	0.00	0.00	22.10	-0.10	–	0
T	0.00	0.00	21.20	-0.10	–	0
Q	0.00	0.00	19.90	0.09	–	0
P	0.00	0.00	18.40	-0.14	–	0
P	0.00	0.00	18.40	-0.38	–	0
S	0.00	0.00	18.20	-0.44	–	0
A	0.00	0.00	18.20	-0.28	–	0
S	0.00	0.00	18.60	-0.28	–	0
G	0.00	0.00	18.50	-0.31	–	0
T	0.00	0.00	17.90	-0.45	–	0
P	0.00	0.00	18.10	-0.62	–	0
G	0.00	0.00	18.90	-0.35	–	0
Q	**87.96**	0.00	19.70	-0.30	–	1
R	**87.96**	0.00	20.20	**-0.01**	–	2
V	**87.96**	0.00	21.90	**-0.01**	–	2
T	**87.96**	0.00	21.70	**0.16**	–	2
I	**87.96**	0.00	22.20	**0.29**	–	2
S	**87.96**	0.00	21.10	**0.39**	–	2
C	0.00	0.00	20.50	**-0.01**	–	1
S	0.00	0.00	19.60	-0.03	–	0
G	0.00	0.00	19.60	-0.34	–	0
R	**80.60**	0.00	18.50	-0.48	–	1
S	**80.60**	0.00	18.60	-0.31	–	1
S	**80.60**	0.00	20.30	-0.34	–	1
N	**80.60**	0.00	19.50	-0.44	–	1
I	**80.60**	0.00	20.10	-0.45	–	1
G	**80.60**	0.00	20.20	-0.21	–	1
R	**80.60**	0.00	21.50	**0.06**	–	2
N	**91.97**	0.00	21.20	**0.11**	–	2
L	**91.97**	0.00	21.30	**0.00**	–	2
V	**91.97**	0.00	**22.80**	**0.24**	–	3
K	**91.97**	0.00	**24.30**	**0.24**	–	3
W	**79.93**	0.00	**23.00**	**0.25**	–	3
Y	**79.93**	0.00	**22.10**	**0.31**	–	3

Q	**79.93**	0.00	**24.00**	**0.03**	–	3
Q	**79.93**	0.00	**21.80**	**0.09**	–	3
F	**79.93**	0.00	20.00	-0.08	–	1
P	**79.93**	0.00	20.20	-0.25	–	1
G	0.00	0.00	20.30	-0.13	–	0
T	0.00	0.00	18.30	-0.08	–	0
A	0.00	0.00	18.40	-0.14	–	0
P	**79.93**	0.00	20.00	**0.11**	–	2
K	**97.99**	0.00	21.10	**0.45**	–	2
L	**87.29**	**27.12**	22.30	**0.63**	+	4
L	**87.29**	**27.30**	24.00	**0.60**	+	4
I	**87.29**	**27.30**	24.10	**0.46**	+	4
Y	**87.29**	**27.30**	22.70	**0.33**	+	4
S	**87.29**	**27.30**	21.10	-0.04	+	3
N	**87.29**	**12.36**	19.90	-0.42	–	2
D	0.00	0.00	18.90	-0.73	–	0
Q	0.00	0.00	18.70	-0.93	–	0
R	0.00	0.00	18.70	-0.97	–	0
P	0.00	0.00	18.60	-0.55	–	0
S	0.00	0.00	19.50	-0.34	–	0
G	0.00	0.00	18.80	-0.43	–	0
V	0.00	0.00	18.80	-0.43	–	0
P	0.00	0.00	19.40	-0.13	–	0
D	0.00	0.00	21.40	-0.13	–	0
R	0.00	0.00	20.20	-0.13	–	0
F	0.00	0.00	20.20	-0.40	–	0
S	0.00	0.00	20.30	-0.48	–	0
G	0.00	0.00	19.70	-0.26	–	0
S	0.00	0.00	17.90	-0.16	–	0
K	0.00	0.00	17.70	-0.44	–	0
S	0.00	0.00	18.20	-0.44	–	0
G	0.00	0.00	18.20	-0.36	–	0
T	0.00	0.00	18.60	-0.36	–	0
S	0.00	0.00	18.60	-0.03	–	0
A	0.00	**0.40**	20.30	**0.00**	–	2
S	0.00	**0.40**	20.30	**0.31**	–	2
L	0.00	**0.64**	21.50	**0.29**	–	2
A	0.00	**0.64**	21.10	**0.25**	–	2
V	0.00	**0.64**	20.90	**0.46**	–	2
S	0.00	**0.24**	20.90	**0.32**	–	2
G	0.00	**0.24**	20.80	**0.08**	–	2

L	0.00	**0.24**	19.60	-0.11	–	1
Q	0.00	0.00	19.50	-0.60	–	0
S	0.00	0.00	19.50	-0.76	–	0
E	0.00	0.00	18.00	-0.69	–	0
D	0.00	0.00	18.10	-1.15	–	0
E	0.00	0.00	17.90	-0.81	–	0
A	**79.93**	0.00	19.60	-0.60	–	1
D	**79.93**	0.00	21.30	-0.31	+	2
Y	**79.93**	**0.39**	**22.50**	-0.06	+	4
Y	**80.60**	**0.39**	**22.50**	0.14	+	4
C	**80.60**	**0.39**	**23.00**	0.29	+	4
A	**80.60**	**0.39**	**23.50**	0.29	+	4
A	**80.60**	**0.39**	**21.80**	0.12	+	4
W	**79.93**	**0.39**	21.10	-0.07	–	2
D	**79.93**	0.00	21.10	**0.05**	–	2
A	**79.93**	**12.73**	22.20	-0.14	–	2
T	**88.63**	**28.85**	20.20	-0.14	–	2
L	**88.63**	**11.30**	20.70	-0.14	+	3
N	**93.98**	**12.67**	**22.40**	**0.35**	+	5
A	**93.98**	**15.72**	**23.20**	**0.61**	+	5
W	**93.98**	**16.02**	**23.60**	**0.56**	+	5
V	**93.98**	**16.02**	**23.30**	**0.28**	+	5
F	**93.98**	**15.35**	**22.80**	**0.39**	+	5
G	**93.98**	**43.39**	20.50	**0.37**	–	3
G	**93.98**	**0.55**	19.70	**0.09**	–	3
G	0.00	0.00	17.80	**0.06**	–	1
T	0.00	0.00	19.40	-0.21	–	0
K	0.00	0.00	20.00	**0.09**	–	1
L	**82.61**	**0.63**	21.30	**0.37**	–	3
T	**82.61**	**0.63**	22.40	**0.40**	–	3
V	**82.61**	**0.63**	22.50	**0.25**	–	3
L	**82.61**	**0.63**	21.30	**0.33**	–	3
S	**82.61**	**0.63**	20.80	**0.00**	–	3
Q	**82.61**	0.00	19.60	**0.02**	–	3
P	0.00	0.00	18.50	-0.21	–	0
K	0.00	0.00	18.80	-0.46	–	0
A	0.00	0.00	18.50	-0.46	–	0
A	0.00	0.00	18.60	-0.44	–	0
P	0.00	0.00	18.90	-0.44	–	0
S	0.00	0.00	18.50	-0.44	–	0

Supplementary References

[1] Fitzpatrick, A.W.P. *et al.* Cryo-EM structures of tau filaments from Alzheimer's disease. *Nature* **547**, 185-190 (2017)

[2] Liberta, F. *et al.* Cryo-EM structure of an amyloid fibril from systemic amyloidosis. Preprint at https://www.biorxiv.org/content/early/2018/06/29/357129 (2018)

[3] Swuec, P. *et al.* Cryo-EM structure of cardiac amyloid fibrils from an immunoglobulin light chain (AL) amyloidosis patient. Preprint at https://www.biorxiv.org/content/early/2018/10/17/444901 (2018)

Publication II:

"Cryo-EM reveals structural breaks in a patient-derived amyloid fibril from systemic AL amyloidosis." Radamaker, L., Baur, J., Huhn, S., Haupt, C., Hegenbart, U., Schönland, S.O., Bansal, A., Schmidt, M. and Fändrich, M. *Nature Communications* **12,** 875 (2021)

DOI: 10.1038/s41467-021-21126-2

Licensed under a Creative Commons Attribution 4.0 International License (CC BY 4.0), https://creativecommons.org/li

Contribution to publication II:

- Performed the research and analyzed the data presented in Fig. 1,2,4,5; SI Fig. 1-6, 9-10. Also SI Table 1 in co-operation with Matthias Schmidt.
- Writing and revising the manuscript in co-operation with Marcus Fändrich with contributions from Julian Baur, Akanksha Bansal and Stephanie Huhn.

Summary

In this publication, two fibril structures from the FOR005 patient case are presented. The fibril protein consists of a 115-residue LC fragment that stems from the GL segments *IGLV3-19, IGLJ2*01* and *IGLC2* and deviates by seven mutations, including one in the *J* and one in the *C* segment. Although a single fibril morphology was reconstructed, two fibril cross-sections were obtained that differ in a 12-residue segment. It was demonstrated that these two conformations co-exist within a single fibril, forming structural breaks at their interface. Thus, amyloid fibrils may not always be conformationally homogeneous along the fibril axis, as previously assumed. Comparison to an ssNMR structure from fibrils formed in vitro from a 97-residue fragment of the patient FOR005 LC sequence showed that the structure of the ex vivo fibrils was not replicated in the in vitro sample, even when the in vitro fibrils were formed in the presence of ex vivo fibril seeds.

nature COMMUNICATIONS

ARTICLE

https://doi.org/10.1038/s41467-021-21126-2 OPEN

Cryo-EM reveals structural breaks in a patient-derived amyloid fibril from systemic AL amyloidosis

Lynn Radamaker[1], Julian Baur[1], Stefanie Huhn[2], Christian Haupt[1], Ute Hegenbart[3], Stefan Schönland[3], Akanksha Bansal[1], Matthias Schmidt[1] & Marcus Fändrich[1✉]

Systemic AL amyloidosis is a debilitating and potentially fatal disease that arises from the misfolding and fibrillation of immunoglobulin light chains (LCs). The disease is patient-specific with essentially each patient possessing a unique LC sequence. In this study, we present two ex vivo fibril structures of a λ3 LC. The fibrils were extracted from the explanted heart of a patient (FOR005) and consist of 115-residue fibril proteins, mainly from the LC variable domain. The fibril structures imply that a 180° rotation around the disulfide bond and a major unfolding step are necessary for fibrils to form. The two fibril structures show highly similar fibril protein folds, differing in only a 12-residue segment. Remarkably, the two structures do not represent separate fibril morphologies, as they can co-exist at different z-axial positions within the same fibril. Our data imply the presence of structural breaks at the interface of the two structural forms.

[1] Institute of Protein Biochemistry, Ulm University, Ulm, Germany. [2] Medical Department V, Section of Multiple Myeloma, Heidelberg University Hospital, Heidelberg, Germany. [3] Medical Department V, Amyloidosis Center, Heidelberg University Hospital, Heidelberg, Germany. ✉email: marcus.faendrich@uni-ulm.de

Systemic AL amyloidosis is a protein misfolding disease that is newly diagnosed in 4–15 persons per one million per year in the United States of America[1] and other parts of the world[2,3]. The amyloid deposits underlying this disease frequently occur in heart and kidneys, with cardiac involvement being the most important prognostic factor for the patient survival[4]. The LC amino acid sequence is highly variable, as a consequence of the recombination of different variable (V), joining (J), and constant (C) germ line (GL) segments, as well as somatic hypermutation[5]. Out of the resulting LC variants, the subtypes λ1, λ2, λ3, λ6, and κ1 are in particular associated with AL amyloidosis[6,7].

It is well established that amyloid fibrils and other LC aggregates play a defining role in the pathogenicity of this disease[4,5]. However, except for the chemotherapeutic removal of the pathogenic plasma cell clone, no pharmacological treatment options exist which directly prevent fibril formation or reverse fibril-induced organ damage[8]. One reason for this paucity of treatment options is the lack of knowledge about the mechanism of LC misfolding and the structure of pathogenic amyloid fibrils in vivo. Another reason is the patient-specific nature of systemic AL amyloidosis, with each patient presenting an essentially unique LC precursor and fibril protein[9].

To provide insight into the fibril structure and LC misfolding mechanism in vivo, we recently set up a research strategy in which AL amyloid fibrils were extracted from diseased tissue and subjected to biochemical analysis[10,11]. The fibril proteins are mainly derived from the LC variable (V_L) domain of the fibril protein precursor[10,11], consistent with earlier observations[12]. They contain the intramolecular disulfide bond that is also present within the natively folded V_L domain[10,13]. The fibrils are polymorphic[11], but consistent amyloid fibril morphologies are found in different organs/deposition sites within the same patient[10]. Different AL patients present different fibril morphologies[10,11], suggesting that the variability of the LC sequence leads to different, or even patient-specific fibril structures.

To obtain insight into their molecular conformations, we and others recently started to employ cryo-electron microscopy (cryo-EM) combined with three-dimensional (3D) reconstruction. So far, two AL amyloid fibrils were analyzed with this combination of methods, one derived from a λ1 (ref. [13]), termed hereafter FOR006, and one from a λ6 LC[14]. The two fibril proteins showed markedly different folds, and their conformations differed fundamentally from natively folded LCs. In the present study, we analyze the structure of fibrils that were purified from the heart muscle tissue of a patient (FOR005) with λ3 LC-derived amyloid fibrils. Using cryo-EM, we obtained two different fibril structures, termed here A and B. The two structures coexist at different *z*-axial positions within the same fibril, which implies the presence of structural breaks in these patient-derived amyloid fibrils.

Results

Extraction of the fibril protein and sequence analysis. The analyzed AL amyloid fibrils were extracted from the explanted heart of a female patient (FOR005) with systemic AL amyloidosis. The patient suffered from severe cardiomyopathy and underwent heart transplantation at the age of 50 years. We previously obtained the amino acid sequence of the fibril protein by protein sequencing, and the nucleotide sequence of the precursor LC by cDNA sequencing[10]. The tissue-deposited fibril protein consists of residues Ser2–Ser116 of the λ3 precursor LC, which correspond to the V_L domain and a few residues (Gly109–Ser116) of the LC constant (C_L) domain. Bioinformatic analysis of the LC cDNA sequence indicated that it originates from the GL segments *IGLV3-19*01*, *IGLJ2*01*, and *IGLC2*, which agrees with previous data showing that the *IGLV3-19* GL segment is linked to heart involvement[6,7]. The amino acid sequence of the fibril protein differs from the protein sequence of the translated GL segments in several positions, probably as a result of the B-cell clone-specific somatic hypermutation. The fibril protein sequence contains five mutations with respect to the GL protein sequence within the *IGLV3-19* segment (Tyr31Ser, Tyr48Phe, Gly49Arg, Asn51Ser, and Gly94Ala), one within *IGLJ2*01* (Val97Gln), and one within *IGLC2* (Val135Gly). C_L mutations are rarely reported for patients with AL amyloidosis, possibly because the cDNA-based gene sequencing of the fibril protein precursor is often confined to the V_L domain.

Observation of two fibril structures in the fibril extracts. The extracted fibrils were subjected to cryo-EM and imaged at 300 kV (Supplementary Fig. 1a). Visual inspection of the recorded images revealed, despite evidence for polymorphism[10], one apparently dominant fibril morphology that corresponded to >95% of fibrils visible in the fibril extracts. Picking this fibril morphology for 3D reconstruction and performing two-dimensional (2D) and 3D classification resulted in two 3D classes showing two different fibril structures, termed here A and B (Fig. 1 and Supplementary Fig. 1b). The corresponding reconstructions were refined to spatial resolutions of 3.2 Å for fibril structure A and 3.4 Å for B (Supplementary Table 1), based on the 0.143 Fourier shell correlation (FSC) criterion (Supplementary Fig. 2a). Their local resolution varied in the fibril cross sections, with higher resolution occurring at the fibril center and lower resolution toward the edges (Supplementary Fig. 2b). Additional rounds of 3D classification did not further subdivide the data sets in a meaningful fashion.

After the initial 3D classification, the data set contained 64,652 segments classified as fibril structure A and 36,667 as fibril structure B. The final reconstructions contained 11,003 segments for fibril structure A and 12,122 for fibril structure B (Supplementary Table 1). We interpreted the two reconstructions with molecular models (Fig. 1c, d) and obtained model resolutions of 3.1 Å for reconstruction A and 3.2 Å for B (Supplementary Table 1 and Supplementary Fig. 2c). 2D projections of the models correspond well to the 2D class averages of the original segments (Supplementary Fig. 3). Both models depict polar fibrils with C1 helical symmetry (Supplementary Table 1), consisting of only one protofilament and a single stack of fibril proteins (Fig. 1b). All peptide bonds of the fibril proteins, including the two X-Pro bonds, are modeled as *trans* isomers.

Both 3D maps contain diffuse density decorating the ordered fibril core (Fig. 1c, d, blue star), reminiscent of the two previously reported cryo-EM structures of ex vivo AL amyloid fibrils[13,14]. These diffuse density regions may represent disordered parts of the fibril protein or non-fibril components. In addition, there is a well-defined density feature (Fig. 1c, d, red star) that appears to stem from a peptide segment in β-sheet conformation, owing to the zigzag pattern and a 4.8 Å rise along the fibril axis (Supplementary Fig. 4a, b). Similar well-defined density islands were previously observed with in vitro formed fibril structures[15,16]. One study suggested that the density islands were formed from a segment of the fibril protein that was protruding from the main fibril core[15]. In another study, the density island originated from a peripherally attached fibril protein that adopted a single, short cross-β-strand but that was otherwise conformationally disordered[16]. As all segments outside the FOR005 fibril core are too short to reach our density islands (Supplementary Fig. 4c), we conclude that non-covalently attached fibril proteins, or fibril protein fragments, are the most plausible explanation of the density islands in the FOR005 fibril structure.

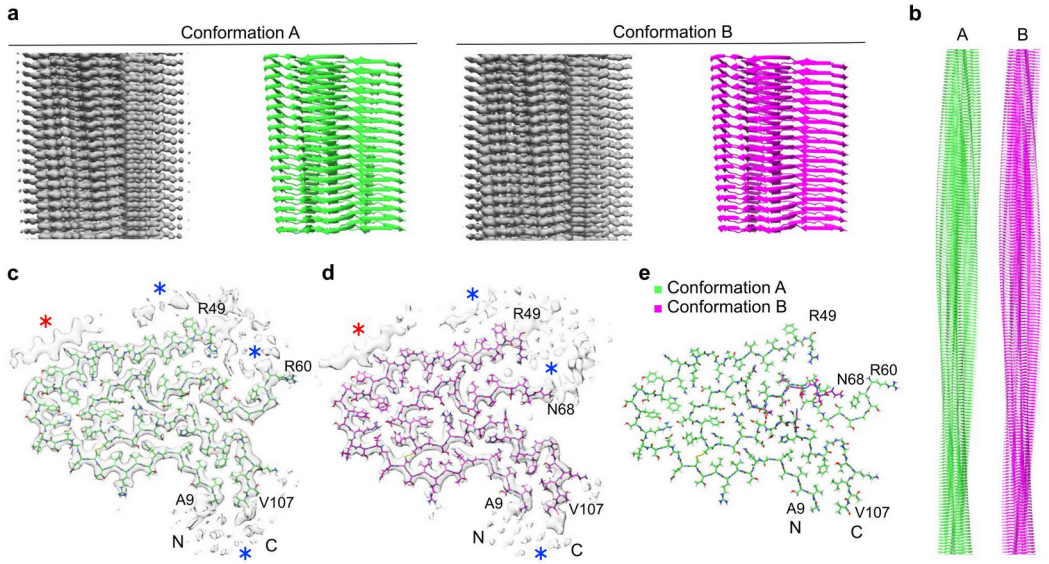

Fig. 1 Two different fibril protein conformations underlie the FOR005 amyloid fibrils. a Side views of the 3D maps of fibril structures A and B (left, gray), and corresponding molecular models (right, green/magenta). **b** Side view of longer segments of the two molecular models. **c**, **d** Cross-sectional views of the fibril protein conformations A (**c**) (EMD-11031) and B (**d**) (EMD-11030). Blue asterisk: region with blurry density surrounding the fibril core. Red asterisk: extra density decorating the fibril core, indicating an ordered peptide conformation. **e** Overlay of the molecular models of fibril structures A (PDB: 6Z10) and B (PDB: 6Z1I). The N- and C-terminal residues of the model are highlighted.

Comparison of the fibril protein conformations A and B. The two fibril structures arise from similar but slightly different protein conformations. The fibril proteins are essentially indistinguishable at residues Ala9–Arg49 and Leu72–Val107. Residues Ser2–Pro8 and Leu108–Ser116 could not be assigned to any well-defined density in the 3D map, which implies that these segments are structurally heterogeneous or disordered. The main difference between the two structures lies in the segment Arg60–Ser71 (Fig. 1e). In fibril A, residues Arg60–Ser71 are in a stable conformation encompassing an arch, while residues Lys50–Asp59 are not well defined in the 3D map (Fig. 1c). In fibril B, residues Asn68–Ser71 are in a relatively extended conformation and the region of structural disorder occurs between residues Lys50–Gly67 (Fig. 1d). Importantly, mass spectrometry previously demonstrated the fibril protein to be continuous and to extend from Ser2 to Ser116 (ref. [10]). Thus, the fibril core as seen in our 3D map is not made up of two fibril protein fragments, but instead it consists of two structurally ordered segments (Ala9–Arg49 and Arg60/Asn68–Val107) that are linked by a structurally heterogeneous region (Lys50–Asp59/Gly67).

The fibril protein shows β-strand conformation at residues Val10–Leu14, Thr17–Gln23, Asp25–Ser26, Arg28–Ser31, Trp34–Gln37, Pro43–Ile47, Leu72–Thr75, Ala79–Glu82, Tyr85–Tyr86, Asn88–Asp91, Asn95–Gln97, and Thr103–Thr106 in both fibrils (Fig. 2a). We refer to these segments as β1 to β12. Structure A contains two additional β-strands in a segment that is disordered in structure B (Arg60–Gly67). These strands are formed by residues Arg60–Ser62 and Ser64–Ser65 and are termed β6′ and β6″ because they are in between the strands β6 and β7. All strands form cross-β-sheets with parallel, hydrogen bonded strand–strand interactions (Fig. 2b and Supplementary Fig. 5a). The protein fold is compact and devoid of large internal cavities.

Molecular interactions defining the fibril structure. The fibril proteins interact along the fibril axis through backbone hydrogen bonds that extend between the strands of the cross-β-sheets. In addition, there are side chain–side chain interactions, such as polar ladders of asparagine or glutamine residues, or stacked hydrophobic or aromatic groups. These features are shown for residues Gln37 and Phe48 in the Supplementary Fig. 6a, b. The fibril backbones show axial height changes of 7.5 Å (fibril A) and 7.0 Å (fibril B), which lead to polar fibril topologies and sterically interlock the fibril layers. Each fibril protein layer interacts only with the layers above and below, e.g., Lys38 from layer i interacts with Asp81 from layer $i+1$ (Supplementary Fig. 6c).

The surfaces of both fibrils are rich in charged and polar amino acids (Fig. 2c ad Supplementary Fig. 5b). The fibril cores contain small hydrophobic patches, such as the one formed by residues Val10, Val12, Leu14, Val98, Phe99, Leu105, and Val107 (Fig. 2c and Supplementary Fig. 5b), as well as patches of buried polar residues. The structure buries a number of compensating charge–charge interactions, for example, at residues Asp25 and Arg28, Arg28 and Asp84, Lys38 and Asp81, Glu80 and Arg90 (Fig. 2c and Supplementary Fig. 5b), as well as an acidic moiety, which is not fully charge compensated. This moiety is formed by residues Glu80, Asp81, Glu82, and Asp84 (Fig. 2d), resembling the partially uncompensated acidic moiety in the previously described λ1 fibril structure[13]. In contrast to the previous λ1 fibril, however, there is no water-filled cavity around the acidic moiety in our fibril.

Location of aggregation-prone segments and mutations. The mutagenic changes of the amyloidogenic LCs compared with the GL sequences are widely believed to trigger amyloidosis in the respective patients[9,17]. However, analysis of the mutated positions within our structure does not readily offer an explanation for their pathogenicity. Some mutations, such as Asn51Ser and Val135Gly, lie within a part of the precursor protein that is disordered or cleaved off in the fibril (Fig. 2a). In addition, none of

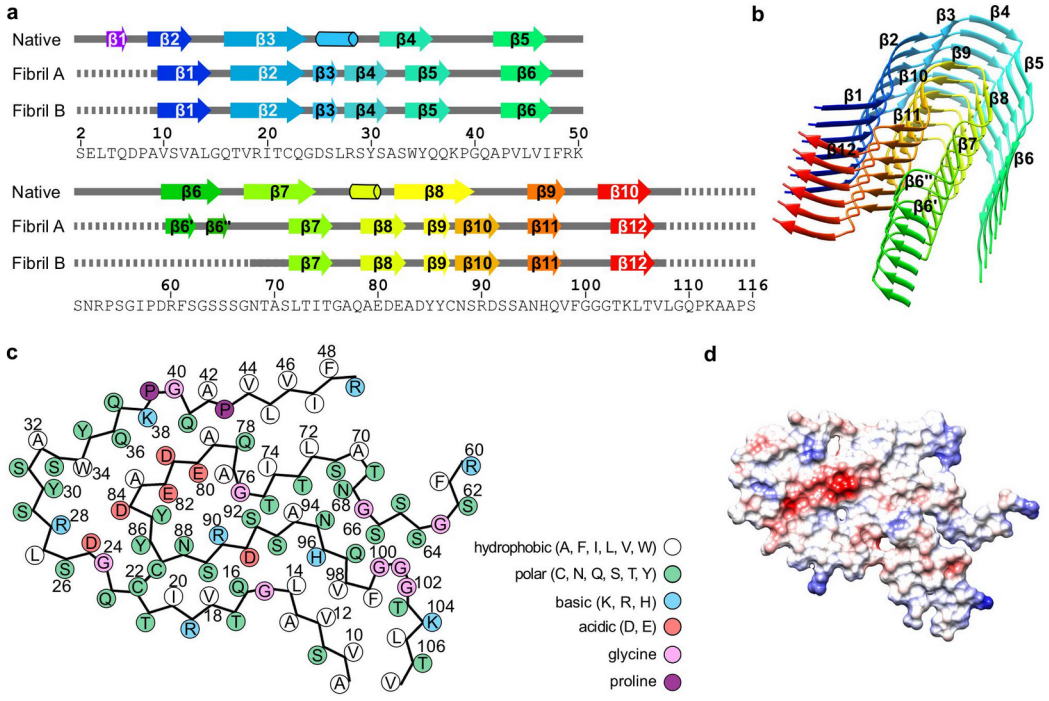

Fig. 2 Secondary structure and folding of the fibril proteins. a Schematic representation of the secondary structure of the fibril proteins A and B, and of a crystal structure of the refolded fibril protein (native, PDB: 5L6Q[10]). Arrows indicate β-strands and cylinders α-helical conformations. Continuous lines indicate ordered conformation, dotted lines indicate disordered segments. The definition of secondary structural elements follows the definition in the respective manuscripts. **b** Ribbon diagram of a stack of six fibril proteins (conformation A). β-strands have been colored in rainbow palette from the N- to the C-terminus. **c** Schematic representation of the amino acid positions in conformation A. **d** Electrostatic surface representation of the fibril protein conformation A. Red indicates negative charge, blue positive, and white neutral. Supplementary Figure 5 shows the corresponding images for fibril conformation B.

the mutations affecting the fibril core adds an obviously favorable interaction. The nonconservative Gly49Arg mutation even leads to a buried charge that is not compensated by a nearby opposite charge (Fig. 3a), suggesting that this mutation may even be unfavorable to the fibril structure. Moreover, analysis of the location of the mutations within the native LC does not readily provide evidence that they might be destabilizing to the native protein conformation (Supplementary Fig. 7a, b). The mutations do not remove an obviously stabilizing interaction and do not affect internal residues that might be considered to be crucial for protein stability. Instead, all mutations are located on the surface of the globularly folded LC (Supplementary Fig. 7a, b).

Computer-based predictions of the aggregation propensity of the FOR005 LC identified the highest aggregation score in the V_L domain at residues Val44–Arg49 (Fig. 3b and Supplementary Fig. 8). These residues form a hydrophobic patch on the fibril surface, which is decorated with the extra density region described above (Fig. 1c, d, blue star). The three disordered protein segments in the fibril protein (Ser2–Pro8, Lys50–Gly67, and Leu108–Ser116) correlate with regions having low aggregation scores (Supplementary Fig. 8). However, comparing the aggregation score of the FOR005 LC to that of the GL protein sequence (Supplementary Fig. 8) does not reveal any clear trend whether the FOR005 LC or its putative GL precursor is more aggregation prone (Supplementary Fig. 8). We conclude that the effect of mutation is subtle and not readily evident by the above analysis. Support for this view comes from a recent study in which the rather counterintuitive observation was reported that a conservative leucine to valine mutation on the surface of a patient-derived V_L domain is strongly destabilizing to the native protein structure, and promotes the formation of amyloid fibrils in vitro[18].

Conformations A and B coexist within the same fibrils. Finally, we sought to determine whether the two reconstructed 3D maps A and B represent two different fibril morphologies, or whether the two structures coexist within the same fibril particle. By visual inspection of the cryo-EM micrographs and measurement of global parameters, such as fibril width or crossover distance, we could not categorize the fibrils in our sample into separate structures A and B. Also, the reconstructed 3D maps have identical helical parameters, such as fibril symmetry, polarity, axial rise, and twist value, as well as a fibril pitch of 155 nm (Supplementary Table 1). The difference between the two structures could only be revealed when the fibril images were cropped into segments that were then aligned independently of their structural context during 3D classification.

Analyzing the origin of the fibril segments in the respective data sets producing reconstructions A and B, we would have expected, for separate morphologies, that each fibril contains segments belonging to only one of the two data sets A or B

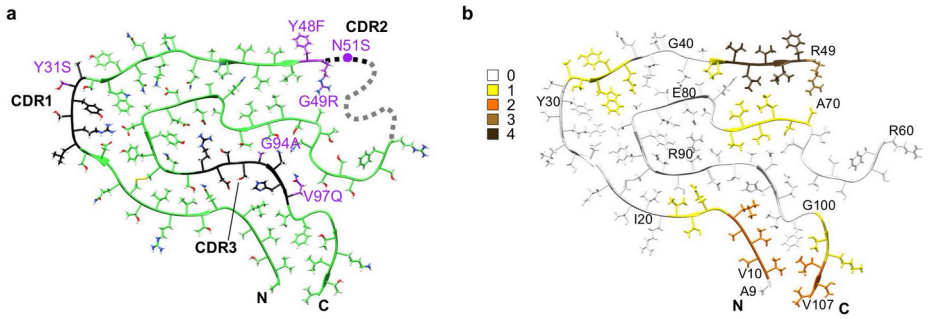

Fig. 3 Location of the mutational positions and aggregation-prone regions in the fibril structure. a Mutations with respect to the GL protein sequence (purple) and CDRs (black) marked in fibril structure A (green). The dotted line represents the intermedial disordered segment. **b** Molecular model of conformation A colored according to aggregation score.

(except for minor classification errors). Surprisingly, however, we found that most fibrils in our sample showed a mixture of A and B segments (Fig. 4a and Supplementary Fig. 9a). Fractions of type B segments per fibril varied almost continuously from 0 to 1 (Fig. 4b and Supplementary Fig. 9b). The assignment of segments to the fibril protein conformations A and B could not readily be correlated with certain positions on the fibril helix on the cryo-EM micrographs, for example, the crossover or the segment in between two crossovers, which might have suggested problems in their alignment. Moreover, the segments are not randomly distributed across the fibrils, but mostly separated into distinct regions along the fibril axis, in which all segments correspond to either structure A or B (Fig. 4a). These results were obtained consistently across different data sets, including the data set resulting from the initial 3D classification (Fig. 4a, b), as well as the data set from the final reconstructions (Supplementary Fig. 9a, b). In conclusion, the fibrils in our data set cannot simply be divided into two fibril morphologies A and B. Instead, the two fibril structures A and B occur simultaneously within a fibril protein stack. This observation indicates that there are structural breaks at the interface of fibril regions corresponding to structures A or B (Fig. 4c, d).

Discussion

We here present the cryo-EM structures of two amyloid fibrils (A and B) that were extracted from the explanted heart of a patient (FOR005) with systemic AL amyloidosis. The spatial resolutions are 3.2 Å for fibril structure A and 3.4 Å for fibril structure B (Supplementary Table 1). These resolutions are sufficient to establish the overall fibril topology and the fibril protein fold. However, uncertainty remains in the exact conformation of the backbone and side chains. This problem is further exacerbated by the known artifacts of cryo-EM structures, such as a loss of side chain density due to beam damage[19], which could be relevant in our reconstructions, e.g., at residues Glu80 or Lys104 (Fig. 1c, d).

Systemic AL amyloidosis is a patient-specific disease[9]. Identification of common structural features in different patient-derived amyloid fibrils is potentially informative about common steps in the misfolding pathways across patient cases. Based on the available cryo-EM structures of ex vivo fibrils from systemic AL amyloidosis (Fig. 5 and Supplementary Fig. 10), the following commonalities can now be identified: the extracted fibril samples contain a dominant fibril morphology that consists of a single, polar protofilament. The fibril core is formed by the V_L domain of the precursor λ-LC in all cases. The C_L domain is structurally disordered and/or lost by proteolysis. The fibril proteins retain the intramolecular disulfide bond of the native V_L domain, indicating that LC misfolding happens in an oxidative environment, such as the extracellular space or an endocytic compartment, that retains the disulfide bond of the native V_L domain. The fibril proteins show an antiparallel N-to-C orientation at the disulfide that is flipped by 180° relative to the native state. The fibril protein conformations differ substantially from the natively folded LC, demonstrating that a global structural rearrangement and/or unfolding reaction takes place during the conversion of the native LC, or of a LC fragment, into a fibril. The fibrils are decorated by blurry density of uncertain origin that may arise from fibril protein segments outside the ordered core, or cellular factors attached to the fibril surface.

Patient-specific features of the fibrils include the exact fold of the fibril protein (Fig. 5), and the location of the β-strands and disordered segments within the sequence (Supplementary Fig. 10). The current λ3- and the previous λ1-derived fibril proteins possess solvent-exposed and conformationally disordered N-termini, while the N-terminal segment of the λ6-derived fibril is buried in the fibril core and part of a β-strand (Fig. 5 and Supplementary Fig. 10). The C-termini are disordered in each of these fibril proteins. Our current fibril structures and the previous λ6 fibril structure each contain an internal, disordered segment interrupting the fibril protein fold. In contrast, the fold of the λ1 fibril protein is continuous (Fig. 5 and Supplementary Fig. 10). The λ1 fibril possesses three large channels, two of which are thought to be water-filled, while the third one contains an apolar molecular inclusion[13]. No such channels or inclusions were identified in the other fibril structures. A feature unique to the current λ3 fibrils is a well-resolved density island attached to the fibril core (Supplementary Fig. 4a, b).

Our structures also differ from a number of studies which used nuclear magnetic resonance (NMR) spectroscopy to investigate the structure of LC-derived fibrils formed in vitro. These fibrils were formed from V_L domain constructs and include murine κ (ref. [20]), human κ1 (ref. [21]), as well as human λ3 (ref. [22]) and λ6 sequences[23]. Particularly relevant in this case is the comparison of our structures to the NMR analysis of recombinant FOR005 V_L domain fibrils[22]. These fibrils were seeded in vitro with amyloid fibrils that were extracted from the heart of the patient (FOR005) with the aim to propagate the ex vivo fibril structure in the in vitro seeded fibrils[22]. Comparison of the in vitro seeded fibrils with our cryo-EM structures of patient fibrils revealed several differences. First, the ex vivo fibrils possess a stable β-strand at residues Thr103–Thr106 that are outside the ordered core of the in vitro seeded fibrils. Second, the in vitro seeded fibrils contain a salt bridge between residues Arg49 and

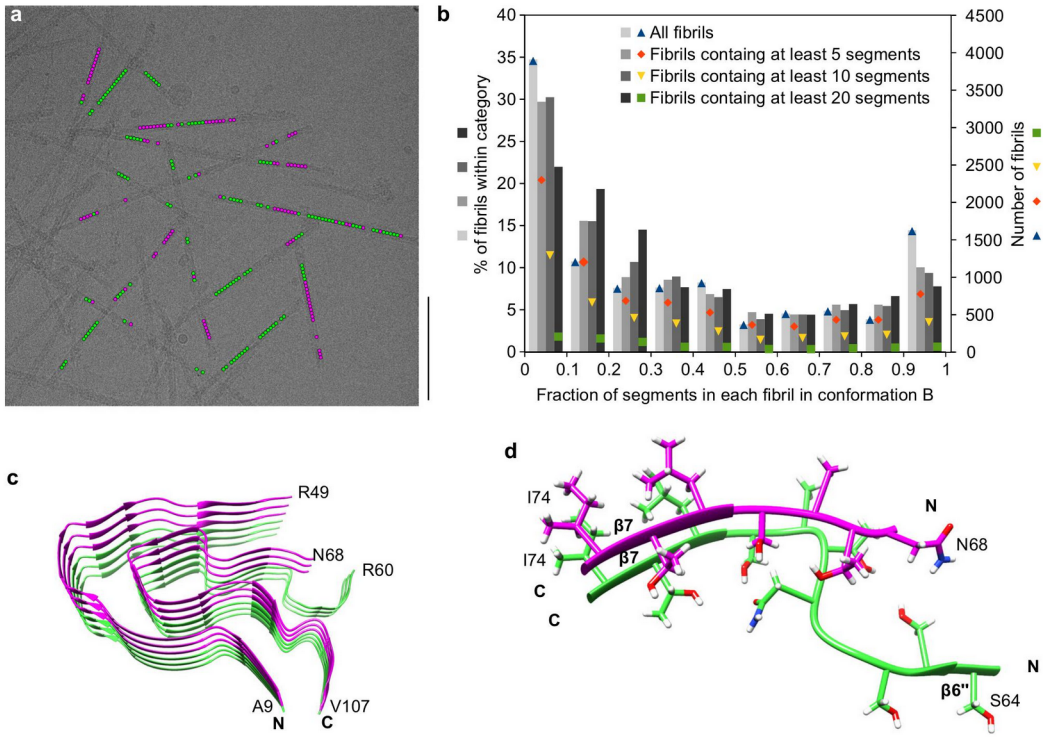

Fig. 4 Evidence for structural breaks in FOR005 fibrils. a Representative cryo-EM micrograph showing the location of segments classified after the first 3D classification as fibril structure A (green) and fibril structure B (magenta). Scale bar: 100 nm. Data were collected from 1,378 micrographs from one fibril sample. Supplementary Fig. 9a shows the same image, highlighting only the segments used in the final fibril reconstruction. **b** Histogram of the fraction of segments classified as fibril structure B, per fibril, after the first 3D classification. Different thresholds were chosen for the minimum number of segments per fibril, resulting in four categories: all fibrils (11,194 fibrils), fibrils containing a minimum of 5 segments (7,738 fibrils), fibrils containing a minimum of 10 segments (4,278 fibrils), and fibrils containing a minimum of 20 segments (951 fibrils). The percentages were normed using the total number of fibrils in each category. Colored points show the absolute number of fibrils in each category and group (fraction in conformation B). In total, the data set ($n = 101,319$) contained 64,652 segments classified as fibril structure A and 36,667 as fibril structure B. Supplementary Fig. 9b shows an analogous histogram, but including only the segments used for the final reconstructions. **c** Stack of three fibril proteins in conformation B (magenta) on top of three fibril proteins in conformation A (green), illustrating the presence of structural breaks within the patient amyloid fibrils. **d** Detailed view of a structural break, including side chains.

Asp25 (ref. [22]), which are far apart in the protein fold of the patient fibril (Fig. 2c). Third, the in vitro seeded fibrils show an electrostatic interaction between Lys50 and Asp81 (ref. [22]), whereas in the ex vivo fibrils, Lys50 is in the internal disordered region, and Asp81 is far away from this segment (Fig. 2c) and has an electrostatic interaction with Lys38 (Supplementary Fig. 6).

These data demonstrate that the in vitro fibrils are structurally different from the ex vivo fibrils analyzed here with cryo-EM. In vitro seeding with ex vivo FOR005 fibrils did not propagate, in this case, the seed structure to the daughter fibrils, although it modified the fibril structure compared with unseeded fibrils[22]. These observations imply that the seeding mechanism did not involve a replication of the seed structure. Early work with sickle cell hemoglobin identified two possible seeding mechanisms: homogeneous and heterogeneous nucleation. Homogeneous nucleation involves the attachment of the soluble fibril precursor proteins to the fibril tip, while heterogeneous nucleation involves the nucleation of new fibrils on the lateral cylindrical surface of an existing fibril[24]. While attachment of the fibril precursor protein to the tip of an amyloid fibril would be expected to lead to a replication of the fibril protein fold, this replication of the seed protein structure may not necessarily occur during heterogeneous seeding. Indeed, the observation of density islands on the outside of the FOR005 fibril core structure (Fig. 1c, d, red star and Supplementary Fig. 4a, b) suggests that fibril proteins may have attached on the fibril surface, but do not fully replicate the fold of the fibril protein. Hence, it is important to use patient-derived fibrils when investigating the structural basis of disease. A similar conclusion was obtained previously when FOR005 fibril protein was extracted from the patient's heart, denatured in guanidine, refolded, and fibrillated in vitro (without seeds). These in vitro fibrils also showed a different morphology than the fibrils that were purified from FOR005 patient tissue[10], as judged by transmission electron microscopy.

A particularly interesting finding in the present study is the observation of structural breaks. So far, it has been part of our general understanding of amyloid fibril structures that these are conformationally uniform along the fibril axis. Occasionally, fibrils were reported that differed morphologically at its two ends[25–28]. Some of these cases could be attributed to a fibril cross-

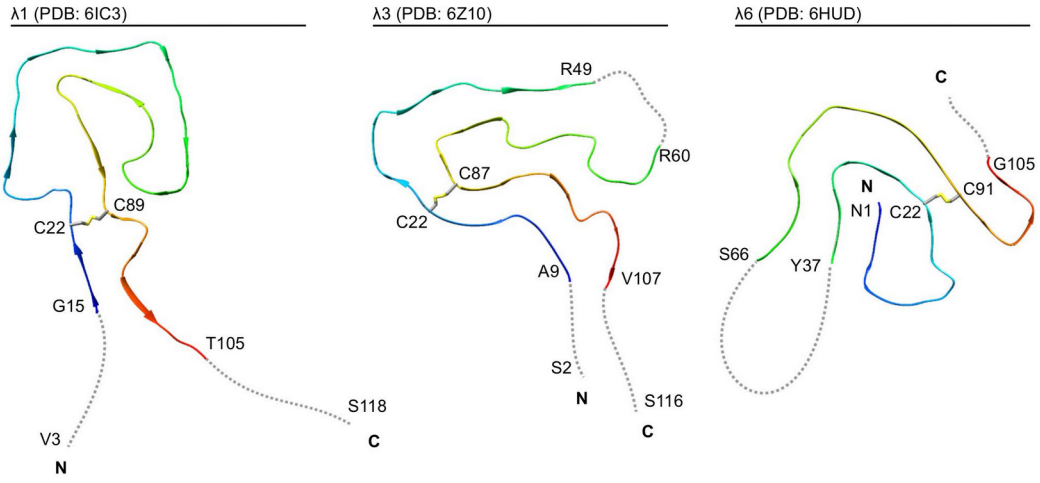

Fig. 5 Comparison of the available cryo-EM structures of ex vivo AL amyloid fibrils. Ribbon diagrams of a λ1 fibril (PDB: 6IC3[13]), the current λ3 fibril (conformation A, PDB: 6Z10), and a λ6 fibril (PDB: 6HUD[14]). The fibrils are shown in a cross-sectional view. For all structures, the location of the disulfide bond forming cysteine residues is marked. Disordered segments are represented as dotted gray lines and depicted in an arbitrary conformation. The first and the last residue of the ordered segments, as well as the first and the last residue of the fibril protein are indicated, if known.

seeding, that is, the attachment of a different fibril precursor protein to a fibril tip, or to a splintering of a multi-protofilament fibril into fibril morphologies with a smaller number, or a different arrangement of protofilaments. In other cases, it was unclear whether two fibril morphologies may have annealed after their formation. In our samples, however, the majority of fibrils show a mixture of conformations, and show multiple, seemingly arbitrary switching between the conformations A and B in each fibril. Therefore, short segments, possibly down to a single protein layer, may be able to adopt a conformation different from that of the surrounding layers. The fibril breaks and the two fibril structures defining the breaks emerged at the 3D classification stage in our analysis and resolved a previously blurry density region into two distinct density paths (Supplementary Fig. 1b). Unresolved density regions resulting from one or more disordered segments of the protein chain are reported for the majority of cryo-EM structures of in vitro and ex vivo amyloid fibrils[29]. Therefore, structural heterogeneity such as described here could be relevant to other fibril structures as well. Furthermore, it is possible that our fibrils contain fibril protein structures which we were unable to resolve so far. We originally extracted 194,502 fibril segments from the cryo-electron micrographs and used only 11,003 (A) and 12,122 (B) of these segments for the final 3D reconstructions (Supplementary Table 1).

Two possible scenarios can be envisioned to explain the mechanism of the formation of structural breaks. One scenario is that they appear during fibril assembly due to an imperfect replication of the seed structure, as a new molecule attaches to the fibril end (Fig. 6). Consistent with this idea, real-time microscopy studies explained the stop-and-go kinetics during fibril growth with irregularities in the addition of molecules to the tip of a growing fibril[30]. The other scenario is that breaks emerge after fibril assembly, for example, because initially disordered segments adopt different stable conformations, which then proliferate along the fibril axis (Fig. 6). Support for the latter mechanism is provided by the fact that the type A and B fibril proteins are mostly identical, and that the differences are confined to a small segment that lies in the vicinity of an unstructured region.

While more work is necessary to discriminate between these two mechanisms, our observations lead to an important change in our understanding of the assembly of polypeptide chains into amyloid fibrils. They demonstrate that these linear aggregates are not as perfectly regular and uniform as has generally been assumed by most previous studies. Considering that the breaks were revealed in the FOR005 fibril samples only at an advanced stage of the analysis, we would predict that they will be observed more frequently in the future, as the methods of structural biology become more powerful and will be able to resolve such fine details more routinely. Structural breaks and other structural defects in cross-β-sheets could have significant ramifications for the biological properties of amyloid fibrils. Examples hereof include the fragility[31] and the loss of torsional coherence of amyloid fibrils[32,33], the branching of amyloid fibrils during fibril outgrowth[34] and the ability of molecular chaperones to bind to, to sever, and to break down amyloid aggregates[35].

Methods

Source of AL fibrils. Heart tissue was collected from a female patient (FOR005) at the age of 50, suffering from AL amyloidosis and consequent advanced heart failure. A monoclonal gammopathy was the underlying condition. The patient was treated within the heart transplant program of the University Hospital Heidelberg. The explanted heart tissue was stored at −80 °C. The study was approved by the ethical committees of the University of Heidelberg (123/2006) and of Ulm University (203/18). Informed consent was obtained from the patient for the analysis of the amyloid deposits.

Fibril extraction from patient tissue. Applying a previously established protocol[11] for fibril extraction, 250 mg of patient heart tissue were diced finely and 0.5 mL of ice-cold Tris calcium buffer (20 mM Tris, 138 mM NaCl, 2 mM $CaCl_2$, 0.1 (w/v) % NaN_3, pH 8.0) added. The sample was homogenized using a Kontes Pellet Pestle, after which it was centrifuged for 5 min at 3100 × *g* at 4 °C. The washing step was repeated five times and each supernatant was stored for further analysis. Afterward, 1 mL of freshly prepared 5 mg mL^{-1} *Clostridium histolyticum* collagenase (Sigma) in Tris calcium buffer with ethylenediaminetetraacetic acid (EDTA)-free protease inhibitor (Roche) were added and the pellet resuspended. Overnight incubation at 37 °C was followed by a 30 min centrifuge cycle at 3100 × *g*. Ten further washing steps with 20 mM Tris, 140 mM NaCl, 10 mM EDTA, and 0.1 % (w/v) NaN_3 and ten subsequent steps with ice-cold water

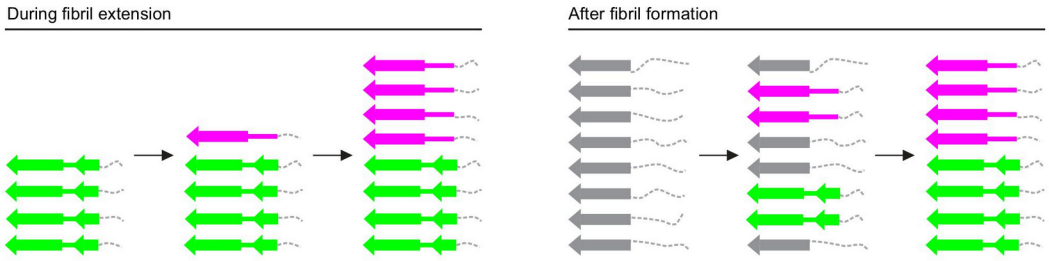

Fig. 6 The origin of structural breaks: two possible scenarios. Schematic representation of a stack of fibril proteins, illustrating two different hypotheses on how structural breaks form: during fibril extension (left) or after fibril formation (right). Conformation A is represented by two β-sheets (green). Conformation B is represented by one β-sheet (magenta). Disordered segments are represented by dotted gray lines. Gray arrows represent the immature fibril proteins, before the mature conformations A and B are fully adopted.

were then performed on the pellet, using a pipette for homogenization. One of the water supernatants was selected for cryo-EM.

Cryo-EM. Holey carbon-coated grids (C-flat 1.2/1.3 400 mesh) were glow-discharged using 40 mA for 40 s. Using a Vitrobot (Thermo Fisher Scientific), 3.5 µL of the extracted fibril sample were incubated on each grid for 30 s at a humidity of >95%, the excess fluid was blotted off and the grid plunged into liquid ethane, then transferred to a grid box. After plunging, one grid from each grid box (containing four grids) was checked using a 200 kV Jeol JEM 2100 F electron microscope (Ulm University). The remaining grids in the grid boxes were kept at liquid nitrogen temperature. Cryo-electron microscopic image acquisition of one selected grid was performed using a Titan Krios transmission electron microscope (Thermo Fisher Scientific) at 300 kV equipped with a K2-Summit detector (Gatan) in counting mode. A Gatan imaging filter with a 20 eV slit was applied. The software package SerialEM v3.7 was used for data collection. The data acquisition parameters can be found in Supplementary Table 1. Global parameters of the fibril morphologies were measured using Fiji[36]. No clearly identifiable second morphology was found and the occurrence of the main morphology was estimated at over 95%.

Helical reconstruction. Helical reconstruction was performed using Relion 2.1 (ref. [37]). The raw data were converted from TIFF to mrcs format using IMOD[38]. Motion and gain corrections, as well as dose-weighting were performed using Motioncor2 (ref. [39]). The non-dose-weighted micrographs were used to determine the defocus values with Gctf[40], whereas the dose-weighted micrographs were used for all subsequent steps. Fibrils were manually selected from 1,964 micrographs and segments were extracted with a box size of 300 pixels (312 Å) with an inter-box distance of 33.6 Å (~11%). Two rounds of reference-free 2D classification were performed with a regularization value of $T = 2$. Class averages which showed the helical repeat along the fibril axis were selected, whereas classes showing artifacts and noise were discarded, resulting in a selection of 101,319 particles. The selection was confirmed by manually arranging the class averages into a full 2D fibril side view. An initial model from a previous reconstruction was filtered to 60 Å resulting in a rod-like structure. This initial model was used as a reference to create a first 3D map using 3D classification with 553 particles picked from nine micrographs. The resulting map was used as a reference for 3D classification with six classes and $T = 3$ using the 101,319 particles obtained from the 2D classification selection. Three of the six classes showed a clear backbone and revealed the presence of two different conformations. These classes were selected (60,044 particles) and further rounds of 3D classification with four classes and step-wise increasing T-values from 3 to 20 were performed. Approximately 11,003 particles were selected for conformation A and 12,122 particles for conformation B. Final round of 3D classification with increasing T-values from 80 to 200, followed by 3D auto-refinement and post-processing with a soft-edged mask and an estimated sharpening B-factor of −33.1013 Å² (conformation A) and −55.1958 Å² (conformation B) for each of the two conformations led to the post-processed maps. Helical z-percentages used for 3D classification and 3D refinement varied between 0.1 and 0.3. The twist and rise were 1.11 and 4.79, respectively, for both conformations. These values agree with the measured crossover distances on the motion-corrected cryo-EM micrographs, and the corresponding power spectra. A left-handed twist was assumed. The resolution of each map was estimated from the value of the FSC curve for two independently refined half-maps at 0.143.

Model building and refinement. The model was manually built using the software Coot[41]. The process was initiated by tracing a poly-Ala chain along the 3D map. The alanine residues were mutated to the LC sequence as determined previously[11]. The model obtained was subjected to manual, as well as automated refinement using phenix.real_space_refine[42,43] tool, as implemented in phenix with non-crystallographic symmetry and secondary structure restraints imposed. This process was repeated until a satisfactory map to model fit was obtained. This model was subsequently used to perform model based automated sharpening of the map (phenix.auto_sharpen[42,43]). The sharpened map was used for improving the model further. The final refined model was evaluated for its quality using the MolProbity[44] validation report.

Sequence analysis. The amino acid sequence of the LC investigated in this study was taken from the gene bank entry KX290463 (ref. [10]), which was obtained by cDNA sequencing of FOR005 patient material. The residue numbering throughout this article refers to the precursor LC sequence (GenBank ANN81988.1) from the patient, starting with the first residue (Ser1) after the signal sequence, which is cleaved off in the fibril protein. All mutations in this manuscript are represented in the direction GL to FOR005 fibril protein. The sequence elements were defined as follows. First, the patient cDNA was translated to the putative amino acid sequence of the fibril precursor protein. Then, the cDNA of the patient and the corresponding amino acid sequence were analyzed to determine the most probable GL segments, using the vbase2 (ref. [45]) and BLAST/BLAT search tools[46] (http://www.ensembl.org). This analysis yielded several hits for possible GL segments. The cDNA sequences and corresponding amino acid sequences of these V, J, and C GL segments were retrieved from the vbase2 (ref. [45]), ENSEMBL[47], and http://www.imgt.org[48] databases, and genetic distances to the patient sequence were calculated by maximum composite likelihood to confirm the most probable V, J, and C GL segments. Finally, the cDNA sequence of the patient and the corresponding amino acid sequence were aligned to these GL segments (fit > 80%), using the MEGA multiple sequencing alignment tool "MUSCLE"[49] and Clustal Omega (https://www.ebi.ac.uk/Tools/msa/clustalo/)[50] to identify patient-specific mutations. The definitions of the CDRs were taken from a previous manuscript[10].

LC aggregation propensities for every residue were calculated using the programs TANGO[51], Foldamyloid[52], Aggrescan[53], and PASTA 2.0 (ref. [54]). For every prediction tool standard parameters were chosen. For Tango (Version 2.1), every amino acid which scores above 5% was counted as a hit. For Foldamyloid, the "triple hybrid" scale was used, meaning that five successive amino acids with a score above 21.4 were counted as hits. PASTA 2.0 calculated aggregation with 90% sensitivity and predicted hits if the energy cutoff fell below −2.8 PASTA Energy Units. For Aggrescan, all amino acids with values above −0.02 were counted as hot spots. In this study, an aggregation score of 0 means that none of these programs identified the corresponding residue as aggregation prone. An aggregation score of 4 means that all four programs identified the corresponding residue as prone to aggregation.

Protein structure representation. UCSF Chimera[55] was used for creating the images of the density maps and protein models. The structure of the refolded FOR005 fibril protein was obtained previously using protein X-ray crystallography and has the protein data bank (PDB) entry 5L6Q[10]. The native C_L domain is the *IGLC2* segment of PDB 4EOW[56], where the side chain of residue Val135 was not shown in order to represent the mutated residue Gly135 of the fibril protein. The following previously published coordinates were used in Fig. 5: 6IC3 and 6HUD.

Reporting summary. Further information on research design is available in the Nature Research Reporting Summary linked to this article.

Data availability

The reconstructed cryo-EM maps were deposited in the Electron Microscopy Data Bank with accession codes EMD-11031 (structure A) and EMD-11030 (structure B). The coordinates of the fitted atomic model were deposited in the PDB under the accession codes 6Z10 (structure A) and 6Z1I (structure B). The cryo-EM data were deposited on EMPIAR with the accession code EMPIAR-10457. The data sets used during the current

study are available from the corresponding author on reasonable request. The unique materials used in the current study are available from the authors on reasonable request. Source data are provided with this paper.

Received: 5 August 2020; Accepted: 21 December 2020;
Published online: 08 February 2021

References

1. Quock, T. P., Yan, T., Chang, E., Guthrie, S. & Broder, M. S. Epidemiology of AL amyloidosis: a real-world study using US claims data. *Blood Adv.* **2**, 1046–1053 (2018).
2. Shimazaki, C. Current diagnosis and treatment of AL amyloidosis in Japan: a nationwide epidemiological survey. *Rinsho Ketsueki* **60.8**, 973–978 (2019).
3. Wisniowski, B. et al. The epidemiology of amyloidosis in Queensland, Australia. *Br. J. Haematol.* **186.6**, 829–836 (2019).
4. Merlini, G. et al. Systemic immunoglobulin light chain amyloidosis. *Nat. Rev. Dis. Prim.* **4**, 1–19 (2018).
5. Blancas-Mejía, L. M. & Ramirez-Alvarado, M. Systemic amyloidoses. *Annu. Rev. Biochem* **82**, 745–774 (2013).
6. Perfetti, V. et al. The repertoire of lambda light chains causing predominant amyloid heart involvement and identification of a preferentially involved germline gene, IGLV1-44. *Blood* **119**, 144–150 (2012).
7. Kourelis, T. V. et al. Clarifying immunoglobulin gene usage in systemic and localized immunoglobulin light-chain amyloidosis by mass spectrometry. *Blood* **129**, 299–306 (2017).
8. Vaxman, I., Dispenzieri, A., Muchtar, E. & Gertz, M. New developments in diagnosis, risk assessment and management in systemic amyloidosis. *Blood Rev.* **40**, 100636 (2020).
9. Bellotti, V., Mangione, P. & Merlini, G. Review: immunoglobulin light chain amyloidosis—the archetype of structural and pathogenic variability. *J. Struct. Biol.* **130**, 280–289 (2000).
10. Annamalai, K. et al. Common fibril structures imply systemically conserved protein misfolding pathways in vivo. *Angew. Chem. Int. Ed.* **56.26**, 7510–7514 (2017).
11. Annamalai, K. et al. Polymorphism of amyloid fibrils in vivo. *Angew. Chem. Int. Ed.* **55.15**, 4822–4825 (2016).
12. Glenner, G. G., Harbaugh, J., Ohms, J. I., Harada, M. & Cuatrecasas, P. An amyloid protein: the amino-terminal variable fragment of an immunoglobulin light chain. *Biochem. Biophys. Res. Commun.* **41**, 1287–1289 (1970).
13. Radamaker, L. et al. Cryo-EM structure of a light chain-derived amyloid fibril from a patient with systemic AL amyloidosis. *Nat. Commun.* **10.1**, 1–8 (2019).
14. Swuec, P. et al. Cryo-EM structure of cardiac amyloid fibrils from an immunoglobulin light chain AL amyloidosis patient. *Nat. Commun.* **10.1**, 1–9 (2019).
15. Boyer, D. R. et al. Structures of fibrils formed by α-synuclein hereditary disease mutant H50Q reveal new polymorphs. *Nat. Struct. Mol. Biol.* **26**, 1044–1052 (2019).
16. Cao, Q., Boyer, D. R., Sawaya, M. R., Ge, P. & Eisenberg, D. S. Cryo-EM structures of four polymorphic TDP-43 amyloid cores. *Nat. Struct. Mol. Biol.* **26**, 619–627 (2019).
17. Blancas-Mejia, L. M. et al. Immunoglobulin light chain amyloid aggregation. *Chem. Commun.* **54.76**, 10664–10674 (2018).
18. Kazman, P. et al. Fatal amyloid formation in a patient's antibody light chain is caused by a single point mutation. *Elife* **9**, e52300 (2020).
19. Wang, J. & Moore, P. B. On the interpretation of electron microscopic maps of biological macromolecules. *Protein Sci.* **26.1**, 122–129 (2017).
20. Hora, M. et al. MAK33 antibody light chain amyloid fibrils are similar to oligomeric precursors. *PLoS ONE* **12.7**, e0181799 (2017).
21. Piehl, D. W., Blancas-Mejía, L. M., Ramirez-Alvarado, M. & Rienstra, C. M. Solid-state NMR chemical shift assignments for AL-09 V L immunoglobulin light chain fibrils. *Biomol. NMR Assign.* **11**, 45–50 (2017).
22. Pradhan, T. et al. Seeded fibrils of the germline variant of human λ-III immunoglobulin light chain FOR005 have a similar core as patient fibrils with reduced stability. *J. Biol. Chem.* **295**, 18474–18484 (2020).
23. Lecoq, L. et al. A substantial structural conversion of the native monomer leads to in-register parallel amyloid fibril formation in light-chain amyloidosis. *Chembiochem* **20.8**, 1027–1031 (2019).
24. Ferrone, F. A., Hofrichter, J. & Eaton, W. A. Kinetics of sickle hemoglobin polymerization: I. Studies using temperature-jump and laser photolysis techniques. *J. Mol. Biol.* **183**, 591–610 (1985).
25. Crowther, R. A. Straight and paired helical filaments in Alzheimer disease have a common structural unit. *Proc. Natl Acad. Sci. USA* **88**, 2288–2292 (1991).
26. Makarava, N., Ostapchenko, V. G., Savtchenko, R. & Baskakov, I. V. Conformational switching within individual amyloid fibrils. *J. Biol. Chem.* **284**, 14386–14395 (2009).
27. Zhang, W. et al. Heparin-induced tau filaments are polymorphic and differ from those in Alzheimer's and Pick's diseases. *Elife* **8**, e43584 (2019).
28. Kollmer, M. et al. Cryo-EM structure and polymorphism of Aβ amyloid fibrils purified from Alzheimer's brain tissue. *Nat. Commun.* **10.1**, 1–8 (2019).
29. Gallardo, R., Ranson, N. E. & Radford, S. E. Amyloid structures: much more than just a cross-β fold. *Curr. Opin. Struct. Biol.* **60**, 7–16 (2020).
30. Ferkinghoff-Borg, J. et al. Stop-and-go kinetics in amyloid fibrillation. *Phys. Rev. E* **82**, 010901 (2010).
31. Ndlovu, H., Ashcroft, A. E., Radford, S. E. & Harris, S. A. Molecular dynamics simulations of mechanical failure in polymorphic arrangements of amyloid fibrils containing structural defects. *Beilstein J. Nanotechnol.* **4**, 429–440 (2013).
32. Knowles, T. P., Smith, J. F., Craig, A., Dobson, C. M. & Welland, M. E. Spatial persistence of angular correlations in amyloid fibrils. *Phys. Rev. Lett.* **96**, 238301 (2006).
33. Knowles, T. P., Smith, J. F., Devlin, G. L., Dobson, C. M. & Welland, M. E. Analysis of structural order in amyloid fibrils. *Nanotechnology* **18**, 044031 (2006).
34. Andersen, C. B. et al. Branching in amyloid fibril growth. *Biophys. J.* **96**, 1529–1536 (2009).
35. Gao, X. et al. Human Hsp70 disaggregase reverses Parkinson's-linked α-synuclein amyloid fibrils. *Mol. Cell* **59**, 781–793 (2015).
36. Schindelin, J. et al. Fiji: an open-source platform for biological-image analysis. *Nat. Methods* **9**, 676–682 (2012).
37. He, S. & Scheres, S. H. W. Helical reconstruction in RELION. *J. Struct. Biol.* **198**, 163–176 (2017).
38. Kremer, J. R., Mastronarde, D. N. & McIntosh, J. R. Computer visualization of three-dimensional image data using IMOD. *J. Struct. Biol.* **116**, 71–76 (1996).
39. Zheng, S. Q. et al. MotionCor2: anisotropic correction of beam-induced motion for improved cryo-electron microscopy. *Nat. Methods* **14**, 331–332 (2017).
40. Zhang, K. Gctf: Real-time CTF determination and correction. *J. Struct. Biol.* **193**, 1–12 (2016).
41. Emsley, P., Lohkamp, B., Scott, W. G. & Cowtan, K. Features and development of Coot. *Acta Crystallogr. D Biol. Crystallogr.* **66**, 486–501 (2010).
42. Afonine, P. V. et al. New tools for the analysis and validation of cryo-EM maps and atomic models. *Acta Crystallogr. D Struct. Biol.* **74**, 814–840 (2018).
43. Afonine, P. V. et al. Real-space refinement in PHENIX for cryo-EM and crystallography. *Acta Crystallogr. D Struct. Biol.* **74**, 531–544 (2018).
44. Williams, C. J. et al. MolProbity: more and better reference data for improved all atom structure validation. *Protein Sci.* **27.1**, 293–315 (2018).
45. Retter, I., Althaus, H. H., Munch, R. & Muller, W. VBASE2, an integrative V gene database. *Nucleic Acids Res.* **33**, D671–D674 (2005).
46. Altschul, S. F., Gish, W., Miller, W., Myers, E. W. & Lipman, D. J. Basic local alignment search tool. *J. Mol. Biol.* **215**, 403–410 (1990).
47. Hunt, S. E. et al. Ensembl variation resources. *Database* **2018**, bay119 (2018).
48. Ruiz, M. et al. IMGT, the international ImMunoGeneTics database. *Nucleic Acids Res.* **28**, 219–221 (2000).
49. Tamura, K., Stecher, G., Peterson, D., Filipski, A. & Kumar, S. MEGA6: molecular evolutionary genetics analysis version 6.0. *Mol. Biol. Evol.* **30**, 2725–2729 (2013).
50. Sievers, F. et al. Fast, scalable generation of high-quality protein multiple sequence alignments using Clustal Omega. *Mol. Syst. Biol.* **7**, 539 (2011).
51. Fernandez-Escamilla, A. M., Rousseau, F., Schymkowitz, J. & Serrano, L. Prediction of sequence-dependent and mutational effects on the aggregation of peptides and proteins. *Nat. Biotechnol.* **22**, 1302–1306 (2004).
52. Garbuzynskiy, S. O., Lobanov, M. Y. & Galzitskaya, O. V. FoldAmyloid: a method of prediction of amyloidogenic regions from protein sequence. *Bioinformatics* **26**, 326–332 (2010).
53. Conchillo-Solé, O. et al. AGGRESCAN: a server for the prediction and evaluation of "hot spots" of aggregation in polypeptides. *BMC Bioinformatics* **8**, 65 (2007).
54. Walsh, I., Seno, F., Tosatto, S. C. & Trovato, A. PASTA 2.0: an improved server for protein aggregation prediction. *Nucleic Acids Res.* **42**, W301–W307 (2014).
55. Pettersen, E. F. et al. UCSF Chimera—a visualization system for exploratory research and analysis. *J. Comput. Chem.* **25**, 1605–1612 (2004).
56. Blech, M. et al. Molecular structure of human GM-CSF in complex with a disease-associated anti-human GM-CSF autoantibody and its potential biological implications. *Biochem. J.* **447.2**, 205–215 (2012).

Acknowledgements

We would like to thank the Deutsche Forschungsgemeinschaft for funding of the Research Unit FOR 2969, projects FA 456/27, HA 7138/3, HE 8472/1-1, HU 2400/1-1, and SCHO 1364/2-1. We are grateful to Prof. Dr. Bernd Reif (Technical University Munich) for helpful discussions and to the students who participated in the practical course "Protein Biochemistry and Structural Biology" in the winter semester 2019, for assisting in the manual picking of the fibril segments. All cryo-EM data were collected at the European Molecular Biology Laboratory, Heidelberg (Germany), funded by iNEXT (Horizon 2020, European Union).

Author contributions

L.R. and J.B. carried out experiments. L.R, J.B., S.H., C.H., A.B., M.S., and M.F. analyzed data. U.H. and S.S. contributed tools and reagents. M.F. designed research. L.R. and M.F. wrote the paper.

Funding

Open Access funding enabled and organized by Projekt DEAL.

Competing interests

The authors declare no competing interests.

Additional information

Supplementary information The online version contains supplementary material available at https://doi.org/10.1038/s41467-021-21126-2.

Correspondence and requests for materials should be addressed to M.F.

Peer review information *Nature Communications* thanks Luis del Pozo-Yauner and the other, anonymous, reviewer(s) for their contribution to the peer review of this work.

Reprints and permission information is available at http://www.nature.com/reprints

Publisher's note Springer Nature remains neutral with regard to jurisdictional claims in published maps and institutional affiliations.

Open Access This article is licensed under a Creative Commons Attribution 4.0 International License, which permits use, sharing, adaptation, distribution and reproduction in any medium or format, as long as you give appropriate credit to the original author(s) and the source, provide a link to the Creative Commons license, and indicate if changes were made. The images or other third party material in this article are included in the article's Creative Commons license, unless indicated otherwise in a credit line to the material. If material is not included in the article's Creative Commons license and your intended use is not permitted by statutory regulation or exceeds the permitted use, you will need to obtain permission directly from the copyright holder. To view a copy of this license, visit http://creativecommons.org/licenses/by/4.0/.

© The Author(s) 2021

Supplementary Figure 1

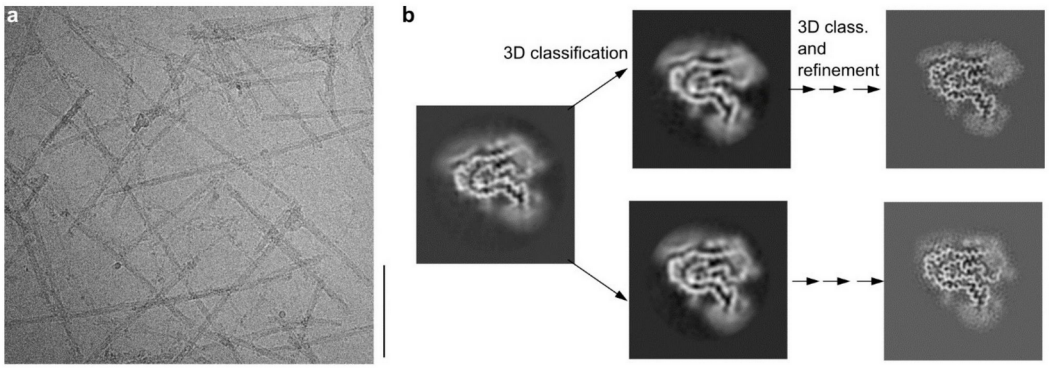

Supplementary Fig. 1

Work flow of steps of the reconstruction process.

(a) Representative cryo-EM image of the extracted fibrils. Scale bar: 100 nm. In total, 1,390 micrographs were analyzed from one fibril sample. (b) Schematic illustration of the workflow. Based on an initial reconstruction, 3D classification separated two subsets exhibiting different density paths. Through several further classification and refinement steps, the final reconstructions were obtained.

Supplementary Figure 2

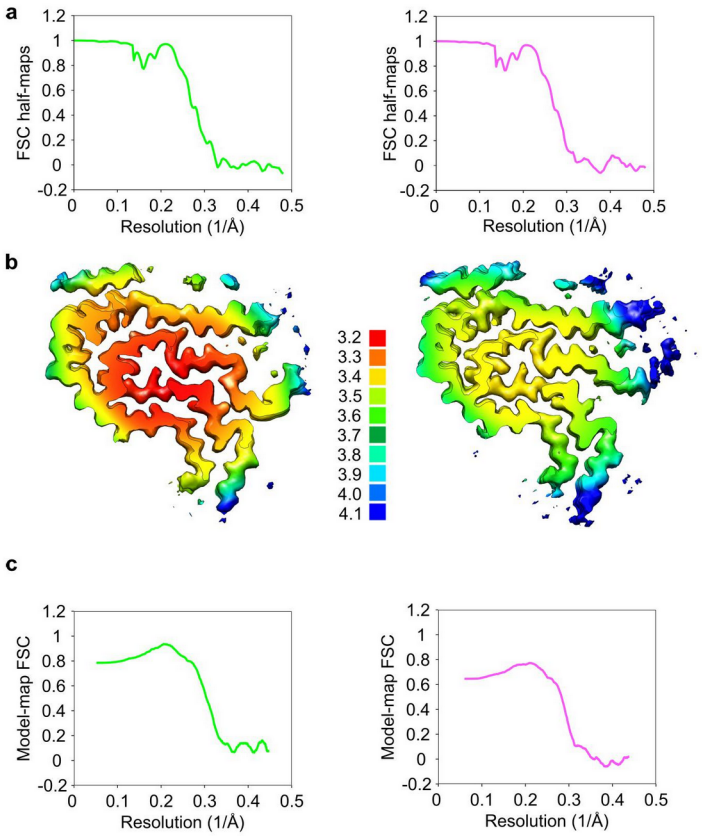

Supplementary Fig. 2

Map resolution and model fit.

(a) FSC curves for fibril structures A (green, left) and B (magenta, right). (b) Local resolution maps for A (left) and B (right). (c) Model-map FSC curves for models of conformation A (green, left) and B (magenta, right)

Supplementary Figure 3

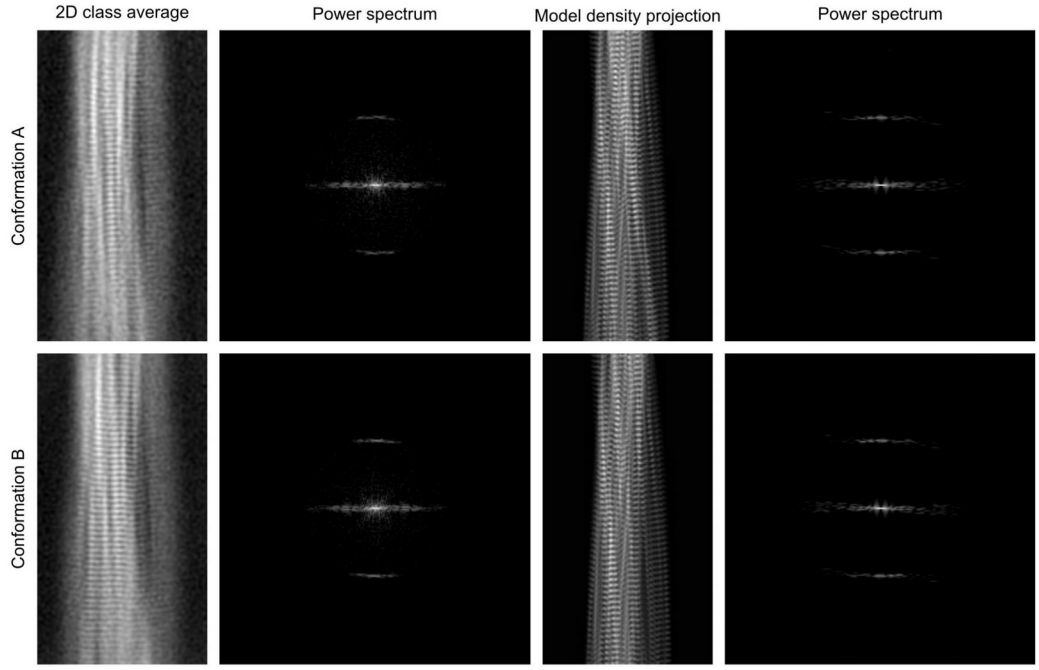

Supplementary Fig. 3

Comparison of the molecular models with 2D class averages.

For the two conformations A and B respectively, 2D class averages and model density projections corresponding to the same fibril regions are shown, with their respective power spectra. The length of the fibril section is approximately 266 Å.

Supplementary Figure 4

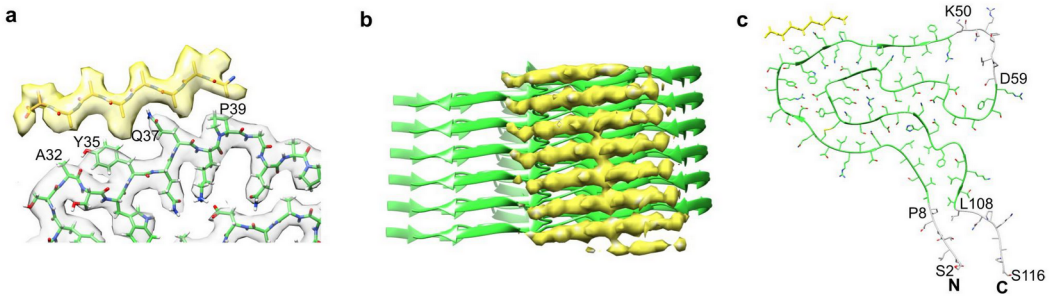

Supplementary Fig. 4

Defined extra density decorating the fibril surface.

(a) Enlarged view of the defined extra density (yellow) seen in structure A (green), overlayed with an 8-residue poly-L-alanine chain in parallel β-sheet conformation (yellow). (b) Side view of the defined extra density (yellow) next to the molecular model of a stack of fibril proteins in conformation A (ribbon diagram, green) showing the rise along the z-axis as well as the offset between the extra density and the fibril protein model. (c) Ribbon diagram including side chains of a single fibril protein layer in conformation A (green) showing all residues in the fibril protein including the disordered N- (Ser2-Pro8) and C-terminus (Leu108-Ser116) and the central disordered region (Lys50-Asp59) marked in gray, as well as the 8-residue poly-L-alanine chain as in (a) (yellow), representing the defined extra density. The gray segments are depicted in arbitrary conformation.

Supplementary Figure 5

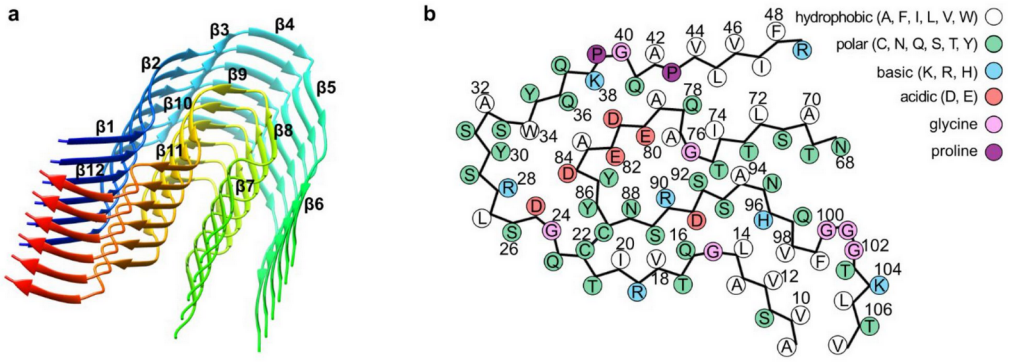

Supplementary Fig. 5

Structural features of fibril protein conformation B.

(a) Ribbon diagram of a stack of six fibril proteins in conformation B. β-strands have been colored in rainbow palette from the N- to C-terminus. (b) Schematic representation of the amino acid positions in conformation B. See Fig. 2b, c for the corresponding images showing conformation A.

Supplementary Figure 6

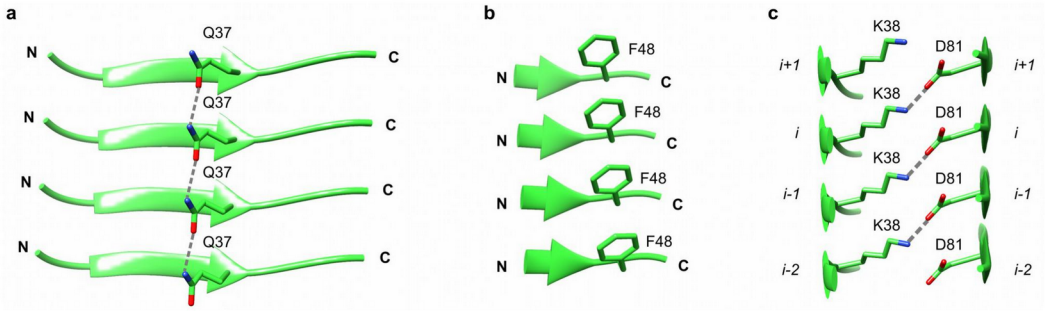

Supplementary Fig. 6

Side chain-side chain interactions across the layers of the fibril model.

(a) Stack of four fibril protein layers showing a polar ladder formed by Gln37 residues. (b) Four Phe48 residues in a configuration allowing for π-π (aromatic) stacking. (c) Electrostatic interactions between Lys38 of layer *i* and Asp81 of layer *i+1* demonstrating the interlocking of fibril protein layers. The images are based on a model of fibril structure A (green).

Supplementary Figure 7

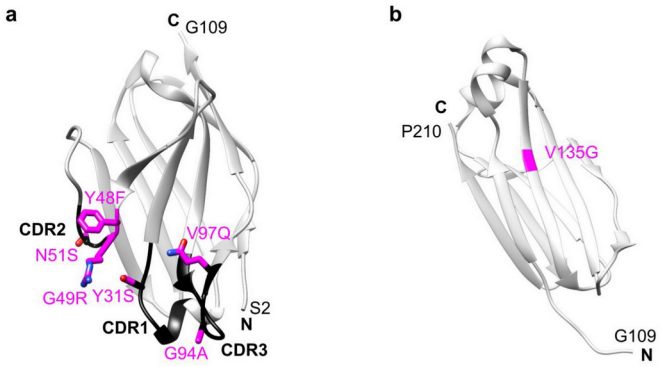

Supplementary Fig. 7

Location of the FOR005 mutations within the natively folded LC domains.

(a) Location of the mutations (magenta) and CDRs (black) within the structure of the refolded FOR005 fibril protein (PDB: 5L6Q[1]). (b) Location of the Val135Gly mutation (magenta), in the C_L domain of a homologous LC, containing an *IGLC2* GL segment (adapted from PDB: 4EOW[2] see methods for details). N- and C-terminal residues are marked.

Supplementary Figure 8

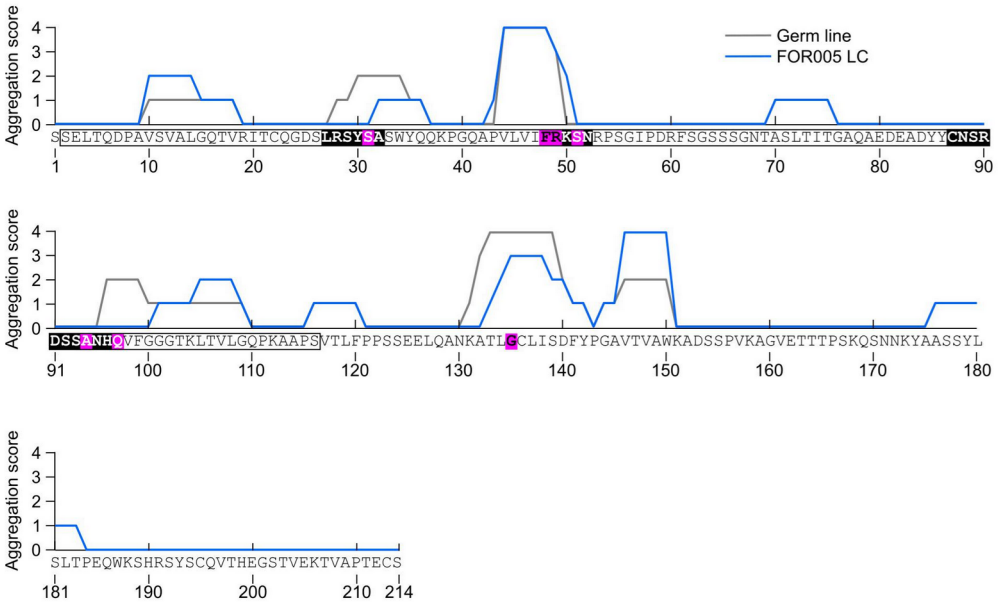

Supplementary Fig. 8

Aggregation score of the FOR005 precursor LC and of the corresponding GL protein sequence.

Aggregation score of the FOR005 LC precursor protein sequence (blue) and of the corresponding GL protein sequence (gray). The sequence on the x-axis is the FOR005 LC precursor protein sequence. The box denotes the range of the fibril protein (Ser2-Ser116). CDRs are indicated by white letters with black boxes. Mutations in the CDRs are indicated by white letters with magenta boxes. Mutations outside of the CDRs are indicated by black letters with magenta boxes.

Supplementary Figure 9

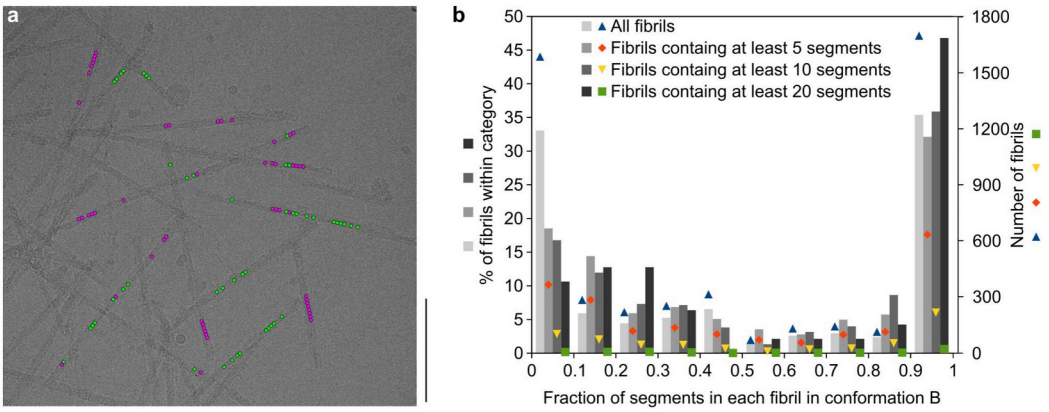

Supplementary Fig. 9

Evidence for structural breaks after the final round of 3D classification

(a) Representative cryo-EM micrograph showing the location of segments classified as fibril structure A (green) and fibril structure B (magenta) after the final round of 3D classification. Scale bar: 100 nm. Data were collected from 1,130 micrographs from one fibril sample. Figure 4a shows the same image, highlighting all the segments from the first round of 3D classification. (b) Histogram of the fraction of segments classified as fibril structure B, per fibril, after the final 3D classification. Different thresholds were chosen for the minimum number of segments per fibril, resulting in four categories: all fibrils (4,795 fibrils), fibrils containing a minimum of 5 segments (1,970 fibrils), fibrils containing a minimum of 10 segments (602 fibrils) and fibrils containing a minimum of 20 segments (47 fibrils). The percentages were normed using the total number of fibrils in each category. Colored points show the absolute number of fibrils in each category and group (fraction in conformation B). The data set (n = 23,124) contained 11,003 segments for fibril structure A and 12,122 segments for fibril structure B. Figure 4b shows an analogous histogram including all the segments from the first round of 3D classification.

Supplementary Figure 10

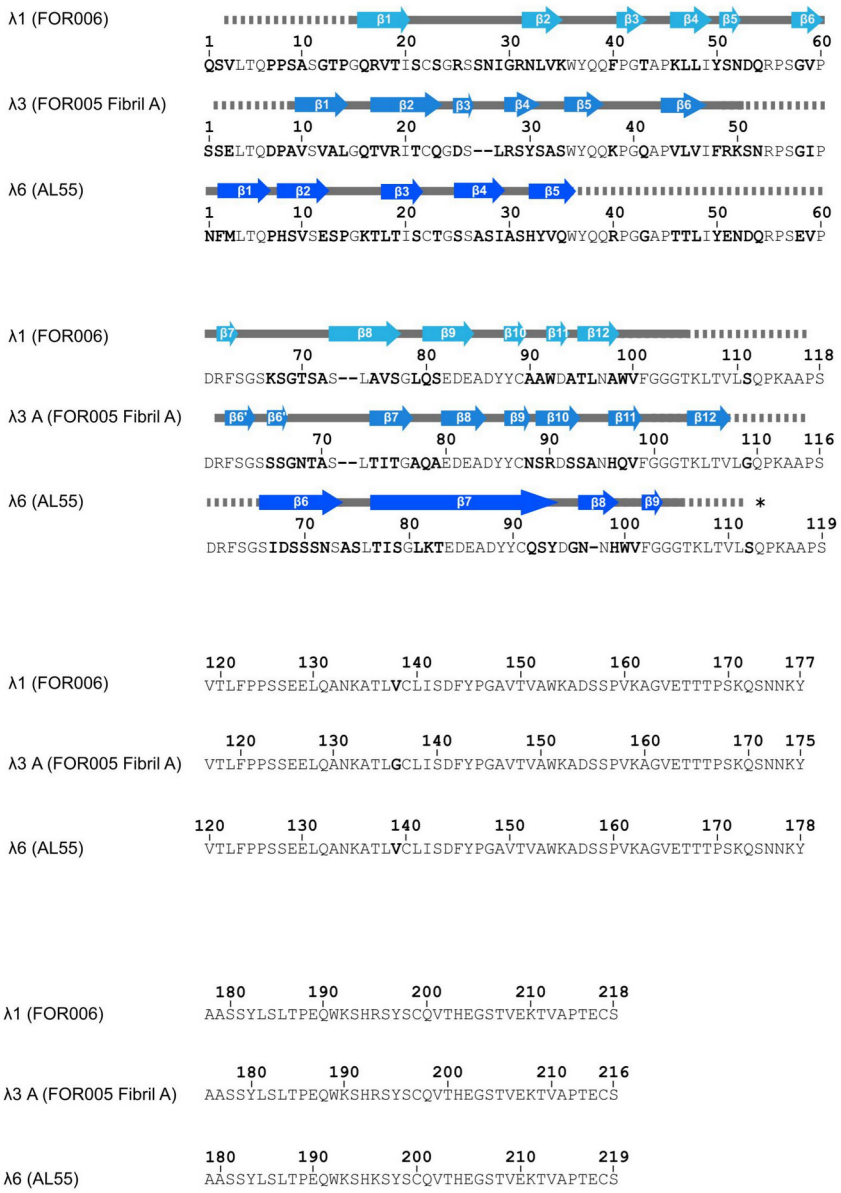

Supplementary Fig. 10

Sequence alignment and secondary structure comparison of ex vivo AL amyloid fibrils.

Sequence alignment of ex vivo AL amyloid fibril LCs for which a cryo-EM structures is available, combined with a schematic representation of the secondary structure of these fibrils. Non-conserved residues are marked in bold. Arrows indicate β-strands. Continuous lines indicate ordered conformation, dotted lines indicate disordered segments. Star: no single truncation site reported. The definition of secondary structural elements follows the definition in the respective manuscripts (FOR006[3]: light blue, FOR005: marine blue, AL55[4]: dark blue).

Supplementary Table 1

	Fibril A (EMD-11031) (PDB 6Z10)	Fibril B (EMD-11030) (PDB 6Z1I)
Data collection and processing		
Magnification	130,000	130,000
Voltage (kV)	300	300
Electron exposure (e– Å^{-2})	1	1
Defocus range (μm)	0.2 – 4.2	0.2 – 4.2
Pixel size (Å)	1.04	1.04
Symmetry imposed	C1	C1
Initial particle images (no.)	194,502	194,502
Final particle images (no.)	11,003	12,122
Map resolution (Å)	3.2	3.4
FSC threshold (0.143)		
Rise (Å)	4.8	4.8
Twist	-1.1	-1.1
Pitch (nm)	155	155
Refinement		
Initial model used (PDB code)	De novo	PDB 6Z10
Model resolution (Å)		
FSC threshold 0.143	3.1	3.2
FSC threshold 0.5	3.4	3.5
Map CC (mask)	0.76	0.73
EMRinger ZScore	5.09	5.97
EMRinger Score	2.88	3.59
Model composition		
Non-hydrogen atoms	3,972	3,648
Protein residues	534	486
Ligands	0	0
B factors (Å^2)		
Protein	73.24	72.43
Ligand	-	-
R.m.s. deviations		
Bond lengths (Å)	0.009	0.009
Bond angles (°)	1.795	1.745
Validation		

MolProbity score	1.42	1.61
Clashscore	1.42	3.08
Poor rotamers (%)	0	0
Ramachandran plot		
Favored (%)	91.76	91.34
Allowed (%)	8.24	8.66
Disallowed (%)	0	0
B-factor after autosharpening (Å^2)	71.3	51.8
Contour level	6σ	6σ

Supplementary Table 1.

Reconstruction and modeling statistics.

Supplementary References

[1] Annamalai, K. et al. Common fibril structures imply systemically conserved protein misfolding pathways in vivo. *Angew Chem Int Ed* **56.26,** 7510-7514 (2017)

[2] Blech, M. et al. Molecular structure of human GM-CSF in complex with a disease-associated anti-human GM-CSF autoantibody and its potential biological implications. *Biochem J* **447.2,** 205-215 (2012)

[3] Radamaker, L., et al. Cryo-EM structure of a light chain-derived amyloid fibril from a patient with systemic AL amyloidosis. *Nat Commun* **10.1,** 1-8 (2019)

[4] Swuec, P., et al. Cryo-EM structure of cardiac amyloid fibrils from an immunoglobulin light chain AL amyloidosis patient. *Nat Commun* **10.1,** 1-9 (2019)

Publication III:

"Role of mutations and post-translational modifications in systemic AL amyloidosis studied by cryo-EM" Radamaker, L., Karimi-Farsijani, S., Andreotti, G., Baur, J., Neumann, M., Schreiner, S., Berghaus, N., Motika, R., Walther, P., Schmidt, V., Huhn, S., Hegenbart, U., Schönland, S.O., Wiese, S., Read, C., Schmidt, M. and Fändrich, M. *Manuscript accepted by Nature Communications.*

Published version: https://www.nature.com/articles/s41467-021-26553-9

Licensed under a Creative Commons Attribution 4.0 International License (CC BY 4.0), https://creativecommons.org/li

Contribution to publication III:

- Performed the research and analyzed the data presented in Fig. 3,5a,b; SI Fig. 2,3. Also Fig. 2, SI Fig. 1 in co-operation with Sara Karimi-Farsijani. SI Table 1 in co-operation with Sara Karimi-Farsijani and Matthias Schmidt.
- Writing and revising the manuscript in co-operation with Marcus Fändrich with contributions from all other co-authors.

Summary

In this publication the structure of an *IGLV1-51* derived LC amyloid fibril from patient FOR001 is presented. Tomograms of the cardiac amyloid deposits show that the amyloid fibrils impede the contractile function of the heart. The sequence of the fibril protein was obtained by mass spectrometry, which confirmed the disulfide bond and revealed a pyroglutamylation. As demonstrated by gel electrophoresis, the FOR001 fibril protein is glycosylated. By denaturing the amyloid fibrils and adding N-glycosidase, it was shown that both the glycosylated and deglycosylated fibril proteins form fibrils in vitro, however the glycosylated protein aggregated at a slower rate. By contrast, the glycosylated fibrils were more stable against proteolysis, indicating that glycosylation protects the amyloid fibrils from degradation.

Role of mutations and post-translational modifications

in systemic AL amyloidosis studied by cryo-EM

Lynn Radamaker[1], Sara Karimi-Farsijani[1], Giada Andreotti[1], Julian Baur[1], Matthias Neumann[2], Sarah Schreiner[3], Natalie Berghaus[3], Raoul Motika[4], Christian Haupt[1], Paul Walther[5], Volker Schmidt[2], Stefanie Huhn[3], Ute Hegenbart[6], Stefan O. Schönland[6], Sebastian Wiese[7], Clarissa Read[5,8], Matthias Schmidt[1], Marcus Fändrich[1]*

[1] Institute of Protein Biochemistry, Ulm University, 89081 Ulm, Germany.

[2] Institute of Stochastics, Ulm University, 89081 Ulm, Germany.

[3] Medical Department V, Section of Multiple Myeloma, Heidelberg University Hospital, 69120 Heidelberg, Germany.

[4] Department of Asia-Africa-Studies, Middle Eastern History and Culture, University of Hamburg, 20148 Hamburg, Germany.

[5] Central Facility for Electron Microscopy, Ulm University, 89081 Ulm, Germany.

[6] Medical Department V, Amyloidosis Center, Heidelberg University Hospital, 69120 Heidelberg, Germany.

[7] Core Unit Mass Spectrometry and Proteomics, Medical Faculty, Ulm University, 89081 Ulm, Germany.

[8] Institute of Virology, Ulm University Medical Center, 89081 Ulm, Germany.

* Corresponding author

Abstract

Systemic AL amyloidosis is a rare disease that is caused by the misfolding of immunoglobulin light chains (LCs). Potential drivers of amyloid formation in this disease are posttranslational modifications (PTMs) and the mutational changes that are inserted into the LCs by somatic hypermutation. Here we present the cryo electron microscopy (cryo-EM) structure of an ex vivo λ1-AL amyloid fibril whose deposits disrupt the ordered cardiomyocyte structure in the heart. The fibril protein contains six mutational changes compared to the germ line and three PTMs (disulfide bond, N-glycosylation and pyroglutamylation). Our data imply that the disulfide bond, glycosylation and mutational changes contribute to determining the fibril protein fold and help to generate a fibril morphology that is able to withstand proteolytic degradation inside the body.

Introduction

Systemic AL amyloidosis is defined by the formation of amyloid fibrils by immunoglobulin light chains (LC)[1,2]. These fibrils can deposit at multiple sites in the body where they can lead to severe impairment of vital organ functions. Untreated patients with a prominent heart involvement show a high risk of death with a median survival of only seven months after their initial diagnosis[3,4]. Due to their natural function as part of B-cell receptors and antibodies, LCs are hypervariable proteins. This variability arises from the genetic recombination of variable (V), joining (J) and constant (C) gene segments that are encoded in the germ line (GL), somatic hypermutation and the junctional diversity at the V/J interface in the course of V/J recombination[5]. Altogether there are 63-71

functional V (34-38 V_κ and 29-33 V_λ), 9-10 J (5 J_κ and 4-5 J_λ) and 5-6 C (1 C_κ and 4-5 C_λ) segments encoded within the GL[6] of which *IGLV6-57*, *IGLV3-01*, *IGLV2-14* and *IGKV1-33* were found to be over-represented in systemic AL amyloidosis[7,8,9,10]. These findings and the fact that usage of *IGLV1-44* is associated with cardiac involvement[11] imply that the LC primary structure is a key determinant for the development of amyloidosis.

Further support for this view comes from observations that the mutational changes that are inserted into the LCs during somatic hypermutation affects the kinetics of amyloid fibril formation in vitro[1]. The effect of these mutations has frequently been attributed to alterations in the biophysical properties of the natively folded, globular LCs, such as to a decreased thermodynamic stability[12,13], to increased conformational dynamics[14,15,16] or to local structural changes in a key region of the protein[14,15,16]. In other cases it was suggested that the mutations may affect the formation of specific folding or misfolding intermediates[14,17] or the stability or structure of the resulting amyloid fibril[18,19]. Post-translational modifications (PTMs) may further modulate the effects of the inserted mutations. Several studies have shown that AL fibril proteins can contain PTMs like disulfide bonds[20,21,22,23], N-terminal pyroglutamate (Pyro-Glu) modifications[24,25] or glycosylations[26,27]. Glycosylation was found to be overrepresented in AL patients indicating that this PTM contributes to the pathogenesis in AL amyloidosis[26,28]. Yet, the mechanism by which glycosylation affects fibril formation or AL pathogenesis has so far remained unclear.

To shed light on the structural effects of PTMs and mutational changes on the fibril state, we have determined the structure of an AL amyloid fibril with cryo electron microscopy (cryo-EM), which is partially pyroglutamylated, N-glycosylated and modified by an intramolecular disulfide bond. The observed fibril structure is different from previously described, non-glycosylated AL amyloid fibrils[21,22,23], consistent with the patient-specific nature of this disease. The mutational changes are

clustered into two topological regions of natively folded variable LC domains, but dispersed throughout the fold of the fibril protein with no obvious structural preference.

Results

FOR001 amyloid fibrils are structurally rigid and disrupt the ordered architecture of the heart muscle

The presently analyzed fibrils were extracted from the heart tissue of patient FOR001, who suffered from advanced cardiac AL amyloidosis and underwent a heart transplantation at the age of 51 years. Analysis of sections of cardiac tissue with scanning electron microscopy (SEM) demonstrates that the fibrils form large-sized, extracellular amyloid deposits that infiltrate and disrupt the ordered structure of the cardiomyocytes (Fig. 1a,b). Using scanning transmission electron microscopy (STEM) we obtained tomograms of the three-dimensional (3D) structure of the cardiac amyloid deposits (Fig. 1b). The deposits are composed of haphazardly arranged fibrils that show a width of ~9 nm. Quantification of the fibril end-to-end distances and contour lengths allowed us to determine the fibril persistence length at 0.74 ± 0.08 μm and their bending rigidity at $3.1 \cdot 10^{-27} \pm 3 \cdot 10^{-28}$ N m^2 (Fig. 1c). The persistence length corresponds to values reported in the literature[29,30] for amyloid fibrils which vary between 16 nm and 18.5 μm, indicating that FOR001 amyloid fibrils and their deposits are structurally rigid. The fibrils in these deposits interact with the surfaces of adjacent cardiomyocytes, and these interactions occur mainly via the fibril tips (Fig. 1d), and only rarely via the fibril lateral surfaces. In some cases, we find deformations in the plasma membrane associated with the focal contact points of the fibrils (Fig. 1d). The fibrils impede the contractile function of the heart, suggesting that clearance of the amyloid may help to restore cardiac function. While there is evidence that the patient's health condition is also defined by circulating amyloid precursors in

the serum[31] our observations underpin the view that the amyloid deposits are damaging to the patient.

Cryo-EM structure of the FOR001 AL amyloid fibril

To investigate the structure of the extracted FOR001 AL fibrils, we imaged them using cryo-EM (Fig. 2a). The images show that approximately 75 % of the fibrils seen in the micrographs belong to one dominant morphology. This fibril morphology is defined by a width of ~9 nm, which agrees with the width measured by electron tomography (see above), and a crossover distance of ~55 nm, as measured from the recorded images. 3D reconstruction of the fibril images yielded a 3D map of the dominant morphology with a resolution of 3.1 Å (Supplementary Figure 1a, Supplementary Table 1), while the remaining minor morphologies could not be reconstructed. The rise and twist of the reconstructed fibril are 4.76 Å and -1.46°, the pitch is 117 nm (Supplementary Table 1). The fibril consists of a single protofilament (C1 symmetry, Fig. 2b,c). The fitted molecular model (Fig. 2d) has a model resolution of 3.1 Å, (Supplementary Table 1). Projections of its density onto the y-z-plane correspond well to the two-dimensional (2D) class averages (Supplementary Figure 1b). The handedness of the fibrils in this sample was determined by platinum side-shadowing, which showed a left-handed twist (Supplementary Figure 2). The ordered core of the fibril consists of two segments that extend from Ser9 to Thr52 and Ser68 to Thr108 (Fig. 2d). For residues Gln1 to Pro8, Asp53 to Lys67 and Val109 to Ser118, which are present in the fibril as shown by mass spectrometry (MS) (see below), no well-defined density could be discerned in our map, suggesting that they are structurally disordered. The fibril protein contains an intramolecular disulfide that connects residues Cys22 and Cys89 (Fig. 2d).

Chemical interactions stabilizing the fibril protein fold

Despite being dominated by β-sheet conformation, the fibril protein structure is profoundly different from the structure of a natively folded LC (Fig. 3a) and encompasses eleven parallel cross-β sheets (β1 to β11) that are formed by residues Val10 – Ala12, Pro14 – Ser21, Asn31 – Val34, Tyr37 – Gln39, Thr43 – Ala44, Pro45 – Glu51, Thr70 – Leu74, Ile76 – Gly78, Tyr88 – Cys89, Thr91 – Glu93, and Thr105 – Leu107 (Fig. 3a,b). The β-strands in these sheets interact in the direction of the fibril z-axis through backbone hydrogen bonds as well as through side chain interactions, including the stacking of aromatic and polar residues (Supplementary Figure 3a,b). The fibril protein fold is defined by buried electrostatic interactions, such as between Glu84 and Lys46 (Supplementary Figure 3c), and by several buried patches of hydrophobic residues, such as the one formed by residues Val10, Ala12, Val34 and Trp36 (Fig. 3c). The fibril quaternary structure is stabilized by an interlocking of the protomers in the direction of the z-axis that is caused by a 14 Å height change of the fibril protein backbone (Supplementary Figure 3d).

Primary structure of the FOR001 fibril protein

The FOR001 fibril protein sequence was determined with electrospray ionization MS (Supplementary Figure 4). DNA sequencing of bone-marrow-derived cDNA was also attempted but failed to produce a sequence that matched the sequence obtained by direct sequencing of the fibril protein. Three major fibril protein species were revealed by MS (Supplementary Figure 5a). Two of these could be assigned to the LC fragments Pyro-Glu1 to Ser118 and Ser2 to Ser118 (Supplementary Figure 5b), both containing a disulfide bond. The third species corresponds to the fragment containing residues Val3 to Ser118 and a disulfide bond, although alternative mass assignments are also possible for the recorded MS peak (Supplementary Figure 5b). These analyses reveal two PTMs: a disulfide bond and a pyroglutamylation (Supplementary Figure 5c) that affects only a fraction of the fibril proteins. The third PTM of the fibril protein is an ~2kDa N-

glycosylation, which is demonstrated by an electrophoretic band shift of the refolded FOR001 fibril protein upon addition of N-glycosidase but not with O-glycosidase (Supplementary Figure 5d). The carbohydrate can be seen as extra density within our 3D map that could not be assigned to the polypeptide chain (Fig. 2b,d, red star). It protrudes from residue Asn17, which forms part of the only canonical N-glycosylation site (Asn-Xaa-Thr/Ser) in the fibril protein sequence.

Identification of the GL segments and mutational changes

Comparisons of the FOR001 LC with known sequences of immunoglobulin LCs and their GL segments (see methods for details) revealed that the FOR001 fibril protein stems from the GL segment *IGLV1-51*02*. The GL precursors of the J and C segments could not be identified unambiguously. In case of the C segment the number of residues (8; Gly111 - Ser118) was too small to allow any GL assignment. In case of the J segment, *IGLJ2*01, IGLJ3*01* (which are identical) and *IGLJ3*02* are all possible precursors (*IGLJ3*02* differs from *IGLJ2*01* and *IGLJ3*01* only in the first residue, which is mutated in the FOR001 protein sequence), also precluding a unique GL assignment. The FOR001 sequence shows six mutational changes compared to the GL segments *IGLV1-51*02, IGLJ2*01, IGLJ3*01* and *IGLJ3*02*: Lys17Asn, Asn52Thr, Asn53Asp, Gly82Ala and Asp93Glu in the V segment and Xaa99Gly in the J segment (Fig. 4a,b, indigo). The mutation Lys17Asn inserts the glycosylation site. In addition, residues Leu97-Ala98 form the variable junction between the V and J segments that arises from genetic V/J recombination (Fig. 4a,b, green).

The location of the mutations in known fibril structures and in natively folded V_L domains

To identify the possible role of mutations in LC aggregation, we analyzed their position within the known fibril structures and natively folded LCs. We find that the majority of the mutations occur at solvent-exposed positions in the fibril, specifically in the FOR001 fibril. Five FOR001 mutations

(Lys17Asn, Asn52Thr, Gly82Ala, Asp93Glu and Xaa99Gly) are part of the ordered fibril core, the sixth mutation (Asn53Asp) affects a structurally disordered region (Fig. 4a,b). One residue (position 53 in the FOR001 fibril protein) is mutated in all known AL fibril structures (Fig. 4a,b) and was identified previously as a mutational hot spot in systemic AL amyloidosis[32]. It is located in the central disordered segments that are present in the FOR001, FOR005 and AL55 fibril structures (Fig. 4a), indicating that this residue does not substantially affect the fibril stability. 79 ± 21 % of the mutations of the four known AL amyloid fibrils reside within an ordered structural segment of the V_L domain (Supplementary Table 2). This value is identical, within error, to the percentage of residues forming the ordered fibril parts (77 ± 6 %), suggesting that the mutations are not preferentially located in the fibril core. However, mutations within the ordered part of the fibril protein are generally well-accommodated in the structure and can add specific interactions. In the FOR006 fibril, they enable the interactions between Arg25 (mutated from Ser) and Glu84 [21]; in the FOR001 fibril, between Ala82 (mutated from Gly) and Leu48.

In a next step we analyzed the position of the aggregation prone segments in the fibril structures. These segments were identified here based on their theoretic aggregation score[21,23]. The aggregation-prone segments (as defined by an aggregation score of 5) occur within the stable core of the FOR001 fibril and other known AL amyloid fibrils (Supplementary Figure 6a,b). By contrast, the structurally disordered regions of these fibrils typically show an aggregation score of 0 (Supplementary Figure 6b). The fibrils with an internal disordered segment (FOR001, FOR005 and AL55) share a conserved sequence motif (PDRFSGS) with low aggregation propensity that is N-terminally preceded by a highly aggregation prone segment (aggregation score 5, Supplementary Figure 6a,b). In the FOR006 fibril, which does not contain an internal disordered segment, the PDRFSGS motif is not preceded by a segment with an aggregation score of 5 (Supplementary

Figure 6a,b). These data suggest that mutations and aggregation prone segments help to define the specific fold of the observed fibril morphologies.

The mutations may additionally affect the native state, as they are found to be clustered into two regions of the globular V_L domains: One region is formed by the complementarity determining region (CDR) mutations around the lower right rim of the native fold when it is oriented as in Fig. 4c (blue spheres). This part of the structure is involved in forming the antigen binding site and includes the shared mutated residue (position 53 in FOR001). The second region is formed by the framework mutations in the upper part of the V_L domain (Fig. 4c, magenta spheres). Both clusters correlate with previously described mutational hot spots of AL fibril proteins[32]. Taken together with the observations above, we conclude that the mutational changes in AL patients preferentially affect two structural sites in the native protein state. In addition, they contribute interactions to support the formation of a specific fibril morphology.

Effect of the N-glycosylation on fibril formation

The glycosylation site is exposed on the fibril surface (Fig. 2d) and on the surface of a natively folded LC (Fig. 5a,b). In the native LC it is far away from the interface to the heavy chain (Fig. 5a) or to the second LC in an LC dimer (Fig. 5b). These observations indicate that the glycosylation does not strongly interfere with the ability of the FOR001 LC to assemble into antibodies or LC dimers. To investigate the influence of the glycosylation on fibril formation in vitro, we purified and refolded FOR001 fibril protein from the heart. The glycosylation was removed from a fraction of the refolded protein. Both the glycosylated and the deglycosylated protein variants were able to form fibrils in vitro, as indicated by time-resolved fibrillation measurements with the amyloid-binding dye thioflavin T (ThT) (Fig. 5c). The deglycosylated FOR001 fibril protein aggregated much faster under these conditions than the glycosylated fibril protein (Fig. 5c), demonstrating that

a glycosylation retards rather than accelerates fibril formation in vitro. We further investigated the proteolytic stability of the glycosylated and deglycosylated fibril samples (Fig. 5d). Both in vitro fibril samples are substantially less stable to proteolysis with proteinase K than the ex vivo fibrils, although the glycosylated in vitro fibrils seem slightly more stable to proteolysis than the deglycosylated in vitro fibrils (Fig. 5e).

Discussion

In this study we obtained the cryo-EM structure of a glycosylated λ1 AL amyloid fibril that was extracted from the heart tissue of patient FOR001. Adding this structure to the previously published ex vivo AL amyloid fibril structures[21,22,23], there are now four known ex vivo amyloid fibril structures from systemic AL amyloidosis. Each of these structures is different (Supplementary Figure 7). The observed differences include the precise position of the β-strands and disordered regions within the fibril protein sequence, the presence or absence of internal cavities, the topological arrangement of the secondary structural elements, the organization of the network of chemical interactions that stabilize the misfolded conformational state, and the involvement of PTMs. However, the fibrils share structural features such as a fibril core that is mainly derived from the LC V_L domain, the presence of an intramolecular disulfide bond, and the tertiary structures of the fibril proteins are substantially different from a natively folded LC.

In the FOR001 fibril we identified three PTMs: a disulfide bond (Fig. 2d, Fig. 3c), a Pyro-Glu modification that affects only a fraction of the fibril proteins (Supplementary Figure 4, Supplementary Figure 5a,b), and a carbohydrate moiety that is linked by N-glycosylation (Supplementary Figure 5d). The disulfide bond corresponds to the canonical disulfide of a natively

folded LC V_L domain[5]. It occurs in all previously described cryo-EM structures of ex vivo AL amyloid fibrils[21,22,23], where it connects two chain segments that present an orientation that is switched by 180° relative to the native state[21]. This disulfide has profound effects on the misfolding and on the fibril structure, as it restricts the conformational freedom of the fibril protein and leads to the requirement of a rotational switch around the disulfide bond as a key molecular event in the misfolding of amyloidogenic LCs[21].

Pyro-Glu residues were previously observed in some[24,25] but not all AL fibril proteins[21,22,23]. They also occur in N-terminally truncated Alzheimer's Aβ peptide[33] and may accelerate the fibrillation of this peptide in vitro[34]. In the FOR001 fibril, a significant fraction of the fibril protein lacks the Pyro-Glu modification (Supplementary Figure 4, Supplementary Figure 5a,b), and the modification affects a disordered region of the fibril structure (Fig. 3a). While we cannot exclude that Pryo-Glu can affect the rate of aggregation, there is, based on our data, no strong evidence to suggest that Pyro-Glu is a major driver for the generation of the specific fibril morphology observed in patient FOR001.

The third PTM is an N-glycosylation. The Asn-Xaa-Ser/Thr N-glycosylation motif occurs more frequently in AL LC sequences than in normal LCs[35,36], and glycosylated LCs are over-represented in systemic AL amyloidosis patients[27], which indicates that LC glycosylation is important for systemic AL amyloidosis. However, the biophysical basis of this effect remained obscure. Several studies demonstrated that glycosylation can stabilize the native fold of globular proteins[37,38], reduce the protein conformational dynamics[39], or increase the solubility of proteins[37,38], indicating that a glycosylation should render a protein less amyloidogenic. Indeed, deglycosylated FOR001 fibril protein aggregates faster than glycosylated protein, as demonstrated here by in vitro fibrillation measurements with ThT (Fig. 5c).

A potentially more important effect of glycosylation could be that it masks the amyloid deposits within the tissue, preventing their clearance by body-own mechanisms[40]. A similar amyloid masking effect is known for serum amyloid P component[41] that is also glycosylated. The carbohydrate of the FOR001 protein is located on the surface of the fibril structure (Fig. 2b,d) and of the natively folded LC, as indicated by analysis of the crystal structure of a homologous LC (Fig. 5a,b). Hence, the carbohydrate covers part of the surface of the fibrils or its biological precursors, consistent with a protective effect and with observations that glycosylated in vitro fibrils from FOR001 fibril protein might be slightly more stable to proteinase K digestion than in vitro formed fibrils from deglycosylated protein. However, both in vitro fibrils are much less stable to proteinase K digestion than the ex vivo FOR001 fibrils (Fig. 5d,e).

The most profound effect of glycosylation suggested by our data is that it helps to define the fibril protein fold in this patient. The fibril protein tertiary structure in the glycosylated λ1 fibril of FOR001 is significantly different from a previously described, non-glycosylated λ1 fibril[21]. The previous structure, and all known structures of non-glycosylated AL amyloid fibril, are defined by a juxtaposition of the N- and C-terminal ends of the fibril protein (Supplementary Figure 7). In the FOR001 fibril, which carries the glycosylation in the N-terminal end of the fibril protein, no such juxtaposition is observed and the N- and C-terminal ends of the polypeptide chain are spread apart in the tertiary structure. Hence, the glycosylation may help to favor the FOR001 fibril protein fold by preventing the association of the N- and C-terminal ends of the fibril protein.

Several previous observations have suggested that the fibril protein fold and the fibril morphology are crucial for the pathological process of an amyloid disease. Consistent fibril protein folds and fibril morphologies can be found in different patients or animals that are affected by the same

disease variant and allelic variant of the fibril precursor protein[42,43,44]. Different fibril protein structures or fibril morphologies are associated with different disease variants[44,45,46]. Ex vivo fibril morphologies are often different from fibrils formed in vitro from the same proteins[20,23,44,47,48,49] and more protease-stable than their in vitro formed counterparts[47,49]. In particular the latter observations led to the hypothesis that pathogenic amyloid fibril structures may have been selected inside the body by their high proteolytic resistance and ability to escape endogenous clearance systems[49,50]. The present observations further support this view as they imply that the disulfide formation, the glycosylation and the mutational changes inserted during somatic hypermutation helped to shape the specific fibril morphology that is associated with patient FOR001 and which shows a high protease stability (Fig. 5d,e).

In summary, we have shown that in AL amyloidosis fibril deposits can interfere with the physiological function of heart tissue by disrupting its ordered architecture. PTMs and the specific mutational changes that characterize amyloidogenic LCs facilitate the formation of patient-specific fibril morphologies that are able to survive under the otherwise hostile and proteolytic conditions inside the body. The resulting fibrils are thus able to accumulate, proliferate and cause damage to the surrounding tissue. The differences in the available cryo-EM structures of fibrils from AL amyloidosis patients underline the patient-specific nature of the disease and make clear the need for investigating AL fibril structures from many patient cases in order to identify common principles of AL amyloid formation.

Methods

Source of the fibril-containing tissue

The fibrils were extracted from the explanted heart of a male patient (FOR001), who suffered from systemic AL amyloidosis with cardiac involvement and underwent cardiac surgery at the age of 51 years. The underlying condition was a monoclonal gammopathy. The patient was treated within the heart transplant program of the University Hospital Heidelberg. The explanted heart tissue was stored at -80 °C. The study was approved by the ethical committees of the University of Heidelberg (123/2006) and of Ulm University (203/18). Informed consent was obtained from the patient for the analysis of the amyloid deposits.

Visualization of amyloid fibril deposits in heart tissue using STEM and SEM

Frozen pieces of FOR001 heart tissue (~1 mm^3) were fixed in a solution of 0.1 % (w/v) glutaraldehyde, 4 % (w/v) paraformaldehyde and 1 % (w/v) saccharose in 0.1 M sodium phosphate buffer (pH 7.3) over night at 4°C. The further sample preparation for STEM and SEM was based on a protocol from a previous publication[51]. In brief, the fixed tissue pieces were cut into ~ 200 µm slices with a scalpel and then high-pressure frozen with a Compact 01 high-pressure freezing device (Engineering Office M. Wohlwend) and freeze substituted in a medium consisting of 0.1 % (w/v) uranyl acetate, 0.2 % (w/v) osmium tetroxide and 5 % (v/v) water in acetone using an AFS2 freeze substitution device (Leica Microsystems) with which the temperature was raised from -90 °C to room temperature over a period of 19 h. Afterwards, the tissue pieces were embedded in epoxy resin (Sigma-Aldrich) starting with a mixture of 30 % (v/v) resin in acetone for 1 h followed by 60 % (v/v) resin in acetone for 3 h and 100 % resin overnight and polymerization in fresh 100 % resin by incubation at 60 °C for 48 h. For SEM imaging, 200 nm thin sections were cut from the polymerized samples using the ultramicrotome Ultracut (Leica Microsystems) equipped with a 45°

diamond knife (Diatome). Sections were mounted on glow discharged silicon wafers and stained with a 0.3 % (w/v) lead citrate solution in water for 1 min, washed with distilled water, dried and imaged in an Hitachi S-5200 field emission scanning electron microscope, detecting the secondary electron signal at 5 kV in analysis mode. For STEM, 300 nm thin sections were cut with a 45° diamond knife and processed in a similar way as described in a previous publication[52]. In brief, sections were mounted on copper grids with 200 parallel grid bars (Plano). After attachment of 15 nm colloidal gold fiducials (Aurion), sections were coated with carbon by electron beam evaporation in a Baf 300 (BalTec). Tomograms were acquired with a STEM JEM-2100F (JEOL) operated at 200 kV. Tilt series were acquired from -72° to +72° with a 1.5° increment using the bright-field detector. The pixel size was 1.395 nm. Tilt series were reconstructed to tomograms by weighted back projection using an emulated simultaneous iterative reconstruction technique-like filter (20 iterations) and segmentation of fibrils and cell membranes were performed with the IMOD software package[53], version 4.9.0.

Measurement of the persistence length

A total of 197 amyloid fibrils in heart tissue were traced in the STEM tomograms and were then available as polygonal chains. Based on this representation, the squared end-to-end distance R, i.e. the Cartesian plane distance between the starting and end points, and the contour length L; i.e. the sum of the length of all line segments of the polygonal chain, were computed for each fibril. The persistence length P of the fibrils was then determined by regression analysis using the formula

$$R^2 = 2PL\left(1 - \frac{P}{L}\left(1 - e^{\frac{-L}{P}}\right)\right) \quad (1)$$

according to Kollmer et al.[54] and using the curve fitting tool in Matlab (MATLAB 2019, The MathWorks). P is contained in the confidence interval from 0.66 µm to 0.81 µm in 95 % of all cases. The bending rigidity B is computed based on P according to the formula

$$B = k_B TP \quad (2)$$

where k_B and T denote the Boltzmann constant and the temperature (300 K), respectively[21,55].

Fibril extraction from FOR001 heart tissue

Fibrils were extracted from FOR001 heart tissue using a previously established protocol[56]. In brief, 250 mg heart tissue were diced with a scalpel and washed five times with Tris Calcium Buffer (TCB) [20 mM Tris, 138 mM NaCl, 2 mM $CaCl_2$, 0.1 % (w/v) NaN_3, pH 8.0]. Each washing step consisted of the addition of 0.5 mL of ice-cold TCB to the pellet, the homogenization of the tissue with a Kontes Pellet Pestle, and the separation of the tissue from the supernatant by centrifugation for 5 min at 3,100 x g and 4 °C, followed by the removal of the supernatant. The tissue pellet after the fifth washing step was resuspended in 1 mL TCB containing 5 mg/mL *Clostridium histolyticum* collagenase (Sigma-Aldrich) and one tablet cOmplete ethylenediaminetetraacetic acid (EDTA)-free protease inhibitor cocktail (Roche) per 7 mL TCB. After an overnight incubation of the digest at 37 °C in a horizontal orbital shaker (750 rpm) the sample was centrifuged for 30 min at 3,100 x g and 4 °C. The pellet was subjected to ten washing steps which were performed in the same manner as the TCB washing steps described above, except that 0.5 mL Tris EDTA buffer [20 mM Tris, 140 mM NaCl, 10 mM EDTA, 0.1 % (w/v) NaN_3, pH 8.0] was used instead of TCB. The pellet from the last wash was resuspended in 0.5 mL ice-cold distilled water, mixed with a pipette and centrifuged for 5 min at 3,100 x g and 4 °C. The fibril-containing supernatant was retained and the pellet was submitted to nine more cycles of resuspension in water and centrifugation. The supernatants were retained to check for the presence of fibrils.

Platinum side shadowing and TEM

The handedness of the fibrils was determined by platinum side shadowing and TEM. Formvar and carbon-coated 200 mesh copper grids (Plano) were glow discharged for 40 s at 40 mA using a PELCO easiGlow glow discharge cleaning system (Ted Pella). 15 µL of the fibril solution were

applied to the grid and incubated for 30 s at room temperature. The grid was blotted using filter paper (Whatman) to remove excess fluid. The grid was washed three times with 10 µL of distilled water and dried at room temperature. Platinum was evaporated at an angle of 30° onto the grid to form a 1-nm-thick layer by use of a Balzers BAF 300 coating device. Grids were imaged using a JEM-1400 TEM (JEOL) that was operated at an acceleration voltage of 120 kV. The images were recorded with an F216 camera (TVIPS).

Cryo-EM sample preparation and data collection

C-flat 1.2/1.3 400 mesh holey carbon-coated grids (Science Services) were glow discharged at 40 mA for 40 s using a PELCO easiGlow glow discharge cleaning system (Ted Pella). Conditions of grid preparation were optimized with the help of a Vitrobot Mark 3 (Thermo Fisher Scientific) and checked in a 200 kV JEM 2100F transmission electron microscope (JEOL) that was equipped with a DE12 detector (Direct Electron). The grids for data collection were prepared by application of 3.5 µL fibril solution to a grid, incubation for 30 s at >95 % humidity, both-side blotting using filter paper (Whatman), and plunging into liquid ethane (~103 K). The data set was recorded with a Titan Krios transmission electron microscope (Thermo Fisher Scientific) at 300 kV and applying a Gatan imaging filter with a 20 eV slit. The images were recorded with a K2-Summit detector (Gatan) in counting mode. The software SerialEM v3.7 was used for data collection. 3,033 micrographs were collected from a single grid. See Supplementary Table 1 for further details. Global fibril parameters, such as width and crossover distance, were measured using Fiji v1.52[57]. The proportion of fibrils showing the reconstructed morphology was determined by analyzing all fibrils (length at least 200 nm) in 100 micrographs.

Reconstruction of the 3D map

Motion correction and dose-weighting was carried out with MotionCor2 [58]. For predicting, refining and correction of the contrast transfer function, Gctf v1.06[59] was used. Helical reconstruction was performed using Relion 3.0 [60]. As a first step, 279,338 particles were picked manually with a box size of ~312 Å and an inter-box distance of 34.6 Å (~11 %). After a reference free 2D classification using 279 classes and a regularization value of T = 2 in the first run, another 2D classification was performed with 50 classes. 2D classes were selected based on the visibility of a z-axial repeat at ~4.8 Å and bad classes were excluded. An initial 3D model was generated using Relion's initial model job. To generate a better reference for 3D classification, fibrils with visible cross-overs were picked from 28 micrographs resulting in 244 particles. These particles were subjected to a 3D classification with the initial model as a reference. This treatment resulted in a map with fibril-like features. Using this map as a reference, the particle set selected from 2D classification was subjected to several rounds of 3D classification, 3D refinement and post-processing. The resolution of the resulting map was estimated to be 3.6 Å. To obtain a more homogeneous set of particles, fibrils were picked more selectively yielding 43,308 particles with a box size of ~270 Å. Using the previously obtained post-processed map as a reference (with adjusted box size), subsequent steps of 3D classification, 3D refinement and post-processing yielded a map at 3.4 Å resolution. All manually picked particles were retained in this reconstruction. Further improvement of map resolution was accomplished through Bayesian polishing, resulting in a final map resolution of 3.1 Å, based on the value of the FSC curve for two independently refined half-maps at 0.143. An estimated map sharpening B-factor of -67.383 $Å^2$ was applied. The map had a twist of -1.45566° and 4.76311 Å. These values agree with twist values calculated from the measured cross-over distances on the cryo-EM micrographs, and with the rise as measured from the micrograph power spectra.

Model building and refinement

The software Coot[61] v0.8.9 was used to manually build the protein model de novo. First, the 3D map was traced and a poly-L-Ala chain created representing the protein backbone. The residues of this chain were then mutated to the FOR001 fibril protein sequence as determined by MS. This initial model was then further improved by subsequent rounds of manual and automated refinement (phenix.real_space_refine)[62] as implemented in Phenix v1.16[63]. Non-crystallographic symmetry and secondary structure restraints were imposed. Model-based automated sharpening of the map (phenix.auto_sharpen)[63] yielded an improved map, which was used to further refine the model. The quality of the model was assessed using the MolProbity[64] generated validation report. modeling parameters are listed in Supplementary Table 1.

Protein sequence determination by electrospray ionization MS

2 µg refolded, lyophilized and glycosylated fibril protein was resuspended in 15 µL buffer [280 mM Tris/HCl pH 6.8, 9 % (w/v) sodium dodecyl sulfate (SDS), 33.3 % (w/v) glycerol, 100 mM dithiothreitol] and processed by denaturing protein gel electrophoresis. Afterwards, the gel band of the fibril protein was cut out and washed by a 10 min incubation in the respective protease buffer (see below), and subsequently, in a mixture of 50 % (v/v) protease buffer and 50 % (v/v) ACN for 10 min. These incubation steps were repeated twice, followed by vacuum drying. Dried gel slices were reduced with 5 mM dithiothreitol (AppliChem) in 50 mM ammonium bicarbonate pH 8.0 for 20 min at room temperature and subsequently alkylated with 55 mM iodoacetamide (Sigma-Aldrich) in 10 mM ammonium bicarbonate for 20 min at 37 °C. The gel slices were placed in five different protease solutions (trypsin in 50 mM ammonium bicarbonate, pH 8.0; LysC in 50 mM ammonium bicarbonate, pH 8.0; elastase in 50 mM Tris/HCl, pH 9.0; chymotrypsin in 50 mM Tris/HCl buffer, pH 8.0, 10 mM $CaCl_2$; pepsin 40 mM HCl, pH 1.5) Each protease was used at 0.33 ng/µL concentration and digestion was carried out overnight at 37 °C (except for chymotrypsin at

25 °C). Resulting peptides were released from the gel slices in two steps: the first step was to add 20 µL of a solution containing 50 % (v/v) ACN and 0.1 % (v/v) TFA; the second step was an incubation in an ultrasonic bath (Bandelin Sonorex Super 10P) at 100 % intensity for 10 min each. ACN was evaporated and samples were filled to 15 µL with 0.1 % TFA (v/v).

Samples were separated by liquid chromatography using a U3000 RSLCnano (Thermo Fisher Scientific) online coupled to the mass spectrometer with an Acclaim PepMap analytical column (75 µm x 500 mm, 2 µm, 100 Å pore size; Thermo Fisher Scientific) in combination with a C18 µ-precolumn (0.3 mm x 5 mm; PepMap, Dionex LC Packings; Thermo Fisher Scientific). First, samples were washed with 0.1 % (v/v) TFA for 5 min at a flow rate of 30 µL/min. Subsequent separation was carried out employing a flow rate of 250 nL/min using a gradient consisting of solvent A [0.1 % (v/v) formic acid] and solvent B [86 % (v/v) ACN, 0.1 % (v/v) formic acid]. The main column was initially equilibrated in a mixture containing 5 % (v/v) solvent B and 95 % (v/v) solvent A. For elution, the percentage of solvent B was raised from 5 to 15 % over a period of 10 min, followed by an increase from 15 to 40 % over 20 min. Fractions from the main column directly eluted into the ionization module and were further analyzed by MS.

Samples were measured using an LTQ Orbitrap Velos Pro system (Thermo Fisher Scientific). The mass spectrometer was equipped with a nanoelectrospray ion source and distal coated SilicaTips (FS360-20-10-D, New Objective). The instrument was externally calibrated using standard compounds (LTQ Velos ESI Positive Ion Calibration Solution, Pierce, Thermo Scientific). The system was operated using the following parameters: spray voltage, 1.5 kV; capillary temperature, 250 °C; S-Lens radio frequency level, 68.9 %. The software XCalibur 2.2 SP1.48 (Thermo Fisher Scientific) was used for data-dependent MS/MS analyses. Full scans ranging from mass to charge ratio (m/z) 370 to 1,700 were acquired in the Orbitrap at a resolution of 30,000 (at m/z 400) with

automatic gain control enabled and set to 10^6 ions and a maximum fill time of 500 ms. Collision induced dissociation was employed as the fragmentation method on individual sample sets. Per survey scan, 10 ions were selected. Single charged ions were rejected and the m/z peaks of fragmented single charged ions were excluded from fragmentation for 60 s. In the linear ion trap, the automatic gain control was set to 10,000 ions and a maximum fill time of 100 ms. For MS/MS fragmentation, a normalized collision energy of 35 % with an 'activation q' of 0.25 and an activation time of 30 ms was used. The resulting fragments were analyzed using the linear ion trap part at rapid scan speeds. Subsequent detection of fragmentation spectra was performed in the Orbitrap mass analyzer at a resolution of 7,500.

For de novo sequencing, the Peaks AB Software (Bioinformatics Solutions) was used. The resulting sequence was then used as a target for further analyses using the Peaks X software suite (Bioinformatics Solutions) in order to confirm the de novo sequence. For all analyses, the mass accuracy was set to 10 ppm on intact peptide masses and 0.5 Da. Various PTMs were considered including the deamidation of Asn or Gln residues, pyroglutamate modifications (Gln), oxidation of Met, as well as carbamidomethylated Cys as a result of the alkylation. Ile/Leu as well as Gln/Lys have the same molecular weights and could not be uniquely determined. These residues were assigned based on homology considerations.

MS analysis of the total fibril protein mass

Lyophilized FOR001 fibril protein was resuspended in glycoprotein denaturing buffer (New England Biolabs) and subsequently it was deglycosylated without the heating step of the standard protocol. The deglycosylated protein was diluted with 0.1 % TFA (v/v) to obtain a concentration of 66 µg/mL. It was applied with a flow rate of 10 µl/min onto a PepSwift trap column (200 µm x 5 mm; Thermo Fisher Scientific) in combination with a monolithic ProSwift RP-4H analytical

column (100 µm x 50 cm; Thermo Fisher Scientific) which were connected to a U3000 RSLCnano (Thermo Fisher Scientific) that was coupled to the mass spectrometer. The fibril protein was eluted using a gradient of solvent B [86 % (v/v) ACN, 0.1 % (v/v) formic acid] and solvent A [0.1 % (v/v) formic acid] with a flow rate of 1 µL/min. The gradient started with an increase of 5 to 55 % solvent B over a period of 75 min, followed by an increase from 55 to 95 % over 15 min. The concentration of 95 % solvent B stayed constant for 3 minutes with a subsequent reduction from 95 to 5 % solvent B over 9 minutes. Fractions from the ProSwift RP-4H analytical column directly eluted into the ionization module and were further analyzed by MS. Samples were measured using an LTQ Orbitrap Elite system (Thermo Fisher Scientific). The mass spectrometer was equipped with a nanoelectrospray ion source and distal coated SilicaTips (FS360-20-10-D, New Objective). The instrument was externally calibrated using standard compounds (LTQ Velos ESI Positive Ion Calibration Solution, Pierce, Thermo Scientific) and operated using the following parameters: spray voltage, 1.5 kV; capillary temperature, 250 °C; S-Lens radio frequency level, 68.9 %. The software XCalibur 2.2 SP1.48 (Thermo Fisher Scientific) was used for data-dependent MS/MS analyses. Full scans ranging from mass to charge ratio (m/z) 370 to 1,700 were acquired in the Orbitrap at a resolution of 30,000 (at m/z 400) with automatic gain control enabled and set to 10^6 ions and a maximum fill time of 500 ms. The raw data was deconvoluted by the MASH Explorer[65] using default settings and the Quick Deconvolution feature. All calculated monoisotopic masses with a score equal or above 94 % resulting from initial m/z peaks with 5 charges or more were considered as correct and are shown in Supplementary Figure 5b,c. The deconvoluted mass peaks were further assigned to protein species by using the software mMass[66] considering a tolerance of 0.1 Da and a peak charge of 0. Sequence modifications were set as follows: pyroglutamylation at Gln1 was set as variable, whereas the disulfide bond between Cys22 and Cys89 was set as fixed.

Refolding of the FOR001 fibril protein

Solid guanidine hydrochloride was added to a sample of ex vivo FOR001 fibrils to reach a final concentration of 6 M followed by an overnight incubation at room temperature to disaggregate the fibrils. The protein was refolded by dialysis (molecular weight cut-off 3.5 kDa, Spectra/Por 6 Dialysis Membrane Pre-wetted RC Tubing, Spectrum Labs) against 20 mM Tris buffer, pH 8.0, for 24 h at 4 °C. The protein was purified by anion exchange chromatography with Q-SepharoseFF medium (10 mL, Cytiva) in an XK 16/20 column (Cytiva) with a slope gradient from 0 % to 100 % elution buffer [20 mM Tris buffer, 1 M NaCl, pH 8.0] over 20 column volumes (CVs). The fibril protein-containing fractions, as identified by protein gel electrophoresis, were purified further with a Resource 15 RPC column (3 mL, Cytiva) that was equilibrated in solvent A [0.1 % (v/v) trifluoroacetic acid (TFA) in water]. The protein was eluted through a slope gradient from 0 to 58 % solvent B [86 % (v/v) acetonitrile (ACN), 0.1 % (v/v) TFA] over 20 CVs, followed by second gradient from 58 to 100 % solvent B over 4 CVs to remove other bound proteins. Fractions were collected and the fractions containing the FOR001 fibril protein were identified by protein gel electrophoresis, pooled and lyophilized.

Deglycosylation of the refolded FOR001 fibril protein

For the experiment shown in Supplementary Figure 5a, the lyophilized, refolded FOR001 fibril protein was dissolved in water at approximately 2 mg/mL concentration. The exact protein concentration was determined by the intrinsic protein absorbance at 280 nm. This solution was mixed with water and SDS-containing 10 x glycoprotein denaturing buffer [5 % (w/v) SDS, 400 mM dithiolthreitol] (New England Biolabs) to generate a final FOR001 fibril protein solution with the volume V_{Prot} containing a protein concentration of 1 mg/mL and 1 x glycoprotein denaturing buffer. The protein was heated for 10 min at 100°C to partially denature the protein before it was cooled to room temperature. For N-deglycosylation, the heated sample was mixed with 1/5 V_{Prot} of a

10 % (v/v) solution of the detergent Nonident P40 in water (New England Biolabs), 1/5 V_{Prot} 10 x Glycobuffer 2 [500 mM sodium phosphate, pH 7.5] (New England Biolabs), 1/2 V_{Prot} water, and 1/10 V_{Prot} PNGase F in 20 mM Tris/HCl, 50 mM NaCl, 5 mM EDTA, pH 7.5 (New England Biolabs) and incubated for 1 h at 37°C. For O-deglycosylation, the heated sample was mixed with 1/5 V_{Prot} of a 10 % (v/v) Nonident P40 solution (New England Biolabs), 1/5 V_{Prot} 10 x Glycobuffer 2 (New England Biolabs), 3/10 V_{Prot} water, 1/10 V_{Prot} O-glycosidase in 20 mM Tris/HCl, 50 mM NaCl, 1 mM EDTA, pH 7.5 (New England Biolabs) and 1/5 V_{Prot} neuraminidase in 20 mM Tris/HCl, 50 mM NaCl, 5 mM EDTA, pH 7.5 (New England Biolabs) and incubated for 10 min at 37°C. The deglycosylation was checked by denaturing protein gel electrophoresis. N- and O-glycosylated fetuin protein, which we purchased as a 10 mg/mL solution from New England Biolabs, was used as a control substance. For the experiments reported in Figure 5, the lyophilized, refolded FOR001 protein was dissolved in water at 1 mg/mL concentration and denatured - without SDS and dithiothreitol - for 10 min at 100°C, as the SDS in the denaturing buffer was found to interfere with the subsequent reversed phase chromatography.

Protein concentration measurement based on the intrinsic absorbance at 280 nm

40 µL protein solution were mixed with 160 µL 7.5 M guanidine hydrochloride (Carl Roth) in 25 mM sodium phosphate buffer, pH 6.5. The absorbance was measured at 280 nm in a Lambda Bio+ ultraviolett/visible (PerkinElmer) spectrometer using a Quartz Suprasil R Ultra-Micro cuvette (Hellma). The protein concentration was determined based on the Lambert-Beer law using a theoretic molar extinction coefficient of 16,740 M^{-1} cm^{-1} for the FOR001 fibril protein according to the method of Gill and von Hippel[67].

Fibril formation kinetics measurements using ThT

Refolded and lyophilized FOR001 fibril protein (glycoslylated or deglycosylated) was dissolved at 2 mg/mL concentration in water. Aggregation kinetics measurements were set up in PF 96-well F-bottom black microplates (Greiner Bio-One International). Each well was filled with 100 µL sample, containing 0.4 mg/mL glycosylated or deglycosylated fibril protein, 20 µM ThT and 10 mM sodium acetate, 10 mM boric acid, 10 mM sodium citrate, pH 4.0, and 150 mM NaCl. The plates were sealed with Rotilabo-sealing film (Carl Roth) and incubated at 37°C in FLUOstar Omega (BMG Labtech) for 72 h. During incubation the plates were agitated by orbital shaking at 300 rpm, which was paused during measurement. The fluorescence emission intensity at 490 nm was recorded every 30 min upon excitation at 450 nm.

Proteinase K digestion of amyloid fibrils

Aliquots of solutions containing ex vivo FOR001 amyloid fibrils or in vitro formed fibrils from glycosylated or deglycosylated FOR001 fibril protein (from the ThT kinetic experiment) were mixed with water and a 10 x buffer stock [200 mM Tris, pH 8.0, 1.4 M NaCl, 20 mM $CaCl_2$, 1 % (w/v) NaN_3] to reach a total volume of 60 µL containing 0.2 mg/mL protein in 1 x buffer. A first aliquot (10 µL) was withdrawn from this solution and retained for gel electrophoresis as the control sample without protease. The remaining 50 µL of the protein solution were mixed with 1 µL of a 2 mg/mL proteinase K solution (Thermo Fisher Scientific). Immediately afterwards, a second aliquot (10 µL) was removed (0 min sample). The remaining solution was incubated at 37 °C in a heating block and further aliquots (10 µL) were withdrawn after 1 min, 2 min and 5 min. As soon as an aliquot was withdrawn it was mixed with 1 µL 200 mM phenylmethylsulfonyl fluoride (PMSF) (Carl Roth) in methanol, incubated for 1 min at room temperature and flash frozen in liquid nitrogen. After the experiment, all aliquots were brought to room temperature and analyzed by denaturing protein gel electrophoresis. The resulting protein bands (72x150 pixels) were

densitometrically quantified using the program Fiji v1.52[57]. The intensity of the fibril protein band without proteinase K was set to 100 %, and an equally sized area on the gel without protein at 0 %.

Denaturing protein gel electrophoresis

Samples from the deglycosylation experiment and proteolytic stability measurement (10 µL volume for degclycosylation, 11 µL volume for proteolytic stability including 1 µL PMSF) were mixed with 2 µL 10 x NuPAGE reducing agent (Thermo Fisher Scientific), 5 µL 4 x NuPAGE LDS sample buffer (Thermo Fisher Scientific) and water to generate a sample with a total volume of 20 µL. The solution was heated at 95ºC for 10 min and applied onto a 4-12 % NuPAGE Bis-Tris gel (Thermo Fisher Scientific), operated in NuPAGE MES SDS running buffer (Thermo Fisher Scientific). BlueEasy Prestained (Genetics) was used as a marker. The gel was stained in a solution containing 30 % (v/v) ethanol, 10 % (v/v) acetic acid and 0.25 % (w/v) Coomassie brilliant blue and destained with a solution containing 20 % (v/v) ethanol and 10 % (v/v) acetic acid.

Analysis of GL segments and mutations

The FOR001 amino acid sequence was used to search the IgBLAST database (https://www.ncbi.nlm.nih.gov/igblast/), which returned the GL segment *IGLV1-51*02*. The protein sequence of the GL segment was retrieved from the VBase2 database (http://www.vbase2.org/). The FOR001 J segment was compared to the five functional *IGLJ* GL segments in the GenBank database (https://www.ncbi.nlm.nih.gov/genbank/). It matched both *IGLJ2* (Gene ID: 28832) and *IGLJ3* (GeneID: 28831) and no unique source could be determined. Nor could we identify the GL precursor of the C segment as most of the LC C_L domain is missing in the FOR001 fibril protein. The residues Leu97-Ala98 constitute the variable V/J junctional region. CDRs were determined with abYsis (http://www.abysis.org/abysis/) based on the Kabat definition[68]. In this manuscript, all mutations are represented in the direction GL to fibril protein.

Computation of the aggregation score

To compute the aggregation score we used TANGO version 2.1 [69], WALTZ[70], FoldAmyloid[71], Aggrescan[72], and PASTA2.0 [73]. These programs calculate a residue-specific aggregation potential. The following settings were chosen for each program: TANGO: temperature: 309.15 K, ionic strength: 0.02 M, concentration: 1 M and pH 7.0; WALTZ: the threshold was set to high sensitivity and the pH to 7.0; FoldAmyloid: scale: triple hybrid, averaging frame: 5; Aggrescan: default settings; PASTA: 90 % specificity, top pairing energies: 22. Residues with a high aggregation potential are defined as follows: TANGO: β-sheet aggregation values above 0.0; WALTZ: total sequence score above 0.0; Foldamyloid: five successive amino acids with a triple hybrid threshold above 0.062; Aggrescan: aggregation-propensity values above −0.02; PASTA: PASTA Energy Units below −2.8. An aggregation score of 0 means that none of the programs identifies a high aggregation score for a given residue. An aggregation score of 5 means that all five programs predict a high aggregation score for that residue.

Protein structure representation

The images of the density map and protein model were created with the software UCSF Chimera v1.14[74]. Hydrogen bonds were defined according to the criteria of both UCSF Chimera v.1.14[74] and the software Coot v0.8.9[61]. The β-sheets were defined as a minimum of two residues having φ/ψ angles in the β-sheet region of the Ramachandran plot and at least one backbone hydrogen bond.

Sample statistics

In this manuscript errors report the standard deviation. In Fig. 5e a one-tailed Welch t-test was used.

Data availability

The datasets used during the current study are available from public repositories and/or from the corresponding author on reasonable request. The cryo-EM map of the FOR001 fibrils was deposited in the Electron Microscopy Data Bank (https://www.ebi.ac.uk/pdbe/emdb/) with the accession code EMD-12570. The coordinates of the corresponding atomic model were deposited in the PDB (https://www.rcsb.org/) under the accession code 7NSL. The cryo-EM data of the FOR001 fibrils were deposited on EMPIAR (https://www.ebi.ac.uk/pdbe/emdb/empiar/) with the accession code EMPIAR-10730. The following published PDB structures were used in the manuscript: 4ODH 10.2210/pdb4ODH/pdb, 6IC3 10.2210/pdb6IC3/pdb, 6Z1O 10.2210/pdb6Z1O/pdb, 6HUD 10.2210/pdb6HUD/pdb, 5JZ7 10.2210/pdb5JZ7/pdb, 6QB6 10.2210/pdb6QB6/pdb, 6Q0E 10.2210/pdb6Q0E/pdb, 7JVA 10.2210/pdb7JVA/pdb, 5MUD 10.2210/pdb5MUD/pdb. The accession codes for the *IGLV1-51**02 segment from the IMGT database is M30446 http://www.imgt.org/ligmdb/view?id=M30446 and from the VBase2 humIGLV015 http://www.vbase2.org/vgene.php?id=humIGLV015. The *IGLJ2* and *IGLJ3* gene segments were taken from GenBank with the Gene IDs 28832 https://www.ncbi.nlm.nih.gov/gene/28832 and 28831 https://www.ncbi.nlm.nih.gov/gene/28831, respectively. Source data are provided with this paper for the following figures: Fig. 1c, Fig. 5c,d,e, Supplementary Figure 1a, Supplementary Figure 2, Supplementary Figure 5d and Supplementary Figure 6.

References

[1] Blancas-Mejia, L. M. et al. Immunoglobulin light chain amyloid aggregation. *Chemical Commununications* **54.76,** 10664-10674 (2018)

[2] Herrera, G.A., Teng, J., Turbat-Herrera, E.A., Zeng, C. and del Pozo-Yauner, L. Understanding Mesangial Pathobiology In AL-amyloidosis And Monoclonal Immunoglobulin Light Chain Deposition Disease. *Kidney international reports* (2020)

[3] Wechalekar, A. D. et al. A European collaborative study of treatment outcomes in 346 patients with cardiac stage III AL amyloidosis. *Blood* **121**, 3420–3427 (2013).

[4] Merlini, G. et al. Systemic immunoglobulin light chain amyloidosis. *Nature reviews Disease primers*, **4(1)**, 1-19 (2018)

[5] Janeway CA Jr, Travers P, Walport M, et al. Immunobiology: The Immune System in Health and Disease. 5th edition. New York: Garland Science;. The generation of diversity in immunoglobulins. (2001)

[6] Lefranc, M.P. IMGT®, the international ImMunoGeneTics database. *Nucleic Acids Research*, **29(1)**: 207-209 (2001).

[7] Comenzo, R.L., Zhang, Y., Martinez, C., Osman, K. and Herrera, G.A., The tropism of organ involvement in primary systemic amyloidosis: contributions of Ig VL germ line gene use and clonal plasma cell burden. *Blood* **98(3)**, 714-720 (2001)

[8] Perfetti, V. et al. Analysis of Vλ-Jλ expression in plasma cells from primary (AL) amyloidosis and normal bone marrow identifies 3r (λIII) as a new amyloid-associated germline gene segment. *Blood* **100(3),** 948-953 (2002)

[9] Abraham, R.S. et al. Immunoglobulin light chain variable (V) region genes influence clinical presentation and outcome in light chain–associated amyloidosis (AL). *Blood* **101(10),** 3801-3807 (2003)

[10] Kourelis, T.V. et al. Clarifying immunoglobulin gene usage in systemic and localized immunoglobulin light-chain amyloidosis by mass spectrometry. *Blood* **129(3),** 299-306 (2017)

[11] Perfetti, V. et al. The repertoire of lambda light chains causing predominant amyloid heart involvement and identification of a preferentially involved germline gene, IGLV1-44. *Blood* **119**, 144–150 (2012).

[12] Hurle, M.R., Helms, L.R., Li, L.I.N., Chan, W. and Wetzel, R. A role for destabilizing amino acid replacements in light-chain amyloidosis. *Proceedings of the National Academy of Sciences*, **91(12),** 5446-5450 (1994)

[13] J. Wall, M. Schell, C. Murphy, R. Hrncic, F.J. Stevens, A. Solomon. Thermodynamic instability of human lambda 6 light chains: Correlation with fibrillogenicity. *Biochemistry*, **38,** 14101-14108 (1999)

[14] Oberti, L. et al. Concurrent structural and biophysical traits link with immunoglobulin light chains amyloid propensity. *Scientific reports*, **7(1),** 1-11 (2017)

[15] Kazman, P. et al. Fatal amyloid formation in a patient's antibody light chain is caused by a single point mutation. *Elife*, **9,** e52300 (2020)

[16] Rottenaicher, G.J. et al. Molecular mechanism of amyloidogenic mutations in hypervariable regions of antibody light chains. *Journal of biological chemistry*, **296,** 100334.Y. (2021)

[17] Blancas-Mejía, L.M. et al. Kinetic control in protein folding for light chain amyloidosis and the differential effects of somatic mutations. *Journal of molecular biology*, **426(2),** 347-361 (2014)

[18] Piehl, D.W., Blancas-Mejía, L.M., Ramirez-Alvarado, M. and Rienstra, C.M. Solid-state NMR chemical shift assignments for AL-09 V L immunoglobulin light chain fibrils. *Biomolecular NMR assignments*, **11(1),** 45-50 (2017)

[19] Pradhan, T. et al. Seeded fibrils of the germline variant of human λ-III immunoglobulin light chain FOR005 have a similar core as patient fibrils with reduced stability. *Journal of Biological Chemistry*, **295(52),** 18474-18484 (2020)

[20] Annamalai, K., et al. Common fibril structures imply systemically conserved protein misfolding pathways in vivo. *Angewandte Chemie*, **129(26),** 7618-7622 (2017)

[21] Radamaker, L., et al. Cryo-EM structure of a light chain-derived amyloid fibril from a patient with systemic AL amyloidosis. *Nat. Comm.* **10.1,** 1-8 (2019)

[22] Swuec, P., et al. Cryo-EM structure of cardiac amyloid fibrils from an immunoglobulin light chain AL amyloidosis patient. *Nat. Comm.* **10.1,** 1-9 (2019)

[23] Radamaker, L., et al. Cryo-EM reveals structural breaks in a patient-derived amyloid fibril from systemic AL amyloidosis. *Nature communications*, **12(1),** 1-10 (2021)

[24] Yazaki, M., Liepnieks, J.J., Callaghan, J., Connolly, C.E. and Benson, M.D. Chemical characterization of a lambda I amyloid protein isolated from formalin-fixed and paraffin-embedded tissue sections. *Amyloid*, **11(1),** 50-55 (2004)

[25] Lu, Y., Jiang, Y., Prokaeva, T., Connors, L.H. and Costello, C.E. Oxidative post-translational modifications of an amyloidogenic immunoglobulin light chain protein. *International journal of mass spectrometry*, **416,** 71-79 (2017)

[26] Kumar, S, et al. Assay to rapidly screen for immunoglobulin light chain glycosylation: a potential path to earlier AL diagnosis for a subset of patients. *Leukemia*, **33(1),** 254-257 (2019)

[27] Mellors, P.W., et al. MASS-FIX for the detection of monoclonal proteins and light chain N-glycosylation in routine clinical practice: a cross-sectional study of 6315 patients. *Blood Cancer Journal*, **11(3),** 1-9 (2021)

[28] Dispenzieri, A., et al. N-glycosylation of monoclonal light chains on routine MASS-FIX testing is a risk factor for MGUS progression. *Leukemia*, **34(10),** 2749-2753 (2020)

[29] Sagis, L.M., Veerman, C. and van der Linden, E. Mesoscopic properties of semiflexible amyloid fibrils. *Langmuir*, **20(3),** 924-927 (2004)

[30] Adamcik, J. and Mezzenga, R. Study of amyloid fibrils via atomic force microscopy. *Current Opinion in Colloid & Interface Science*, **17(6),** 369-376 (2012)

[31] Palladini, G., et al. Circulating amyloidogenic free light chains and serum N-terminal natriuretic peptide type B decrease simultaneously in association with improvement of survival in AL. *Blood*, **107(10),** 3854-3858 (2006)

[32] Poshusta, T.L., et al. Mutations in specific structural regions of immunoglobulin light chains are associated with free light chain levels in patients with AL amyloidosis. *PloS one*, **4(4),** e5169 (2009)

[33] Thal, D.R., Walter, J., Saido, T.C. and Fändrich, M. Neuropathology and biochemistry of Aβ and its aggregates in Alzheimer's disease. *Acta neuropathologica*, **129(2),** 167-182 (2015)

[34] Wulff, M., et al. Enhanced Fibril Fragmentation of N-Terminally Truncated and Pyroglutamyl-Modified Aβ Peptides. *Angewandte Chemie International Edition*, **55(16),** 5081-5084 (2016)

[35] Stevens, F. J. Four structural risk factors identify most fibril-forming kappa light chains. *Amyloid* **7(3),** 200-211 (2000)

[36] Omtvedt, L.A., et al. Glycosylation of immunoglobulin light chains associated with amyloidosis. *Amyloid* **7(4),** 227-44 (2000)

[37] Solá, R.J. and Griebenow, K.A.I. Effects of glycosylation on the stability of protein pharmaceuticals. *Journal of pharmaceutical sciences*, **98(4),** 1223-1245 (2009)

[38] Schwarz, F. and Aebi, M. Mechanisms and principles of N-linked protein glycosylation. *Current opinion in structural biology*, **21(5),** 576-582 (2011)

[39] Lee, H.S., Qi, Y. and Im, W. Effects of N-glycosylation on protein conformation and dynamics: Protein Data Bank analysis and molecular dynamics simulation study. *Scientific reports*, **5(1),** 1-7 (2015)

[40] Bellotti, V., Mangione, P. and Merlini, G. immunoglobulin light chain amyloidosis—the archetype of structural and pathogenic variability. *Journal of structural biology*, **130(2-3),** 280-289 (2000)

[41] Pepys, M.B., et al. Human serum amyloid P component is an invariant constituent of amyloid deposits and has a uniquely homogeneous glycostructure. *Proceedings of the National Academy of Sciences*, **91(12),** 5602-5606 (1994)

[42] Liberta, F., et al. Morphological and primary structural consistency of fibrils from different AA patients (common variant). *Amyloid*, **26(3),** 164-170 (2019)

[43] Schmidt, M., et al. Cryo-EM structure of a transthyretin-derived amyloid fibril from a patient with hereditary ATTR amyloidosis. *Nature communications*, **10(1),** 1-9 (2019)

[44] Scheres, S.H., Zhang, W., Falcon, B. and Goedert, M. Cryo-EM structures of tau filaments. *Current Opinion in Structural Biology*, **64,** 17-25 (2020)

[45] Bergström, J., et al. Amyloid deposits in transthyretin derived amyloidosis: cleaved transthyretin is associated with distinct amyloid morphology. *The Journal of Pathology: A Journal of the Pathological Society of Great Britain and Ireland* **206(2),** 224-232 (2005)

[46] Westermark, G.T., Fändrich, M. and Westermark, P.,. AA amyloidosis: pathogenesis and targeted therapy. *Annual Review of Pathology: Mechanisms of Disease*, **10,** 321-344 (2015)

[47] Kollmer, M., et al. Cryo-EM structure and polymorphism of Aβ amyloid fibrils purified from Alzheimer's brain tissue. *Nature communications*, **10(1),** 1-8 (2019)

[48] Schweighauser, M., et al. Structures of α-synuclein filaments from multiple system atrophy. *Nature* **585,** 464–469 (2020)

[49] Bansal, A., et al. AA amyloid fibrils from diseased tissue are structurally different from in vitro formed SAA fibrils. *Nature communications*, **12(1),** 1-9 (2021)

[50] Fändrich, M. and Schmidt, M. Methods to study the structure of misfolded protein states in systemic amyloidosis. *Biochemical Society Transactions*, **49(2),** 977-985 (2021)

[51] Read, C., Walther, P., von Einem, J. Quantitative Electron Microscopy to Study HCMV Morphogenesis, in: Yurochko, A.D. (Ed.), Human Cytomegaloviruses: Methods and Protocols, Methods in Molecular Biology. Springer US, New York, NY, 265–289 (2021)

[52] Read, C., Schauflinger, M., Nikolaenko, D., Walther, P., Einem, J. von. Regulation of human cytomegalovirus secondary envelopment by a C-terminal tetra-lysine motif in pUL71. *J. Virology* JVI.02244-18. (2019)

[53] Kremer, J.R., Mastronarde, D.N., McIntosh, J.R. Computer visualization of three-dimensional image data using IMOD. *Jounal of structural biology* **116,** 71–76 (1996)

[54] Kollmer, M., et al. Electron tomography reveals the fibril structure and lipid interactions in amyloid deposits. *Proceedings of the National Academy of Sciences*, **113(20),** 5604-5609 (2016)

[55] Feuz, L., Leermakers, F. A. M., Textor, M., Borisov. O. Bending rigidity and induced persistence length of molecular bottle brushes: a self-consistent-field theory. *Macromolecules* **38,** 8891-8901 (2005)

[56] Annamalai, K., et al. Polymorphism of amyloid fibrils in vivo. *Angewandte Chemie International edition* **55.15**, 4822–4825 (2016).

[57] Schindelin, J. et al. Fiji: an open-source platform for biological-image analysis. *Nature methods*, **9(7),** 676–682. (2012)

[58] Zheng, S. Q. et al. MotionCor2: anisotropic correction of beam-induced motion for improved cryo-electron microscopy. *Nature methods* **14**, 331–332 (2017)

[59] Zhang, K. Gctf: Real-time CTF determination and correction. *Journal of structural biology* **193**, 1–12 (2016)

[60] He, S., Scheres, S. H. W. Helical reconstruction in RELION. *Journal of structural biology* **198**, 163–176 (2017)

[61] Emsley P., Lohkamp, B., Scott, W.G. & Cowtan, K.. Features and Development of Coot. *Acta Crystallography D Biology Crystallography* **66**, 486–501 (2010)

[62] Afonine, P.V. et al. Real-space refinement in PHENIX for cryo-EM and crystallography. *Acta Crystallography D Structural Biology* **74**, 531-544 (2018)

[63] Afonine, P.V. et al. New tools for the analysis and validation of cryo-EM maps and atomic models. *Acta Crystallography D Structural Biology* **74**, 814-840 (2018)

[64] Williams, C. J. et al. MolProbity: More and better reference data for improved all atom structure validation. *Protein Science* **27.1,** 293-315 (2018)

[65] Wu, Z., Roberts, D.S., Melby, J.A., Wenger, K., Wetzel, M., Gu, Y., Ramanathan, S.G., Bayne, E.F., Liu, X., Sun, R. and Ong, I.M. MASH Explorer: A Universal Software Environment for Top-Down Proteomics. *Journal of proteome research*, **19(9),** 3867-3876 (2020)

[66] Niedermeyer, T.H. and Strohalm, M. mMass as a software tool for the annotation of cyclic peptide tandem mass spectra. *PloS one*, **7(9),** e44913 (2012)

[67] Gill, S.C. and Von Hippel, P.H. Calculation of protein extinction coefficients from amino acid sequence data. *Analytical biochemistry*, **182(2),** 319-326 (1989)

[68] Kabat. E. A., Wu, T. T., Reid-Miller, M., Peny, H. & Gottesman, K. United States Department of Health and Human Services, Wash-. Sequences of Proteins of Immunological Interest. 4th Ed. ington, D.C. (1987)

[69] Fernandez-Escamilla, A. M., Rousseau, F., Schymkowitz, J. & Serrano, L. Prediction of sequence-dependent and mutational effects on the aggregation of peptides and proteins. *Nature Biotechnology* **22**, 1302–1306 (2004).

[70] Maurer-Stroh, S. et al. Exploring the sequence determinants of amyloid structure using position-specific scoring matrices. *Nature methods*, **7(3),** 237-242 (2010)

[71] Garbuzynskiy, S. O., Lobanov, M. Y. & Galzitskaya, O. V. FoldAmyloid: a method of prediction of amyloidogenic regions from protein sequence. *Bioinformatics* **26**, 326–332 (2010)

[72] Conchillo-Solé, O. et al. AGGRESCAN: a server for the prediction and evaluation of “hot spots” of aggregation in polypeptides. *BMC Bioinformatics* **8**, 65 (2007).

[73] Walsh, I., Seno, F., Tosatto, S. C. & Trovato, A. PASTA 2.0: an improved server for protein aggregation prediction. *Nucleic Acids Res.* **42**, W301–W307 (2014).

[74] Pettersen, E. F. et al. UCSF Chimera—a visualization system for exploratory research and analysis. *Journal of Computational Chemistry* 25, 1605–1612 (2004)

Acknowledgements

We thank the Deutsche Forschungsgemeinschaft for funding (projects FA 456/23 and FA 456/27 to M.F., HA 7138/3 to C.H., HE 8472/1-1 to U.H., HU 2400/1-1 to S.H., SCHO 1364/2-1 to S. O. S., SCHM 997/30-1 to V.S and a Start-up Grant of the Research Unit FOR 2969 to C.R.). All cryo-EM data were collected at the European Molecular Biology Laboratory, Heidelberg (Germany), funded by iNEXT (Horizon 2020, European Union). We are grateful to Karl-Heinz Gührs for critically reading the manuscript.

Author contributions

L.R., S.K, G.A., J.B. S.W. and C.R. carried out experiments. L.R, S.K. G.A., J.B., M.N., S.S., N.B., C.H., V.S., S.H., P.W., S.W., C.R., M.S. and M.F. analyzed data. R.M., U.H. and S.O.S. contributed tools, reagents or materials. M.F. designed research. L.R. and M.F. wrote the paper with contributions from all other authors.

Competing interests

The authors declare no competing interests.

Figures

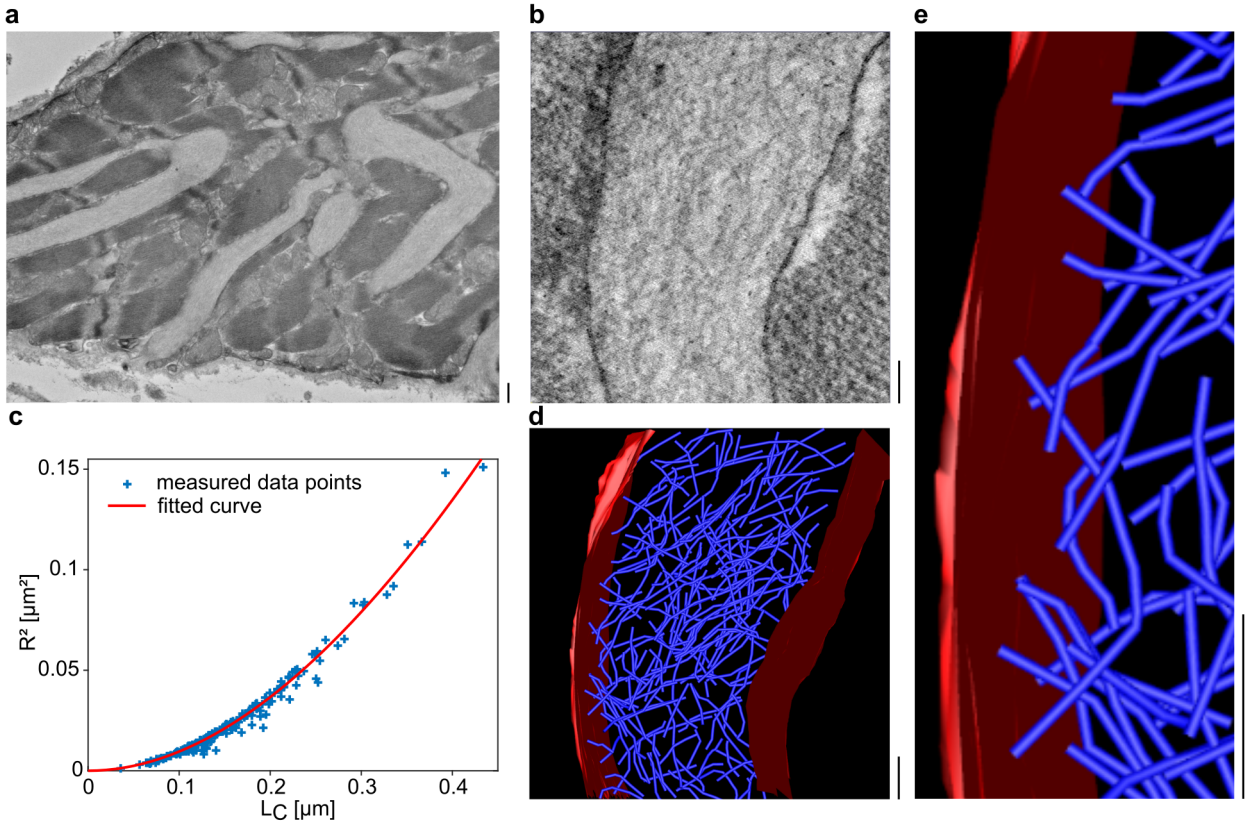

Figure 1

Tissue deposits of FOR001 amyloid fibrils.

(a) SEM overview of FOR001 heart tissue. The fibril deposits between cardiomyocytes are marked with blue asterisks. Scale bar: 1 µm. (b) STEM tomogram. Top: virtual section. The fibril deposit is marked with an asterisk. Bottom: rendered tomogram of the fibril deposit. Blue: amyloid fibrils. Red: membranes. Scale bar: 100 nm. (c) Analysis of the persistence length based on a fit of the plot showing the squared end-to-end distance versus the contour length using the equation (1). The blue symbols show the measured data points (n = 195) and the red line the fit. (d) Region of the tomogram, showing the interactions of the fibrils (blue) with the cardiomyocyte membrane (red). Scale bar 100 nm.

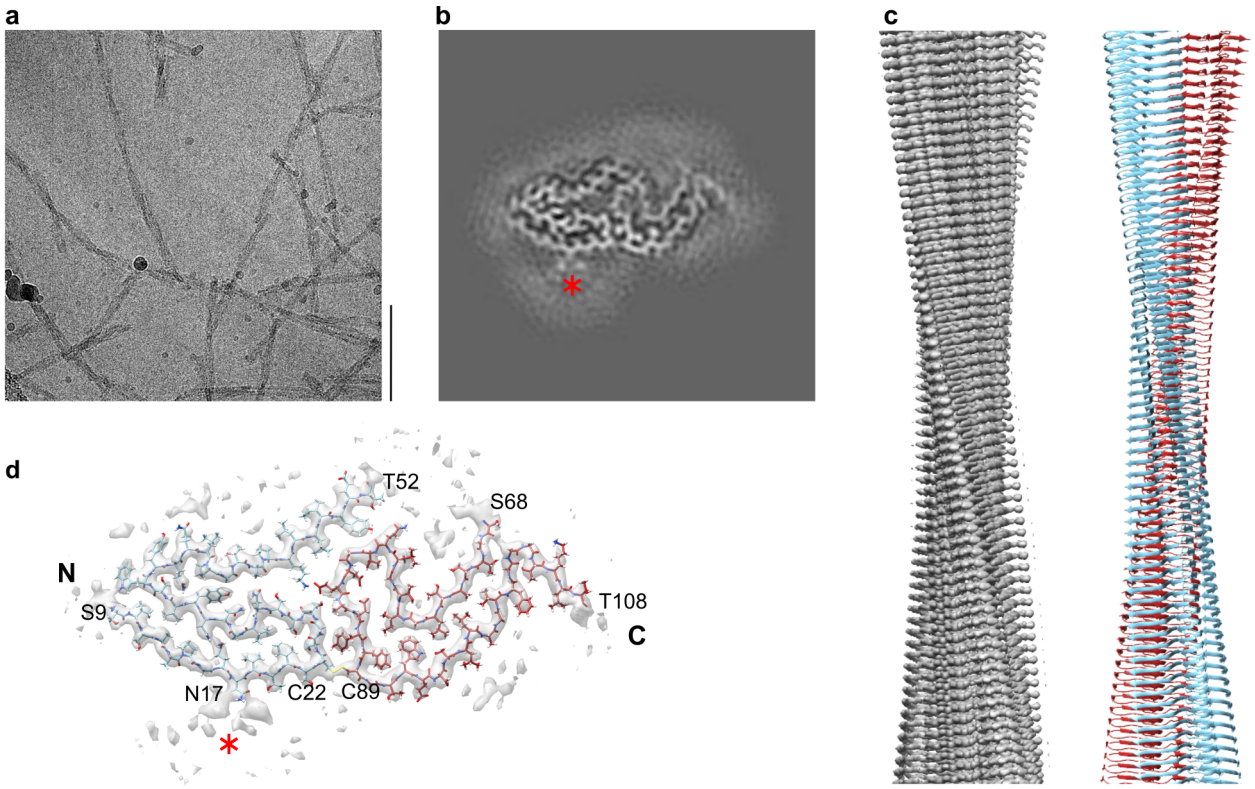

Figure 2

Cryo-EM structure of the FOR001 AL amyloid fibril.

(a) Cryo-EM image of FOR001 amyloid fibrils. Scale bar is 100 nm. The dataset consists of 3,033 micrographs. (b) Cross-section of the map obtained by summing five central slices. (c) Side-view of the map (left) and molecular model (right), showing the left-hand fibril twist. (d) Cross-section of the map with the molecular model overlaid. The color coding of the model is the same in panels (c) and (d); that is, light blue refers to the N-terminal segment of the ordered fibril protein (residues Ser9-Thr52), while the deep red segment refers to the C-terminal segment (residues Ser68-Thr108). The two segments are cross-linked through a disulfide between Cys22 and Cys89. The red star in (b) and (d) indicates the glycosylation site at Asn17.

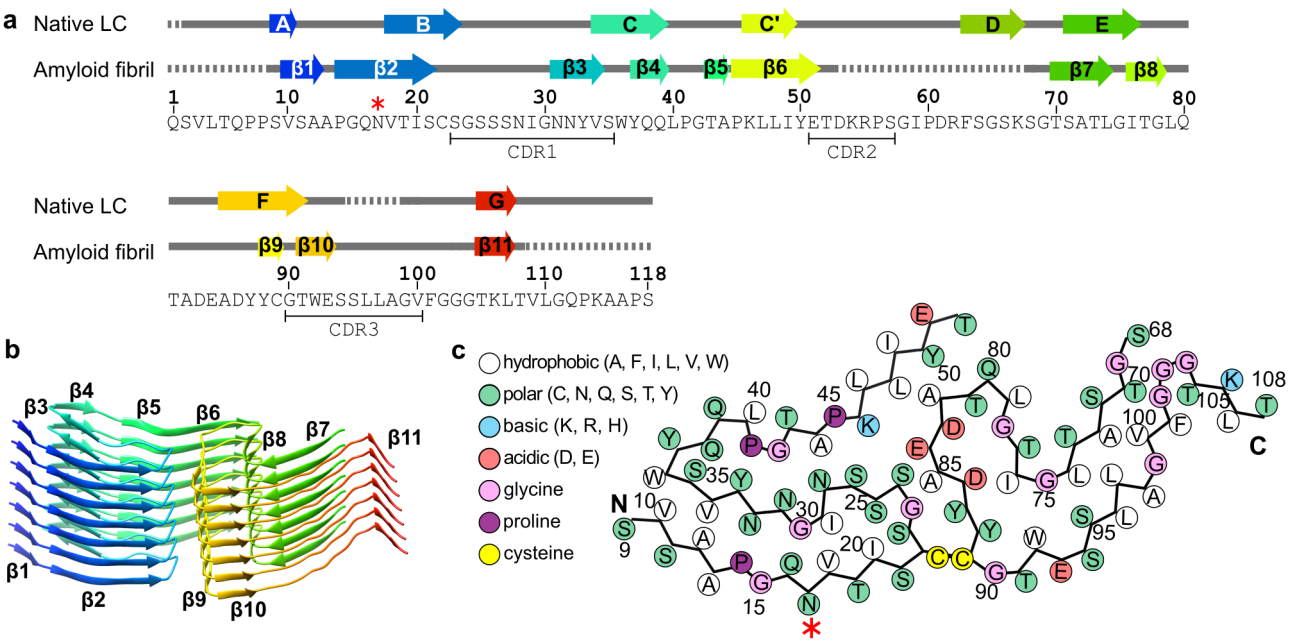

Figure 3

Location of the secondary structural elements and mutational sites in the fibril structure.

(a) Amino acid sequence of the FOR001 fibril protein and secondary structural elements of the FOR001 fibril protein (PDB 7NSL) and of a crystal structure of a natively folded LC (PDB 4ODH 10.2210/pdb4ODH/pdb) containing an *IGLV1-51*02* segment. Arrows indicate β-strands in the structure, rainbow colored from N (blue) to C-terminus (red). Dotted lines represent disordered segments. Red star: location of the glycosylation. (b) Stack of seven protein layers of the fibril, showing the β-strands β1-β11 with the same coloring as in (a). (c) Schematic representation of the fibril protein fold. Red star: location of the glycosylation.

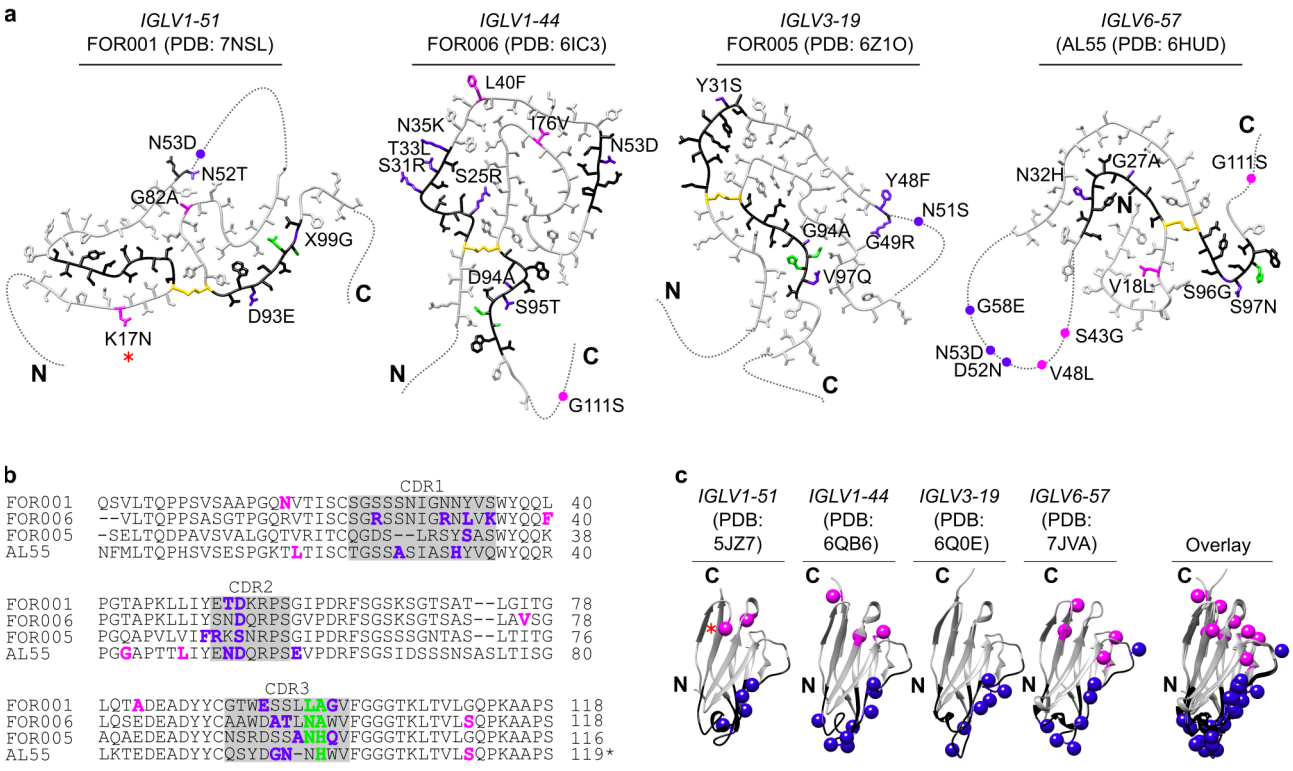

Figure 4

Location of the mutations in known AL amyloid fibrils and natively folded V_L domains.

(a) Location of the mutations in known AL amyloid fibril structures. The fibrils are derived from the GL segments *IGLV1-51*02* λ1 (FOR001, this study, PDB 7NSL) *IGLV1-44*01* λ1 (FOR006, PDB 6IC3 10.2210/pdb6IC3/pdb)[21] *IGLV3-19*01* λ3 (FOR005, PDB 6Z1O 10.2210/pdb6Z1O/pdb)[23] and *IGLV6-57*02* λ6 (AL55, PDB 6HUD 10.2210/pdb6HUD/pdb)[22]. Disordered parts of the fibril proteins are indicated by dotted lines. Black: CDRs; yellow: Cys. Indigo: mutations in the CDRs and one residue before or after a CDR; magenta: mutations in framework regions; green: residues in the junctional region at the V/J interface. Red star: location of the glycosylation. (b) Sequence alignment of the four fibril proteins. CDRs are marked with gray boxes. Color coding as in (a). (c) Location of mutations in corresponding, natively folded LC V_L domains that are based on the GL segments *IGLV1-51*01* (PDB 5JZ7 10.2210/pdb5JZ7/pdb), *IGLV1-44*01* (PDB 6QB6 10.2210/pdb6QB6/pdb) *IGLV3-19*01* (PDB 6Q0E 10.2210/pdb6Q0E/pdb) and *IGLV6-57*02* (PDB 7JVA 10.2210/pdb7JVA/pdb) CDRs are marked in black. Color coding as in (a).

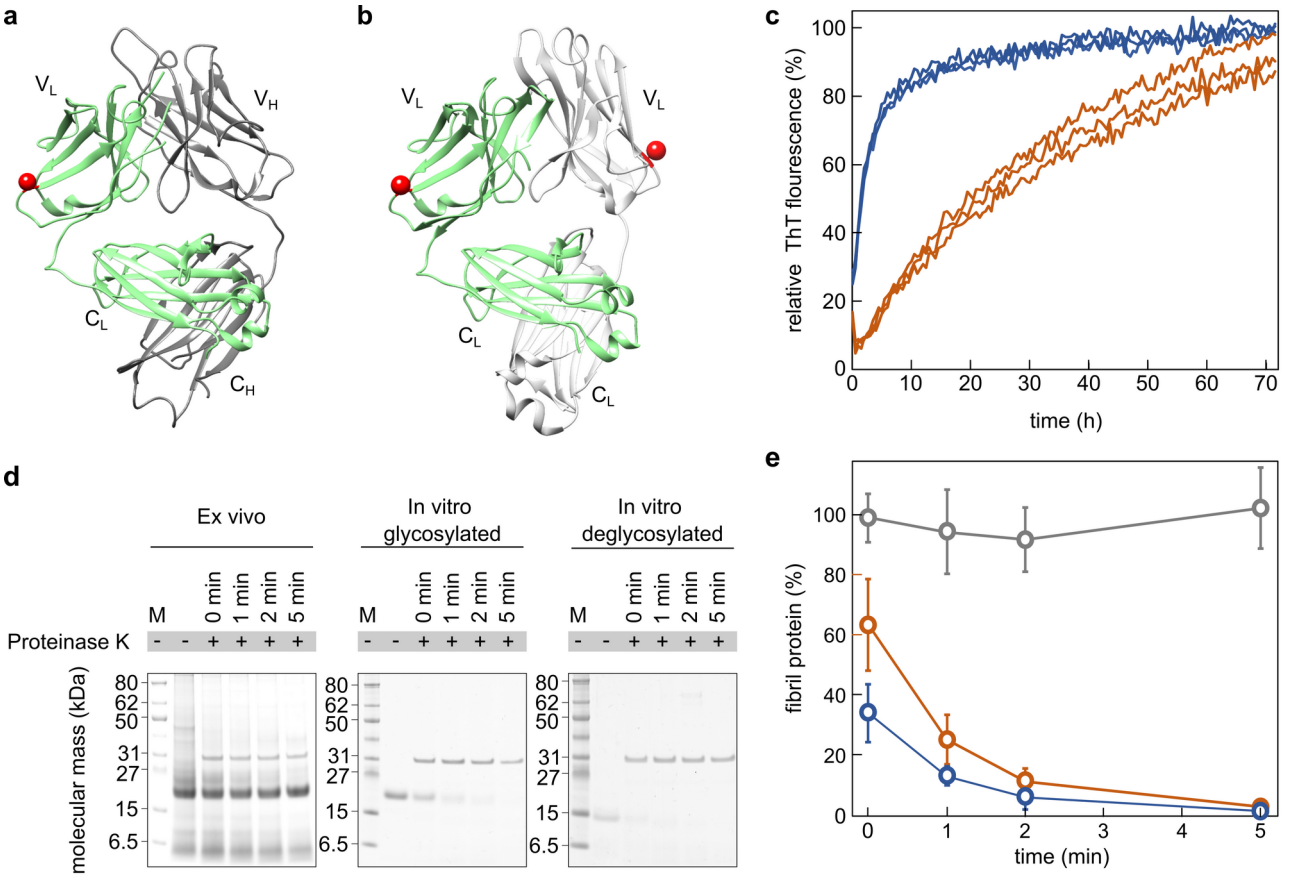

Figure 5

Effect of glycosylation on the formation of fibrils from FOR001 fibril protein.

(a) Ribbon representations of a fragment antigen binding that contains an LC with an *IGLV1-51*02* GL segment (PDB 4ODH 10.2210/pdb4ODH/pdb). The V_L and the C_L domain, as well as the variable heavy (V_H) and constant heavy (C_H) domains are labeled. The LC is marked green, the heavy chain is displayed in gray. Red sphere: residue homologous to the FOR001 glycosylation site (b) Crystal structure of an LC dimer encompassing an *IGLV1-51*02* GL segment (PDB 5MUD 10.2210/pdb5MUD/pdb). One LC in the dimer is marked green, the other in gray. Red sphere: as in (a). (c) Fibril formation kinetics of refolded FOR001 fibril protein as obtained from real-time measurements of the ThT fluorescence intensity. Blue: deglycosylated; red: glycosylated protein. (d) Coomassie-stained denaturing protein electrophoresis gels of samples to estimate the proteolytic

stability of ex vivo FOR001 fibrils and fibrils formed in vitro from deglycosylated and glycosylated FOR001 protein. Each gel was replicated three times. M: marker. (e) Densitometric quantification of the fibril protein band (n = 3) of ex vivo fibrils (gray) and in vitro fibrils from deglycosylated (blue) and glycosylated FOR001 protein (red) after digestion with proteinase K for different periods of time. The band intensity of the sample before proteinase K addition was set to 100 %. Based on a one-tailed Welch t-test, the amounts of glycosylated and deglycoslated fibril proteins differ from one another with a p-value of 0.032 and 0.049 at time points 0 min and 1 min, respectively. Error bars represent the standard deviation.

Supplementary Figures

Supplementary Figure 1

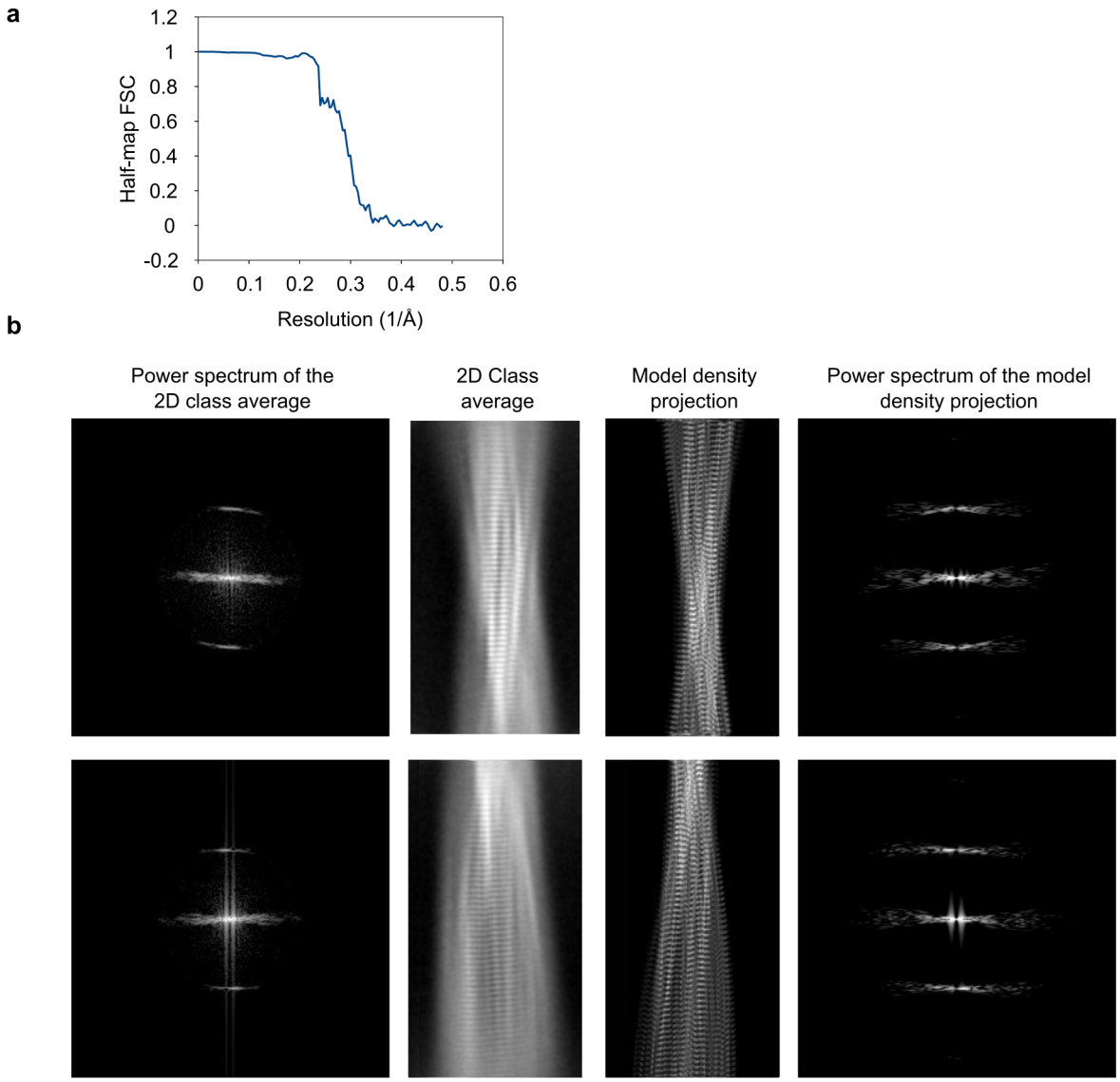

Supplementary Figure 1

FSC and comparison of the molecular model with the 2D class averages.

(a) Half-map FSC. (b) 2D classes (center left) compared with corresponding model projections (center right). The images at the far left and far right column show the power spectra of the 2D class

averages and model density projection as indicated. The top and the bottom rows refer to different z-axial positions in the fibril helix.

Supplementary Figure 2

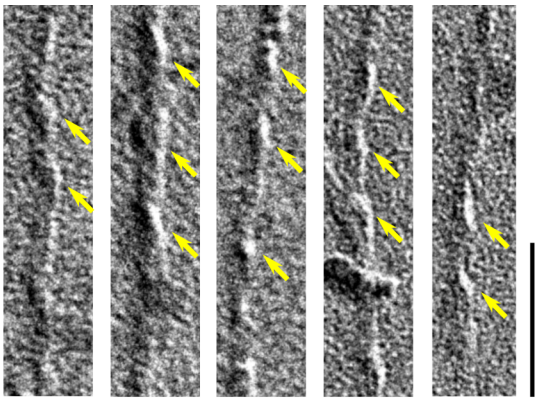

Supplementary Figure 2

Handedness of the FOR001 amyloid fibrils.

TEM images of a platinum side shadowed grid of FOR001 fibrils show a left-hand twist. To guide the eye, yellow arrows indicate the fibril crossovers. Scale bar is 100 nm.

Supplementary Figure 3

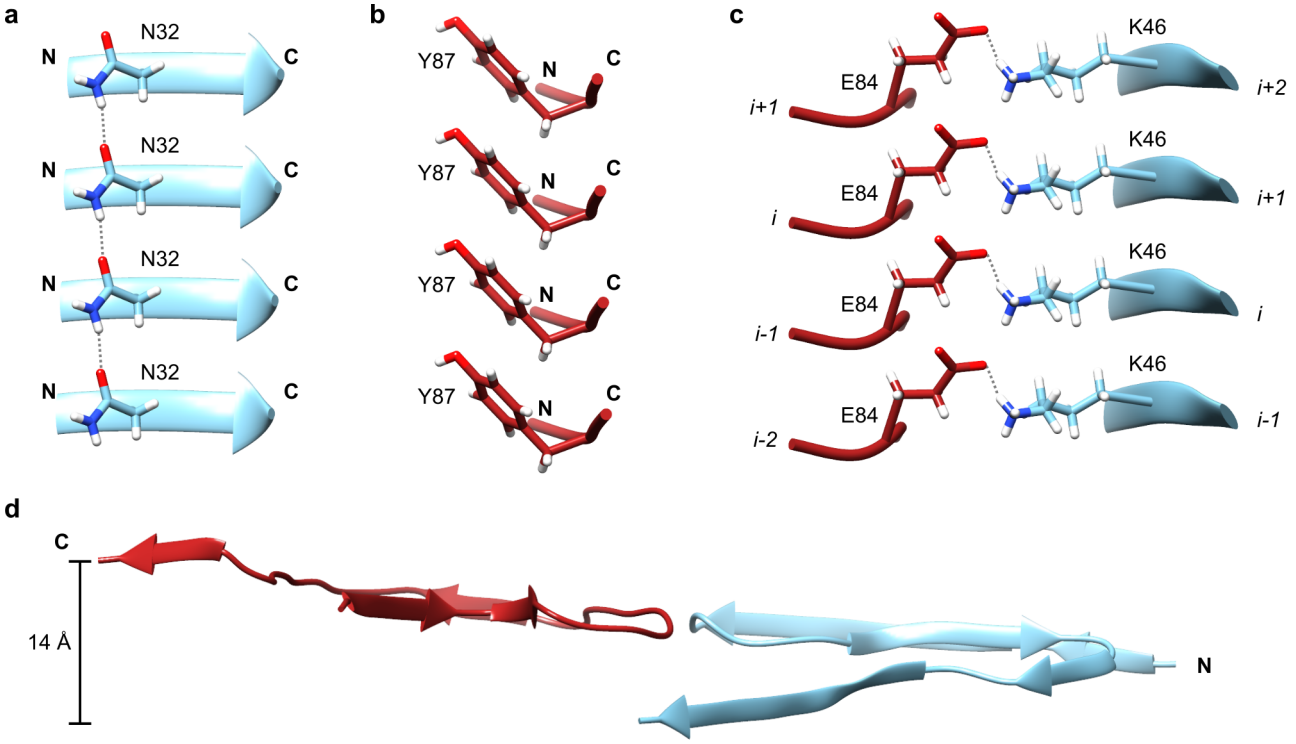

Supplementary Figure 3

Detailed views of the fibril structural model.

(a) Polar ladder formed by Asn32 residues. Dotted lines represent hydrogen bonds. (b) Aromatic stacking of Tyr87 residues. (c) Electrostatic interactions between Glu84 of layer *i* and Lys46 of layer *i+1*. Dotted lines represent salt bridges. (d) Side view of a single protein layer showing the height change of the protein backbone. The color code of the fibril protein in this figure corresponds to Fig. 1; that is, light blue refers to the N-terminal segment of the ordered fibril protein (residues Ser9-Thr52), while the deep red segment refers to the C-terminal segment (residues Ser68-Thr108).

Supplementary Figure 4

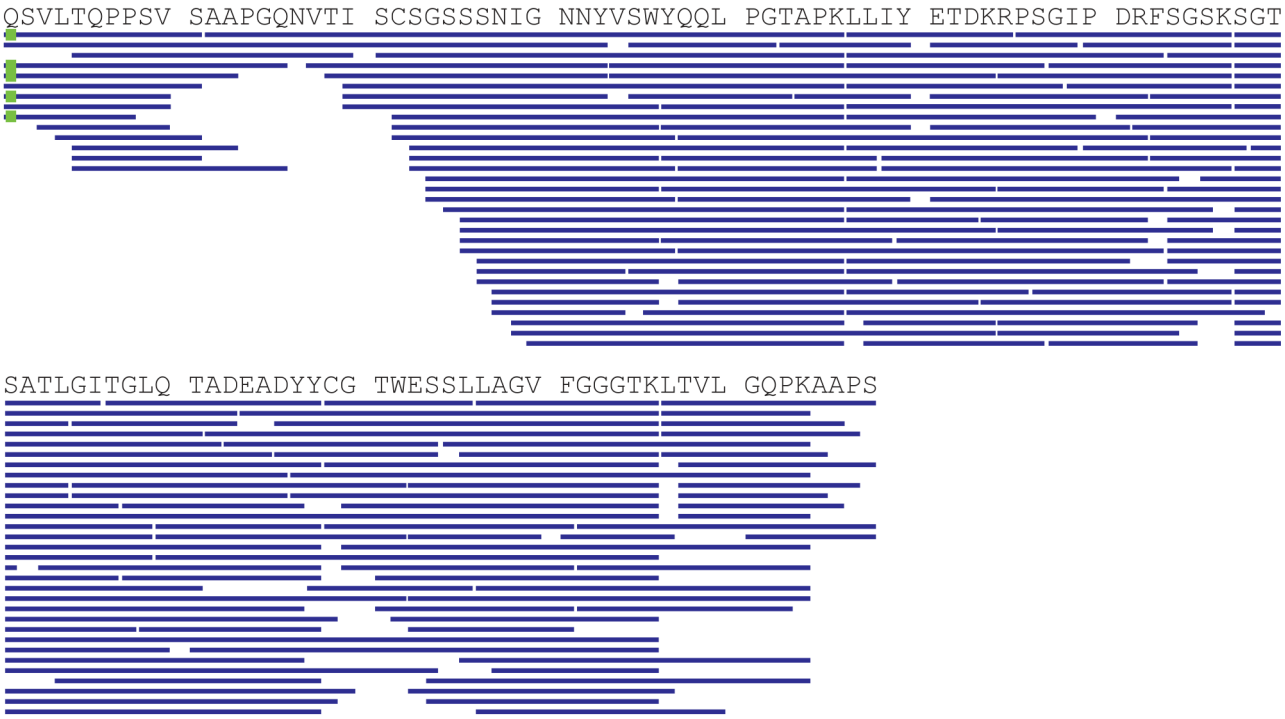

Supplementary Figure 4

Protein sequence of the FOR001 fibril protein.

Blue bars: peptide fragments identified by electrospray ionization MS and Peaks X software of glycosylated FOR001 fibril protein that was alkylated and treated with different proteases (see Methods for details). Green square: Pyro-Glu. Only a fraction of the identified peptides is displayed in the figure. Cys residues were uniformly found to be alkyated.

Supplementary Figure 5

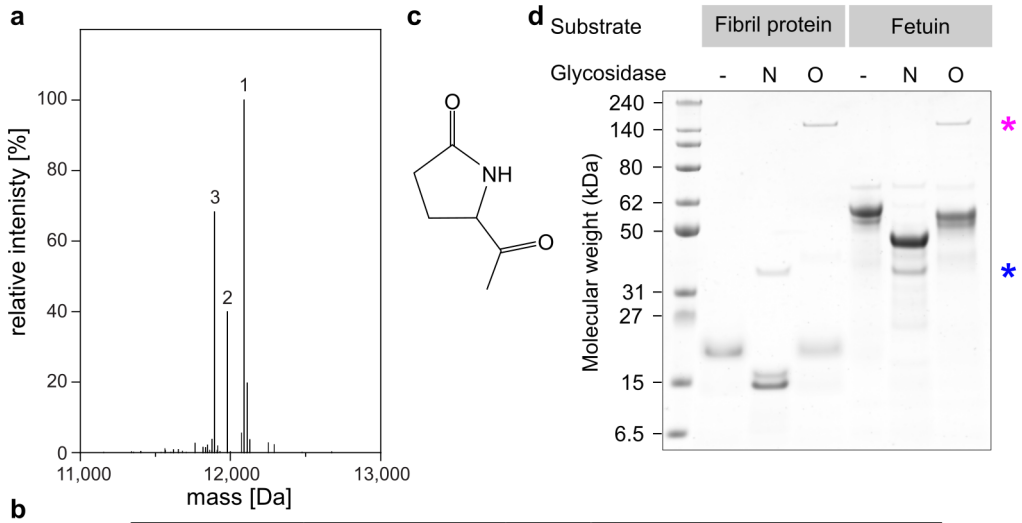

b

peak	experimental mass	theoretical mass	start	end	posttranslational modifications
1	12,089.9 Da	12,089.9 Da	**Q1**	**S118**	1x disulfide bond 1x pyroglutamylation
2	11,978.9 Da	11,978.9 Da	**S2**	**S118**	1x disulfide bond
3	11,891.9 Da	11,891.9 Da	S2 **V3** L4 Q6	P117 **S118** V119 L121	1x disulfide bond " " "

Supplementary Figure 5

Mass of the deglycosylated FOR001 fibril protein.

(a) Deconvoluted mass spectrum of the deglycosylated FOR001 fibril protein. (b) Assignment of peaks 1-3 of the deconvoluted mass spectrum shown in (a). The removal of the glycosylation at position 17 converted Asn into Asp. Blue: assignment of fibril protein fragment. For peak 3, alternative assignments are possible (black). (c) Chemical structure of Pyro-Glu. (d) Denaturing electrophoresis gel showing the deglycosylation samples of the FOR001 fibril protein or fetuin incubated with N-glycosidase or O-glycosidase. The first lane is a size marker. Blue star: position of the N-glycosidase (PNGase F); magenta star: position of the O-glycosidase. Fetuin was used as a control substrate to demonstrate the activity of both enzymes. This gel was replicated at least three times.

Supplementary Figure 6

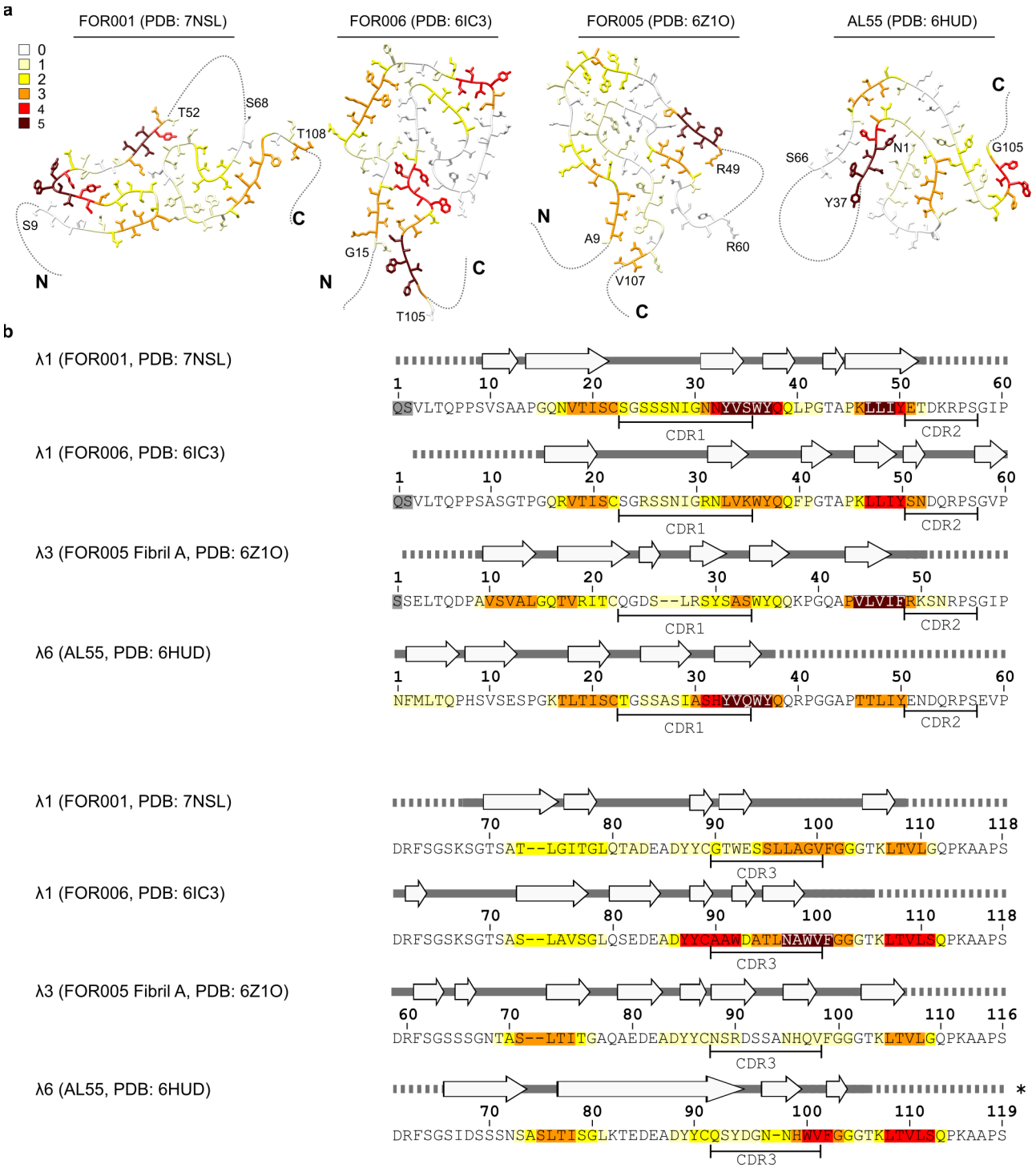

Supplementary Figure 6

Location of the aggregation prone segments in the available ex vivo fibril structures.

(a) Four published ex vivo AL amyloid fibril structures[1,2,3] colored according to aggregation score (0-5, as indicated in the figure). (b) Sequence alignment of the four fibril proteins[1,2,3]. The secondary structure of the fibril protein is displayed over the sequence. Continuous gray bar indicates the ordered segments of the fibril protein. Dotted lines indicate disordered segments that were not resolved by cryo-EM. White arrows refer to the location of the β-strands, as defined by the authors of each study. Star: no unique C-terminal end of the fibril protein reported. The sequences are color-coded according to the aggregation score as in (a). Gray boxes indicate N-terminal, cleaved residues.

Supplementary Figure 7

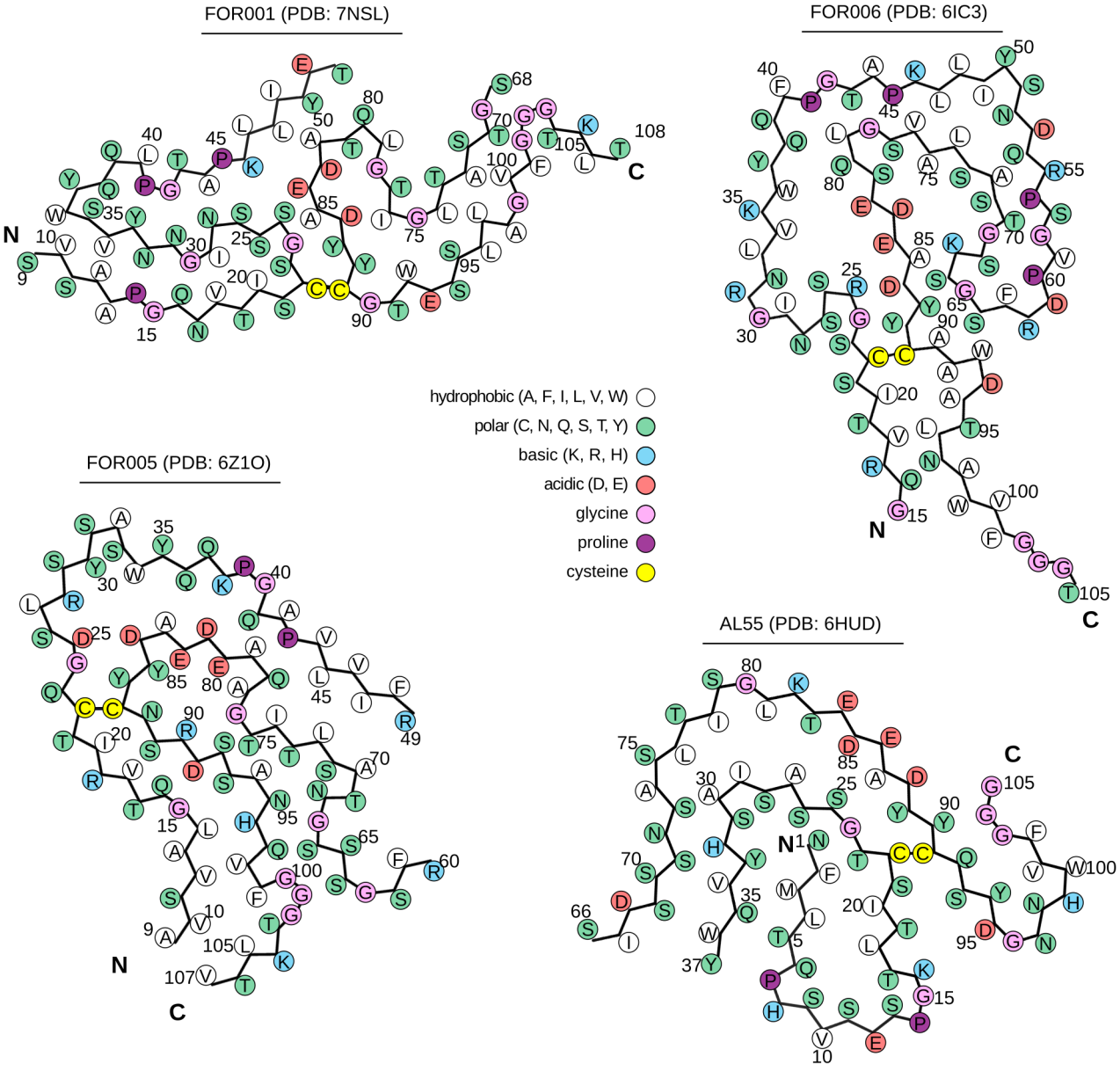

Supplementary Figure 7

Schematic comparison of four AL amyloid fibril folds.

Schematic representation of the FOR001 (PDB: 7NSL) fibril as compared to the previously reconstructed fibrils from patients FOR006 (PDB: 6IC3 [1]) and FOR005 (PDB: 6Z1O [2]) as well as of the AL55 fibril (PDB: 6HUD [3]).

Supplementary Tables

Supplementary Table 1

	(EMD-12570) (PDB 7NSL)
Data collection and processing	
Magnification	130,000
Voltage (kV)	300
Electron exposure (e– $Å^{-2}$) per frame	1
Defocus range (μm)	0.41 – 8.6
Pixel size (Å)	1.04
Symmetry imposed	C1
Initial particle images (no.)	43,308
Final particle images (no.)	43,308
Map resolution (Å) FSC threshold (0.143)	3.1
Rise (Å)	4.76
Twist (°)	-1.46
Pitch (nm)	117
Refinement	
Initial model used (PDB code)	De novo
Model resolution (Å) FSC threshold 0.143 FSC threshold 0.5	 3.0 3.2
Map CC (mask)	0.77
EMRinger ZScore	6.79
EMRinger Score	3.83
Model composition Non-hydrogen atoms Protein residues Ligands	 4263 595 0
B factors ($Å^2$) Protein Ligand	 53.74 -
R.m.s. deviations Bond lengths (Å) Bond angles (°)	 0.009 1.516
Validation MolProbity score Clashscore Poor rotamers (%)	 1.13 1.44 0
Ramachandran plot Favored (%) Allowed (%) Disallowed (%)	 96.30 3.70 0
B-factor after autosharpening ($Å^2$)	40.8

Contour level	12

Supplementary Table 1.

Reconstruction and modeling statistics.

Supplementary Table 2

	FOR001 (this study)	**FOR006 [1]**	**FOR005 [2]**	**AL55 [3]**
V segment	*IGLV1-51*02*	*IGLV1-44*01*	*IGLV3-19*01*	*IGLV6-57*02*
J segment	*IGLJ2 /IGLJ3*	*IGLJ3*	*IGLJ2*	*IGLJ3*
Number of residues in the V_L domain	110	110	108	111
Residues in fibril core	85	91	A: 89 B: 81	77
Residues in disordered V_L domain segments	25	19	A: 19 B: 27	34
Percentage of residues in ordered segments	77 %	83 %	A: 82 %, B: 75 %	69 %
Number of mutations in the V and J segments	6	9	A: 6 B: 6	10
Number of mutations in ordered segments	5	9	A: 5 B: 5	5
Percentage of mutations in ordered segments	83 %	100 %	A: 83 % B: 83 %	50 %

Supplementary Table 2

Comparison of the distribution of mutations and disordered residues in known fibril proteins.

All analyses refer to residues within the V_L domain and hence to all residues of the full-length LC except from the signal sequence and C segment. Letters A and B in the FOR005 fibril refer to fibril conformations A and B [2]. The mean value and standard deviation of the percentage of disordered residues are 22 ± 6.2 % for the four fibrils. The mean value and standard deviation of the percentage of mutations in disordered segments are 21 ± 21 % for the four fibrils. The mean values are based on FOR005 structure A [2].

Supplementary References

[1] Radamaker, L., *et al.* Cryo-EM structure of a light chain-derived amyloid fibril from a patient with systemic AL amyloidosis. *Nat Commun* **10,** 1103 (2019)

[2] Radamaker, L., *et al.* Cryo-EM reveals structural breaks in a patient-derived amyloid fibril from systemic AL amyloidosis. *Nat Commun* **12,** 875 (2021)

[3] Swuec, P., *et al.* Cryo-EM structure of cardiac amyloid fibrils from an immunoglobulin light chain AL amyloidosis patient. *Nat Commun* **10,** 1269 (2019)

Acknowledgements have been removed for data privacy reasons

Curriculum Vitae has been removed for data privacy reasons